UCSF
UC San Francisco Electronic Theses and Dissertations

Title
Improving Cancer Biomarkers through Magnetic Resonance Technology

Permalink
https://escholarship.org/uc/item/7mw8b9jd

Author
Zierhut, Matthew Luke

Publication Date
2008

Peer reviewed|Thesis/dissertation

eScholarship.org Powered by the California Digital Library
University of California

Improving Cancer Biomarkers through Magnetic Resonance Technology

by

Matthew Luke Zierhut

DISSERTATION

Submitted in partial satisfaction of the requirements for the degree of

DOCTOR OF PHILOSOPHY

in

Bioengineering

in the

GRADUATE DIVISION

of the

UNIVERSITY OF CALIFORNIA, SAN FRANCISCO

AND

UNIVERSITY OF CALIFORNIA, BERKELEY

Copyright 2008

by

Matthew Luke Zierhut

Dedicated to

Lawrence and Maxine Zierhut

and

Norman and Viola Rooney

Acknowledgements

To Sarah Nelson, for helping focus my wandering thoughts, for being a great mentor and treating me as a peer, for pushing me when I needed to be pushed, and for helping to guide me through my four years of school,

to all my colleagues in the brain lab, present: Jason Crane, Kate Hammond, Inas Khayal, Yan Li, Janine Lupo, Joe Osorio, Esin Ozturk Isik, Il Woo Park, and Radhika Srinivasan; and past: Forest Crawford, Paul DiCamillo, Michael Lee, Colleen McGue, and Pieter Pels, for their help in research projects, and for making the 3rd floor an enjoyable experience,

to my colleagues downstairs: Albert Chen, Meredith Metcalf, Cornelius von Morze, Duan Xu, Simon Hu, and Sri Veeraraghavan, for their collaboration and mini basketball hoop,

to Sharmila Majumdar, for chairing my qualifying exam committee and being the first to teach me about MRI (back in undergrad),

to Roland Henry, for helping with my qualifying exam as a member and as a teacher,

to Dan Vigneron, John Kurhanewicz, and Mark Swanson, for their expert opinions, their ability to answer difficult questions, and for the great conversations over drinks,

to Bob Brasch, for his help on this dissertation and on my qualifying exam, for showing me the ropes my first year at UCSF, and for showing me how great Thai food is,

to Steve Conolly, for his enthusiasm and support in both research and teaching, and for his help on both my qualifying exam and dissertation committees,

to Soonmee Cha and Susan Chang, for their clinical expertise and direct involvement in my research,

to Mark Albers, Bob Bok, Ralph Hurd, Kayvan Keshari, Peder Larson, Sabrina Ronen, Jim Tropp, Yi-Fen Yen, and Vickie Zhang, for their many contributions to the multiple carbon 13 research projects and for their great ideas and intellectual discussions,

to Niles Bruce and Bert Jimenez, for teaching me how to scan and making the patient scans possible,

to Greg Stolowitz, John Knueppel, Dustin Harper, Brian Hitt, Jeff King, and Joey Zwillinger, for roommate support and for trying to understand what I have been doing for the past four years,

to my parents, Randy and Gayle, for their support and encouragement in my 22 years of school,

to my big brothers and sisters, Shelley, Mike, Craig, and Becka, for being great examples and encouraging this pursuit,

to Mackenzie, Mason, Buckley, and Quinn, for the endless smiles they bring,

to Kirby, for being a great dog for 16 years and for being so excited to see me every time I got home from work,

and, finally, to my wife, Ayesha, for her love and support, for putting up with me when I'm no fun to be around, for her amazing back-tickles, and for always being there for me,

THANK YOU!

Grant funding for this thesis project was provided by UC Discovery grants, UC Dean's Health Science grants, LSIT01-10107, and ITL-BIO04-10148, in conjunction with GE Healthcare and NIH grant R01CA059880.

Abstract

Improving Cancer Biomarkers through Magnetic Resonance Technology

by

Matthew Luke Zierhut

Cancer is a complex disease that is not easily characterized, especially in its early stages. However, cancer does demonstrate numerous abnormal traits compared to healthy tissue of similar origin. These traits are most commonly observed in a tissue sample obtained through a surgical biopsy. Biopsies are not available for all tumors, and when performed, they can be highly invasive procedures.

Nuclear magnetic resonance (NMR) allows for techniques that can non-invasively investigate several abnormal characteristics common to cancer. MR imaging (MRI) can be used to see contrast in cancerous tissue with different MR properties and to monitor kinetic changes associated with cancer progression from an exogenously injected compound. MR spectroscopic imaging (MRSI) can also be used to assess the amount of certain endogenous substances, some of which are noticeably altered in the presence of cancer. Furthermore, dynamic NMR spectroscopy and MRSI can enable metabolically active exogenously injected compounds to be monitored, along with their metabolic products; thus, both kinetic and metabolic properties of cancer can simultaneous be ascertained.

In this thesis project, three techniques based on NMR technology were investigated to determine their value in assessing cancer characteristics. Kinetic modeling of T_1 weighted and T_2^* weighted dynamic contrast enhanced ^{1}H MRI (DCE-MRI) were

compared to evaluate which technique was more clinically valuable. Various techniques for reducing acquisition time for three-dimensional ^{1}H MRSI were also compared to determine which technique produced clinically relevant data with the fewest artifacts in the human brain. Finally, kinetic modeling was applied to dynamic ^{13}C spectroscopy data in rats, mice, and dogs to evaluate its promise as a future clinical technique.

The results from this research project show that kinetic modeling of T_1 weighted DCE-MRI data and ^{1}H 3D echo-planar spectroscopic imaging (EPSI) techniques are particularly valuable for cancer research, especially when compared to methods aiming for similar results. Additionally, by applying kinetic modeling and EPSI techniques to hyperpolarized ^{13}C data, it is possible to non-invasively monitor cancer metabolism in vivo. Therefore, implementing hyperpolarized $^{13}C_1$-pyruvate techniques in humans may drastically improve cancer prognoses in the near future.

Approved by Sarah J. Nelson, Dr. rer Nat

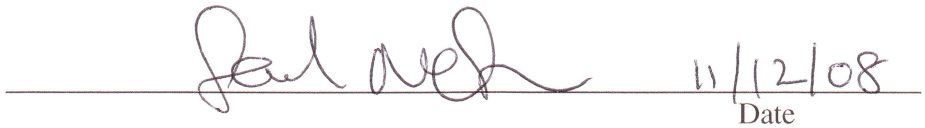

11/12/08
Date

Table of Contents

Chapter 1: Introduction 1

Chapter 2: Cancer and Nuclear Magnetic Resonance 4

2.1 Cancer 4
2.2 Nuclear Magnetic Resonance 6
2.3 NMR Spectroscopy 9
2.4 Magnetic Resonance Imaging (MRI) 14
2.5 Magnetic Resonance Spectroscopic Imaging (MRSI) 20
2.6 Summary 21
2.7 References 22

Chapter 3: Kinetic Modeling and Metabolism in MR 24

3.1 Basics of MR Contrast in Cancer 24
3.2 Kinetic Modeling 25
3.3 Cancer Metabolism 28
3.4 Improving ^{1}H 3D-MRSI Acquisitions 29
3.5 Hyperpolarized ^{13}C Spectroscopy 30
3.6 References 31

Chapter 4: Comparison of T_1 Weighted and T_2^* Weighted DCE-MRI Modeling Techniques in Human Brain Tumor Patients 34

4.1 Abstract 34
4.2 Introduction 35
4.3 Methods 38
4.3.1 Patients and Data Acquisition 38
4.3.2 Modeling 40
4.3.3 Comparative Analysis 43
4.4 Results 43
4.5 Discussion 49

4.6 Conclusion 52
4.7 References 52

Chapter 5: ^{1}H Spectroscopic Imaging of Human Brain at 3T: Comparison of Fast 3D-MRSI Techniques 54

5.1 Abstract 54
5.2 Introduction 55
5.3 Materials and Methods 56
5.3.1 MR Data Acquisition Protocol 57
5.3.2 Data Reconstruction 58
5.3.3 Data Analysis 60
5.4 Results 62
5.5 Discussion 69
5.6 Conclusions 73
5.7 Appendix: Gaussian-Weighted Average Regridding Algorithm 73
5.8 References 74

Chapter 6: Kinetic Modeling of Hyperpolarized $^{13}C_1$-Pyruvate Metabolism in Normal Rat Kidneys and TRAMP Mice 77

6.1 Abstract 77
6.2 Introduction 78
6.3 Methods 80
6.3.1 Animal and Sample Handling 80
6.3.2 Data Acquisition 81
6.3.3 Data Analysis 82
6.4 Results 85
6.5 Discussion 93
6.6 Conclusion 96
6.7 References 97

Chapter 7: How Does Dose of Hyperpolarized $^{13}C_1$-Pyruvate Affect Metabolic Results in Canine Prostate?.....99

7.1 Abstract.....99

7.2 Introduction.....100

7.3 Methods.....102

7.3.1 Animal Handling.....102

7.3.2 Sample Preparation.....102

7.3.3 Dynamic ^{13}C Spectroscopy.....103

7.3.4 Spectroscopic Imaging.....105

7.4 Results.....107

7.5 Discussion.....110

7.6 Conclusion.....111

7.7 References.....112

Chapter 8: Summary.....114

List of Tables

Table 2.1. The gyromagnetic ratios of various NMR active nuclei. 10

Table 2.2. Some published values of estimated T_1 and T_2 values in various tissues at 1.5T and 3.0T 17

Table 4.1. Median DCE-MRI parameter values for each glioma patient in the CEL 46

Table 4.2. Median blood volume parameters for each patient as estimated from T_1 weighted DCE-MRI and T_2^* weighted DCE-MRI in NAGM and NAWM 47

Table 5.1. List of all spectroscopic imaging techniques and their specifications 58

Table 5.2. Median raw SNR and normalized SNR values for all spectroscopic imaging techniques for NAA and Lac in a phantom 63

Table 5.3. Median raw SNR and normalized SNR values for all spectroscopic imaging techniques for NAA in 5 volunteers 64

Table 5.4. NAA linewidths for all techniques in phantom and volunteers 65

Table 6.1. Reproducibility of metabolic conversion parameters for a 15mm slice containing healthy rat kidney. 85

Table 7.1. Mean values of metabolite SNR and metabolic rate constants grouped by dose levels 108

Table 7.2. Median estimated values of metabolite T_1 constants and arrival time for all dogs 108

Table 7.3. Estimated Michaelis-Menten parameters from fitted metabolic rate constants 108

Table 7.4. Pyruvate and lactate maximum SNR values in prostate tissue for 14 spectroscopic image acquisitions 109

List of Figures

Figure 2.1. Chart showing typical ranges of ^{1}H chemical shifts for certain functional groups. 11

Figure 2.2. Proton spectrum acquired from a normal human brain 13

Figure 2.3. Three types of MRI contrast in a healthy human brain 16

Figure 2.4. Pulse sequence diagram of a general 3D MRI acquisition with an inversion recovery and a spin echo pulse 19

Figure 2.5. One slice of a three-dimensional magnetic resonance spectroscopic image of a healthy human brain is shown....21

Figure 4.1. Before and after Gd injection 36

Figure 4.2. Representative ROI image....39

Figure 4.3. Images from three glioma patients representing grade 2, 3, and 4 gliomas....44

Figure 4.4. Boxplots of parameter values vs grade....47

Figure 4.5. Comparison plots of blood volume parameters and endothelial leak parameters. 49

Figure 5.1. Gradient waveforms used for two different echo-planar spectroscopic imaging encoding techniques. 59

Figure 5.2. Median percentages of detectable voxels in each metabolite peak region are shown in the bar graph for each spectroscopic imaging technique 66

Figure 5.3. Representative datasets of two volunteers' spectra 67

Figure 5.4. Qualitative examples of the partial volume effect in each spectroscopic imaging technique 68

Figure 5.5. Typical data acquired on a glioma patient using a flyback EPSI sequence. 69

Figure 6.1. Simplified diagram of the biochemical pathways taken by $^{13}C_1$-pyruvate....79

Figure 6.2. Examples of dynamic curves of metabolite levels in a 15mm slice containing healthy rat kidney and a 10mm slice containing TRAMP tumor 86

Figure 6.3. Response of metabolic conversion parameters to varying doses of $^{13}C_1$-pyruvate.....87

Figure 6.4. Response of initial reaction rates to varying doses of $^{13}C_1$-pyruvate 88

Figure 6.5. Response of initial pyruvate-to-lactate reaction rates in four 10mm slices containing TRAMP tumor to varying doses of $^{13}C_1$-pyruvate.....89

Figure 6.6. Serial plots of estimated metabolic conversion parameters over time for three mice with a transgenic prostate tumor.....90

Figure 6.7. One dimensional flyback echo planar spectroscopic imaging data from a wild type mouse and a TRAMP mouse.....92

Figure 7.1. Representative dynamic curves of metabolite SNR for 3 different $^{13}C_1$-pyruvate doses in different dogs 108

Figure 7.2. Representative pyruvate and lactate peak height images from an MS-FSEPSI data set in a dog.....109

Chapter 1: Introduction

Cancer is the 2nd leading cause of death in the US, killing nearly 600,000 people every year (23% of all deaths)[§]. However, with early accurate characterization, cancer survival rates can be dramatically improved[‡]. Various nuclear magnetic resonance (NMR) technologies have been commonly used to aid in cancer diagnoses and early detection, including: magnetic resonance imaging (MRI), dynamic contrast enhanced MRI (DCE-MRI), and MR spectroscopic imaging (MRSI). These NMR techniques can produce biomarkers of cancer severity and many are used by clinicians to aid in their prognoses.

This thesis project aims to improve the current state of cancer diagnostics through NMR technology 1.) by comparing similar techniques to assess which produce the most valuable results, 2.) by improving techniques' clinical applicability, 3.) by implementing new techniques in human patients, and 4.) by developing new techniques for future clinical use. Specifically, this project focuses on improving cancer biomarkers through kinetic modeling and spectroscopic techniques applied to ^{1}H and ^{13}C data in brain and prostate tumors.

Chapter 2 gives a brief introduction to cancer and cancer diagnostic procedures, focusing on the brain and prostate. It introduces NMR as a useful technology to non-invasively assess characteristics of cancer, further describing technical details of numerous NMR data acquisition techniques.

[§] Cancer Statistics 2008. American Cancer Society.
<http://www.cancer.org/docroot/PRO/content/PRO_1_1_Cancer_Statistics_2008_Presentation.asp>
[‡] <http://www.cancer.net/patient/Learning+About+Cancer/Statistics/Understanding+Survival+Statistics>

Chapter 3 expounds on the techniques introduced in chapter 2 by discussing how they can be used to gain clinical information about brain and prostate cancer. It also discusses how NMR technologies can be used to probe tracer kinetics and cancer metabolism through kinetic modeling and spectroscopy of ^{1}H and ^{13}C nuclear magnetic resonances. Specifically, three techniques are introduced: 1.) kinetic modeling of an inert exogenous contrast agent using DCE-MRI; 2.) spectroscopic assessment of endogenous tissue metabolites using three-dimensional ^{1}H MRSI; and 3.) kinetic modeling of an exogenously introduced metabolite and its endogenous products using dynamic ^{13}C NMR spectroscopy.

Chapter 4 compares kinetic modeling techniques applied to T_1 weighted and T_2^* weighted DCE-MRI in human brain tumor patients. Accuracies of the estimated parameters were assessed and the parameters were compared to determine which was most valuable for helping to characterize gliomas. Encouraging results were returned from both techniques; however, modeling of the T_1 weighted data appeared to show more tumor contrast and possibly correlated more with tumor malignancy.

Chapter 5 discusses various techniques for improving ^{1}H 3D-MRSI acquisition time (t_{ACQ}) and compares data acquired from each in spectroscopic phantoms and healthy human volunteer brains. While all techniques appeared to produce reliable data in less than 11 minutes (~50% reduction in t_{ACQ}), the echo-planar spectroscopic imaging (EPSI) techniques appeared to suffer the least from artifacts such as partial voluming and lipid aliasing. Clinically relevant 3D-MRSI data were also acquired in seventeen patients with a flyback EPSI technique in less than 9.5 minutes.

Chapter 6 presents the implementation of a kinetic modeling technique applied to dynamic ^{13}C spectroscopic data from regions containing rat kidneys or a transgenic adenocarcinoma of the mouse prostate (TRAMP) after injecting hyperpolarized $^{13}C_1$-pyruvate. A one-dimensional EPSI technique was also used to acquire dynamic ^{13}C data simultaneously in multiple 10 mm axial slices of TRAMP mice. Results suggest that the modeling technique used was robust and the 1D-EPSI data were of similar quality to single slice data. Michaelis-Menten kinetics appear to successfully describe the relationship between estimated metabolic conversion parameters and amount of injected pyruvate. Furthermore, results show that pyruvate-to-lactate conversion was accelerated in TRAMP tumors and increased with tumor progression.

Chapter 7 applies the kinetic modeling introduced in chapter 6 to single slice data acquired from healthy canine prostates, a more human-like model. ^{13}C Spectroscopic imaging is also acquired in two and three dimensions, using an EPSI technique for three-dimensional data. Results show similar findings to the rat and TRAMP data in that as pyruvate dose increased, pyruvate conversion to products proportionally decreased, as suggested by Michaelis-Menten kinetics. Furthermore, low dose pyruvate data produced similar lactate SNR to higher dose data, suggesting low clinical human doses may be just as sensitive.

Chapter 8 summarizes the conclusions from the preceding chapters and discusses the contributions from this work to the clinical and scientific communities.

Chapter 2: Cancer and Nuclear Magnetic Resonance

2.1 Cancer

More than 1.4 million people in the United States will be diagnosed with some form of cancer in 2008, and nearly 570,000 people will die from it (approximately 23% of all US deaths) (1). Although primary brain and central nervous system (CNS) tumors are not the most common form of cancer (approximately 52,000 people will be diagnosed this year (2)), they are among the most lethal, as the annual number of deaths is nearly 70% of the annual incidence of malignant brain and CNS tumors (3). While prostate cancer is less lethal than brain cancer (annual deaths are about 16% of incidences), it is the most prevalent male form of cancer, making up approximately 25% of all new male cancer cases each year (>186,000) (1). In both cancers, while they may not always be lethal, they almost always have an adverse effect on the patient's quality of life, and it is therefore important to improve upon early diagnosis, treatment planning, and treatment monitoring to help improve the lives of patients with these diseases.

Not all primary brain and CNS tumors are malignant; thus the health risks of aggressive treatment are not always necessary. The most common type of primary brain tumor is a glioma, a tumor of the neuroglial support cells. Gliomas display both intertumoral and intratumoral heterogeneity. The variety of biological characteristics necessitates multiple treatment options. Glioma classification and grading are currently based on the World Health Organization (WHO) system of histological analysis of surgical biopsies, ranging from I (benign) to IV (highly malignant). These guidelines focus on four histological aspects of surgical biopsies to assess tumor grade: 1) nuclear

atypia, 2) mitotic activity, 3) endothelial proliferation, and 4) necrosis (4). The number of these criteria that are present determine the tumor grade, with more criteria signifying higher grade. Other criteria are needed to classify specific tumor type, such as tumor location, cell type, and immunohistochemical (IHC) assays, but the WHO guidelines strongly direct the prognosis, and thus the planned treatment. Tumor grading is not flawless however, as biopsies can be prone to sampling errors inherent to heterogeneous tumors, and surgical biopsy is an invasive procedure that is not always feasible due to the location of the tumor.

Prostate cancer is most commonly staged by tissue biopsy according to the Tumor/Nodes/Metastases (TNM) system. Histologic samples are put into one of four stages (I being benign, IV being malignant) according to the tumor size, lymph node involvement, and presence or boundary of metastases. Grade I and II prostate tumors are confined within the borders of the prostate, while grade III and IV tumors have spread to other tissues. TNM staging is only a portion of what doctors use to decide on prostate cancer treatment, as the Gleason score (5) and the value of a known protein marker, prostate specific antigen (PSA) (6), also contribute to a "risk group" assessment. Patients are categorized as low, intermediate, or high risk, which directly correlate with the aggressiveness of recommended treatment. Prostate cancer suffers from similar issues as brain tumors in that biopsies cannot always capture the heterogeneity of the tumors. Additionally, biopsies and aggressive treatment can be painful, and may not always be necessary – especially in cases of benign prostatic hyperplasia (BPH).

The development of reliable and robust techniques for non-invasively assessing the characteristics of gliomas and prostate cancer would be extremely valuable. Several

groups have specifically used nuclear magnetic resonance (NMR) technology this purpose (7,8,9). While the results that have been obtained are promising, there still exists a need for improving sensitivity and specificity of the techniques available.

2.2 Nuclear Magnetic Resonance

Nuclear Magnetic Resonance (NMR) is a phenomenon of atomic nuclei that allows researchers to probe multiple chemical and biological properties. An atomic nucleus may possess an intrinsic non-zero magnetic moment (μ) if it has any unpaired nucleons (protons or neutrons). This nuclear magnetic dipole moment is due to the spin nature of protons and is described for a proton (^{1}H nucleus) according to the following equation:

$$\mu = \frac{\gamma h}{4\pi}, \qquad [2.1]$$

where γ is the gyromagnetic ratio intrinsic to the nuclei involved and h is Planck's quantum constant. A single proton, has two possible nuclear spin-states in the presence of an applied static magnetic field (B_0): spin-up (aligned with the field) or spin-down (aligned against the field). Each spin-state has an associated energy state (E):

$$E = \frac{s_n \gamma h B_0}{2\pi}, \qquad [2.2]$$

where s_n is the nuclear spin (±½ for a proton). Most nuclei will align with the field (s_n is positive, spin-up), but the proportion depends on thermal energy and the energy difference (ΔE) between the two spin-states. More specifically, the ratio of aligned nuclei (n_+) to anti-aligned nuclei (n_-) is related to the Boltzmann probability distribution:

$$\frac{n_+}{n_-} = e^{\frac{\Delta E}{kT}}, \qquad [2.3]$$

where k is Boltzmann's constant and T is temperature. For protons, the proportional excess of aligned nuclei in a static magnetic field can be approximated as follows:

$$\frac{n_+ - n_-}{N} \approx \frac{h\gamma B_0}{4\pi kT}, \qquad [2.4]$$

where N is the total number of nuclei. At a magnetic field strength of 1.5 Tesla (1.5T), which is commonly used in hospitals around the world, this fraction is less than five protons per million at normal human body temperature. Yet, because there are so many protons in the human body (on the order of 10^{27} protons), the net contribution from the magnetic dipoles leads to measurable NMR effects.

In order to measure these effects, Faraday's law of induction is applied (Equation 2.7). Nuclear spin causes a precession around an applied magnetic field, similar to a spinning gyroscope, with a specific frequency (the Larmor frequency, ω_0) given by the following equation:

$$\omega_0 = \gamma B_0. \qquad [2.5]$$

The equilibrium net magnetization (M_0), resulting from the sum of the nuclei's dipoles aligning with $\mathbf{B_0}$, precesses around the applied static field at this Larmor frequency, or resonance frequency. Typical field strengths put this resonance frequency in the radio frequency (RF) range for most nuclei. The magnitude of the equilibrium magnetization, M_0, is the product of the nuclei's magnetic dipole moment (μ), the proportional excess of aligned nuclei (Equation 2.4), and the density of nuclei in the volume involved (ρ_0). For hydrogen (^{1}H),

$$M_0 = \frac{\rho_0 h^2 \gamma^2 B_0}{(4\pi)^2 kT}. \qquad [2.6]$$

By applying an additional magnetic field (B_1), oriented perpendicularly to the $\mathbf{B_0}$ field vector and oscillating at exactly the Larmor frequency, the net magnetization vector ($\mathbf{M}$) can be manipulated to rotate around the $\mathbf{B_1}$ field vector. Furthermore, the additional field can be precisely applied to direct $\mathbf{M}$ from alignment with $\mathbf{B_0}$ ($\mathbf{M}_{\parallel}$) to a plane perpendicular to $\mathbf{B_0}$ ($\mathbf{M}_{\perp}$) (or any angle). This procedure is typically called an RF excitation pulse, as the B_1 excitation frequency is in the RF range. After the $\mathbf{B_1}$ field is removed, $\mathbf{M}$ will continue to precess around $\mathbf{B_0}$ at the Larmor frequency, although it is now oriented in the perpendicular plane. According to Faraday's law of induction, the net nuclear magnetic moment, $\mathbf{M}$, will generate a voltage, V, in a specifically tuned electrically conducting coil that is equal to the rate of change of the magnetic flux from $\mathbf{M}$, $\Phi_{\mathbf{B}}$, through the coil area, $\mathbf{A}$. Specifically:

$$\Phi_{\mathbf{B}} = \int_{\mathbf{A}} \mu_0 \mathbf{M} \cdot d\mathbf{A}$$
$$V = \frac{-d\Phi_{\mathbf{B}}}{dt}, \qquad [2.7]$$

where μ_0 is the permeability of free space. Thus, if a coil is oriented perpendicular to the $\mathbf{B_0}$ vector, it can generate a voltage from the oscillating net magnetization in the transverse plane, $\mathbf{M}_{\perp}$.

Signal measured in the transverse plane from the receive coil will immediately begin to decay after the $\mathbf{B_1}$ field is removed. The two main processes involved in the decay of the $\mathbf{M}_{\perp}$ signal are T_1 effects and T_2 effects. Signal decay caused by T_1 effects is due to nuclear spin-lattice interactions that cause the net magnetization to return to equilibrium and align with $\mathbf{B_0}$, thus $\mathbf{M}_{\parallel}$ will grow and $\mathbf{M}_{\perp}$ will get smaller. T_2 signal

decay is due to nuclear spin-spin interactions, or irreversible interactions at the nuclear level that cause the net magnetization vector to spread throughout the transverse plane. T_2 is defined as the time it takes $\mathbf{M}_\perp$ to decay to $e^{-1}\mathbf{M}_\perp$ and T_1 is defined as the time it takes $\mathbf{M}_\parallel$ to recover to $e^{-1}\mathbf{M}_\parallel + (1-e^{-1})\mathbf{M}_0$. There is also $\mathbf{M}_\perp$ signal decay due to reversible interactions, or external field inhomogeneities, known as T_2' effects. Signal decay from the combination of T_2 and T_2' effects is known as T_2^* decay, or decay from magnetic susceptibility, and is described by the equation:

$$\frac{1}{T_2^*} = \frac{1}{T_2} + \frac{1}{T_2'}. \qquad [2.8]$$

A more general description of the behavior of a net magnetic dipole (**M**) in an external magnetic field (**B**) can be summarized by the Bloch equation:

$$\frac{\partial \mathbf{M}(t)}{\partial t} = \gamma \mathbf{M}(t) \times \mathbf{B}(t) + \frac{1}{T_1}\left(M_0 - \mathbf{M}_\parallel(t)\right) - \frac{1}{T_2}\mathbf{M}_\perp(t). \qquad [2.9]$$

This equation includes the influences of the longitudinal magnetization ($\mathbf{M}_\parallel$) recovery constant (T_1) and the transverse magnetization ($\mathbf{M}_\perp$) decay constant (T_2) as well as the precession described above.

2.3 NMR Spectroscopy

The gyromagnetic ratio (γ) has an intrinsic value for each nucleus. For example, for a hydrogen nucleus (^{1}H), γ_{1H} = 42.58 MHz/T, but for the nucleus of the isotope carbon-13 (^{13}C), γ_{13C} = 10.71 MHz/T. This difference causes the nuclei to precess at different frequencies in the exact same environment, and makes simultaneous measurements from multiple nuclei nearly impossible. (Table 2.1 lists gyromagnetic ratios for some spin active nuclei.) However, the same element's nuclei may precess at

slightly different frequencies as well, due to local differences in the magnetic field. These small differences can be measured more practically.

Table 2.1. The gyromagnetic ratios of various NMR active nuclei.

Nucleus	γ (MHz/T)
^{1}H	42.576
^{3}He	-32.434
^{7}Li	16.546
^{13}C	10.705
^{14}N	3.0766
^{15}N	-4.3156
^{17}O	-5.7716
^{23}Na	11.262
^{31}P	17.235
^{129}Xe	-11.777

Differences in precession frequency can be due to inhomogeneities in the static B_0 field, intentionally applied magnetic field gradients, or chemical shielding of the spin active nuclei by spinning electrons. While B_0 inhomogeneities can cause measurement artifacts, magnetic field gradients are what allow for imaging and chemical shielding is what allows for spectroscopy.

Chemical shielding is important in NMR research as it allows researchers to probe the chemical composition of substances based upon the slight differences in the local magnetic field. Equation 2.10 shows a modified Larmor equation to account for this shielding:

$$\omega_0 = \gamma B_0(1-\sigma), \qquad [2.10]$$

where σ represents the amount of chemical shielding experienced by the nucleus. A σ of 0 represents a "free" nucleus, not affected by any chemical shielding, while a σ of 1 represents a nucleus that is experiencing shielding that exactly cancels the applied magnetic field, and thus no net magnetic field. Typically, σ values are on the order of a couple parts per million (ppm). The frequency shift due to chemical shielding is known as a chemical shift. Figure 2.1 is a chart showing typical ranges of ^{1}H chemical shifts for certain functional groups.

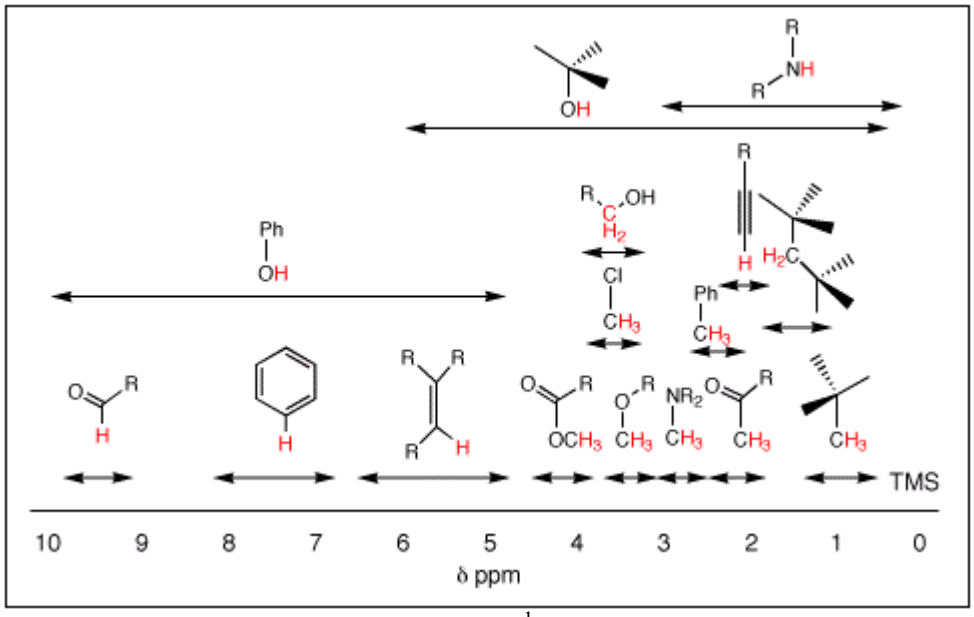

Figure 2.1. Chart showing typical ranges of ^{1}H chemical shifts for certain functional groups. (From the University of Colorado, Boulder, Chemistry and Biochemistry Department (10)). Tetramethylsilane (TMS) is located at 0 ppm as a reference peak

Using a technique as described in section 2.2 to measure the net transverse magnetization ($\mathbf{M}_\perp$), the chemical composition of a substance can be determined by determining the chemical shielding present for a specific spin active nucleus. The measured NMR signal from the transverse magnetization will consist of all the magnetic

dipoles in a sample, each precessing at a frequency determined by the applied magnetic field and the inherent chemical shielding of that nucleus. This signal can then be Fourier transformed to reveal the specific frequencies, and thus chemical shielding, present. The Fourier transform is a powerful tool for lossless conversion between two domains: in this case the time (t) and frequency (f) domains. Equation 2.11 is the general equation for a one-dimensional Fourier transform:

$$H(f) = \int_{-\infty}^{\infty} h(t) e^{-i2\pi ft} dt \,, \qquad [2.11]$$

where $H(f)$ is a function in the inverse domain of $h(t)$.

Because the NMR signal is discrete and not acquired continuously, the Discrete Fourier transform is used to transform the free induction decay (FID) measured from the transverse plane into a frequency spectrum. If the time signal measured in the transverse plane is represented by $M(t)$, the frequency spectrum, $S(f)$, can be calculated as follows:

$$S\left(\frac{k}{N\Delta t}\right) = \sum_{n=0}^{N-1} M\left(n\Delta t\right) e^{\frac{-i2\pi kn}{N}} \,. \qquad [2.12]$$

Here N discrete samples are acquired, k is the discrete sample number in frequency, n is the discrete sample number in time, and Δt is the time between samples. Thus, continuous time is discretized such that $t = n\Delta t$ and frequency is discretized such that $f = k\Delta f = \frac{k}{N\Delta t}$. Figure 2.2 shows an example of a proton NMR spectrum acquired from a normal human brain. Multiple distinct chemical shielding species are easily seen from the multiple spectral peaks. Generally, the area under each peak is proportional to the number of nuclei experiencing a particular chemical shielding. Multiple nuclei can

experience the exact same chemical shielding due to molecular symmetry and bond rotations. These are referred to as equivalent nuclei.

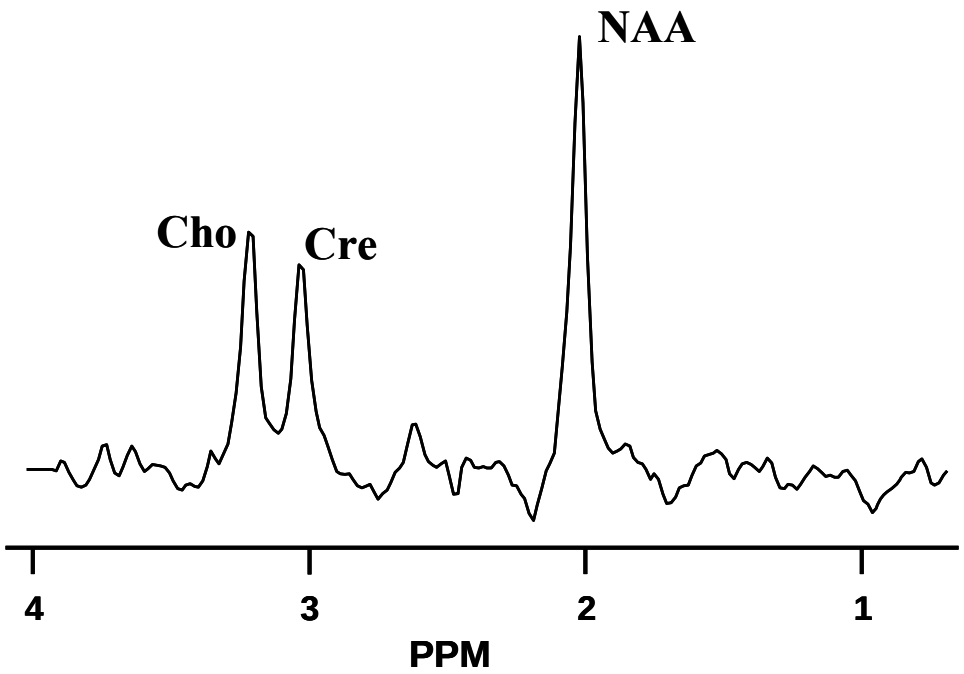

Figure 2.2. Proton spectrum acquired from a normal human brain. Multiple chemical shielding entities are observable, most notably from choline containing compounds (Cho), creatine (Cre), and N-acetyl aspartate (NAA). The largest peak in the spectrum appears near 2.0 ppm and is from the chemically shielded magnetic dipoles from the three methyl protons found in NAA. The peak seen near 3.03 ppm is shifted due to the chemical shielding of the three methyl protons in creatine. Choline has nine equivalent methyl protons that resonate near 3.2 ppm. Multiple compounds contain choline, and thus will contribute to the spectral peak at 3.2 ppm. Three known choline containing compounds that exist in the human brain are free choline, phosphorylcholine (PC), and glycerophosphorylcholine (GPC).

Spinning electrons are not the only source of local magnetic influence in a molecule. Other nuclei, located nearby via molecular bonds, have an additional influence on the local magnetic field experienced by each nucleus. As discussed earlier, each proton can exist in a spin-up ($s_n = +½$) or spin-down ($s_n = –½$) state when subjected to a B_0 field. Thus, nearby protons will add or subtract to the local magnetic field depending on their state, causing a splitting of the resonant peak. More nearby unique (non-

equivalent) protons create more peak splits. These interactions are known as spin-spin coupling, or J-coupling, and their effects can also be used to help further deduce chemical structure.

2.4 Magnetic Resonance Imaging (MRI)

Acquiring images from the magnetic dipoles of nuclei involves the same theory as in acquiring NMR spectroscopy. The major difference is that the chemical shielding that allows for probing of various chemical compositions is neglected in favor of intentional manipulation of the local magnetic fields. Moreover, ^{1}H MRI assumes that all NMR signal comes from one type of proton (a water proton), and there is no chemical shielding. By introducing magnetic field gradients that cause the applied $\mathbf{B_0}$ field to predictably vary in space, the protons throughout these spatial areas will precess at known spatially dependent frequencies. Instead of transforming time data into the frequency domain (as in NMR spectroscopy), the Fourier transform will convert the measured net transverse magnetization into the image domain. An MRI is thus an image of the magnitude of the transverse magnetization, where the signal in each voxel is the magnitude of the transverse magnetization there.

To obtain a three-dimensional (3D) image, gradients are applied in three orthogonal spatial dimensions (x, y, z) to sample the inverse image domain, known as k-space. A three-dimensional inverse Fourier transform will then convert the data into an image. There are many different strategies for acquiring k-space data, but a general representation of this relationship is shown in equation 2.13 for linear gradients, G_i, in each ith dimension, where $S(k_x, k_y, k_z)$ represents the measured signal, or the net

transverse magnetization over all space, during the sample at each (k_x,k_y,k_z) k-space coordinate.

$$S(k_x,k_y,k_z)=\iiint M_{\perp}(x,y,z)e^{-i2\pi\left(k_x x+k_y y+k_z z\right)}dxdydz$$
$$k_i=n_i\gamma G_i\Delta t_i \qquad [2.13]$$

Here n_i represents the sample number in the ith dimension. k_i can be iterated by either varying the ith dimension's gradient strength by a discrete amount, G_i, for a constant duration, Δt, or by playing a constant gradient over time and making discrete samples every Δt. Iterating k_i using a constant gradient duration but varied gradient strength is known as "phase encoding", while the latter technique, which plays a constant gradient during acquisition, or readout, is commonly referred to as "frequency encoding".

Slice or volume selection is commonly used to selectively excite only specific spatial regions for both imaging and spectroscopy. When a spatially varying magnetic field (gradient) is applied, a range of precession frequencies is induced. RF excitation pulses can be designed to only excite a specific frequency range, thus selecting a plane of known width when employed while a gradient is on. Further spatial encoding can then occur within this excited region.

There are a number of different strategies for acquiring k-space samples. The two most common are phase encoding and frequency encoding. There are also multiple strategies for acquiring MR images with unique contrast. The image contrast obtained depends on acquisition parameters that control the influence of NMR physical properties. Three physical concepts that have already been mentioned can be exploited to create distinct spatial contrast in a ^{1}H MRI: proton density (ρ_0), T_1 effects, and T_2 (as well as T_2^*) effects. While these are by no means the only sources of MRI contrast, the research

discussed in this paper will be based on them, and thus they will be given the focus here. Figure 2.3 shows an example of a ρ_0 weighted image, a T_1 weighted image, and a T_2 weighted image, all of a healthy human brain.

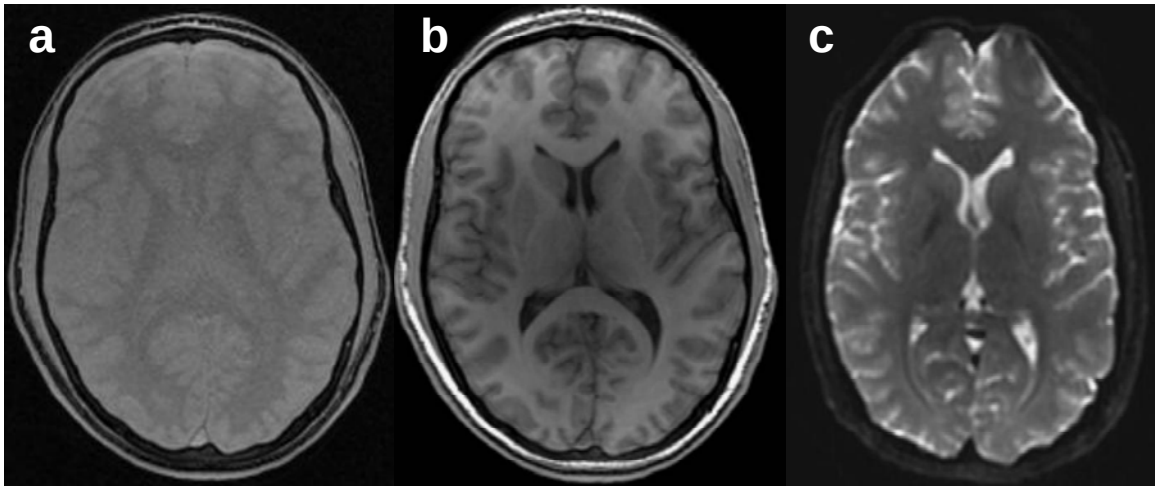

Figure 2.3. Three types of MRI contrast in a healthy human brain. A ρ_0 weighted image (a), a T_1 weighted image (b), and a T_2 weighted image (c).

Proton density (ρ_0) weighted imaging aims to acquire images with minimal influence from T_1 and T_2 effects. That is, when the receive coil is measuring the signal from the transverse magnetization, the only spatial variation in the magnitude is due to the density of protons in the tissue. In order to do this, after an RF excitation is applied, k-space should be acquired immediately, to lessen any T_2 (or T_2^*) signal decay, and the magnetization (**M**) should be given a long time to fully recover back to equilibrium (M_0), to prevent influence from T_1 effects. The time that elapses between RF excitation and k-space sampling is called the echo time (TE) and the time that elapses between consecutive RF excitations is called the repetition time (TR). A 90° RF excitation imaging sequence can be described by the following solution to the Bloch equation:

$$M_{\perp} = M_0\left(1 - e^{-TR/T_1}\right)e^{-TE/T_2^*}. \qquad [2.14]$$

To acquire an image with T_1 weighting, a TR should be used that is on the order of the T_1 values of the tissues in the image, along with a short TE. Similarly, a T_2^* weighted image can be acquired using a long TR, with a TE on the order of the tissues' T_2^* values. The influence from tissue proton densities on these images cannot be changed. Different tissues have different T_1 and T_2 (and T_2^*) values that can also vary with the size of the B_0 field. Table 2.2 shows some T_1 and T_2 values in specific tissues at 1.5T and 3.0T from literature (11,12,13,14). T_2^* values are typically much shorter than T_2 values.

Table 2.2. Some published values of estimated T_1 and T_2 values in various tissues at 1.5T and 3.0T (11,12,13,14).

	T_1 (ms)		T_2 (ms)	
Tissue	**1.5T**	**3.0T**	**1.5T**	**3.0T**
Skeletal Muscle	1130	1420	35	32
Cartilage	1060	1240	42	37
Synovial Fluid	2850	3620	1210	767
Bone Marrow	288	371	165	133
Subcutaneous Fat	288	365	165	133
White Matter	646	838	85	75
Gray Matter	1197	1607	94	83
Blood	1441	1932	290	275
Kidney	690	1194	55	56
Liver	576	812	46	42

Because typical TR values do not allow longitudinal magnetization to fully recover to equilibrium, it may take multiple excitations before the magnetization reaches a steady state. A steady state is reached when the exact amount of longitudinal magnetization that is lost in an RF excitation is recovered in a single TR. For a 90° RF excitation, steady state occurs after one excitation, but for lower RF excitation angles (flip angles, θ), it takes multiple excitations to achieve steady state. The steady state magnetization equation is similar to equation 2.14 for a given flip angle, θ:

$$M_{\perp} = \frac{M_0\left(1-e^{-TR/T_1}\right)e^{-TE/T_2^*}\sin\theta}{\left(1-\cos\theta e^{-TR/T_1}\right)} \qquad [2.15]$$

Changing θ allows for another way to alter T_1 and ρ_0 weighting.

Reversible constant external field inhomogeneities (T_2' effects) are responsible for T_2^* values being shorter than T_2 values. These effects can be undone if the spreading of the transverse magnetization they cause can be exactly reversed. T_2 and T_1 effects are not reversible, however. In a time, TE/2, after the initial RF excitation, each nuclear dipole will have precessed according to its local magnetic field environment – including external inhomogeneities. If each nuclear dipole is then inverted in the transverse plane, each dipole will be in a location as if it had been precessing in the opposite direction. Now, when they continue to precess, as they had done before the inversion, the dipoles will return to their alignment just prior to the initial RF excitation at the echo time, TE, less the signal decay from T_2 effects. This technique is known as a spin-echo, and the inversion can be accomplished by applying a 180° RF excitation after the initial RF pulse. A spin-echo is necessary to acquire a T_2 weighted image.

Another common technique to achieve T_1 weighting is inversion recovery. If a 180° RF inversion pulse is applied at equilibrium, the net magnetization will fully invert along $\mathbf{B_0}$. The net magnetization will then recover to equilibrium, according to T_1 effects. Thus, during its recovery, the magnitude of the net magnetization will first decay, until it reaches a null point, and then increase towards equilibrium, M_0. If a 90° excitation pulse is applied at some "inversion time" (TI) during the net magnetization's recovery, further T_1 contrast is available. If the TI occurs at exactly the time a specific tissue experiences the null point, the image will have no signal contribution from that tissue. Inversion

recovery techniques can be used in conjunction with other contrast weighting techniques to eliminate unwanted signal. Two common inversion recovery techniques include fluid attenuated inversion recovery (FLAIR), where the signal from cerebral spinal fluid (CSF) is nulled, and short tau inversion recovery (STIR), which eliminates signal from fat. Figure 2.4 shows a pulse sequence diagram (PSD) for a general spin-echo 3D acquisition with inversion recovery.

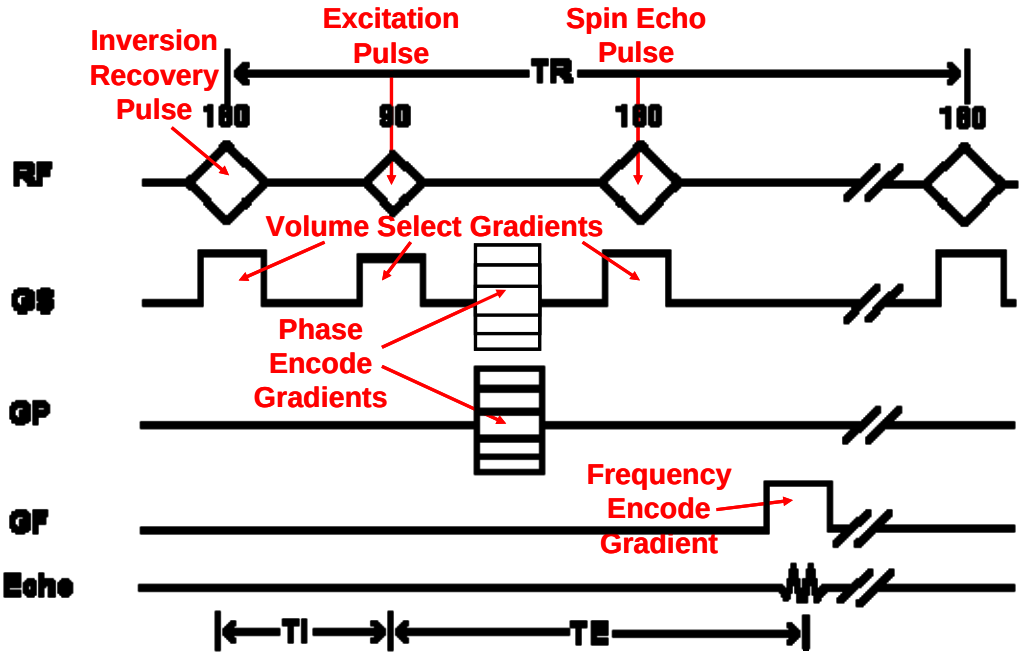

Figure 2.4. Pulse sequence diagram of a general 3D MRI acquisition with an inversion recovery and a spin echo pulse (modified from reference 15). Time goes from left to right. RF denotes the time sequence of the RF excitation pulses, with angles labeled. GS is the volume-select gradient in dimension *z*, with phase encoding; GP is the phase encoding gradient for dimension *y*; and GF is the frequency encoding gradient for dimension *x*. TI, TE, and TR are also labeled. Data are acquired while the frequency encoding gradient is played.

2.5 Magnetic Resonance Spectroscopic Imaging (MRSI)

NMR spectroscopy and MRI can be performed simultaneously to acquire images with an additional spectral dimension, or spatially resolved chemical shifts. This is known as chemical shift imaging (CSI) or magnetic resonance spectroscopic imaging (MRSI).

Typically MRSI data are acquired by phase encoding all spatial dimensions to prevent complications that a readout gradient can have on the spectroscopic dimension. However, this technique can be quite time consuming as three-dimensional MRSI (3D-MRSI) datasets can require a large number of RF excitations to employ k-space acquisition via phase encoding. Thus, there have been many alternative 3D-MRSI acquisition techniques developed to reduce acquisition time (t_{ACQ}), several of which use a spatially encoding gradient during data acquisition.

Because the signal from the molecules often being probed is much smaller than the signal from water protons (and sometimes lipid protons), additional techniques are necessary to improve data quality. Specifically, two techniques that are commonly used to improve spectral quality are outer volume suppression pulses and spectral suppression pulses. A volume can be selected using multiple slice selecting RF excitations in different dimensions, known as point resolved spectroscopy (PRESS). Signal from outside this selection, or PRESS box can be further suppressed using specialized slice selecting pulses coupled with spoiler gradients. These pulses are known as VSS pulses, or very selective saturation pulses, due to their very sharp transition bands (16). Additionally, signal within specific spectral regions may be suppressed by saturating a specific spectral range (in all space) via chemical shift selective saturation (CHESS) pulses (17). By

applying CHESS pulses tuned to the spectral region containing water, NMR signal from less prevalent chemical species with chemical shifts near water can be more reliably measured. Figure 2.5 shows one slice of a 3D-MRSI dataset acquired on a healthy human brain.

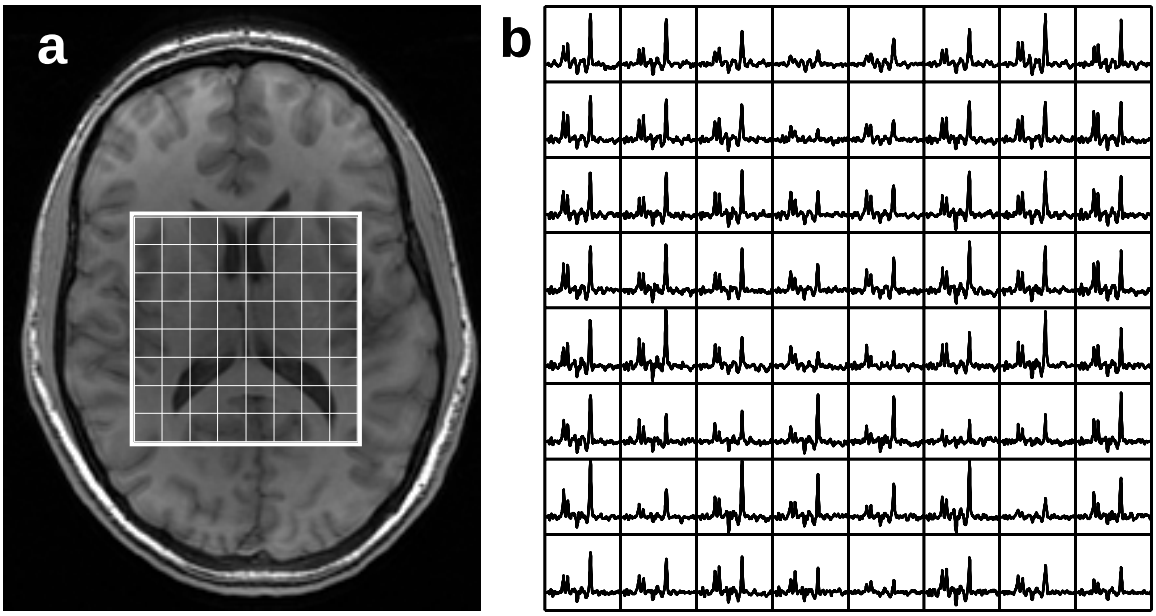

Figure 2.5. One slice of a three-dimensional magnetic resonance spectroscopic image (3D-MRSI) of a healthy human brain is shown. A T_1 weighted image is shown with an overlaying grid (a). The adjacent grid (b) shows the NMR spectra for each 1 cm^3 voxel represented in the grid in 5a. The spectral bandwidth focuses on the range between 0.5 and 4.0 ppm. As in Figure 2.2, Cho, Cre, and NAA peaks are most prominent.

2.6 Summary

Because of the wide array of information available through probing the nuclear magnetic resonance characteristics of chemicals and tissues, NMR technologies have become increasingly influential in the biochemistry and medical research fields. The search for biomarkers for multiple diseases and illnesses has thus benefited greatly from advances in NMR technologies. Specifically, NMR techniques have revealed unique and

clinically useful morphological, functional, and metabolic information about cancer. Moreover, the future of cancer research will benefit significantly as NMR technologies advance.

2.7 References

1. Cancer Statistics 2008. American Cancer Society. <http://www.cancer.org/docroot/PRO/content/PRO_1_1_Cancer_Statistics_2008_Presentation.asp>.
2. Central Brain Tumor Registry of the US data – 2000-2004. CBTRUS. <http://www.cbtrus.org/>.
3. Statistics. Accelerate Brain Cancer Cure. <http://www.abc2.org/statistics.shtml>.
4. Uddin, A., T. Jarmi, S. Hariha, Glioblastoma Multiforme. 2005.
5. Gleason DF. The Veteran's Administration Cooperative Urologic Research Group: histologic grading and clinical staging of prostatic carcinoma. In Tannenbaum M (ed.) Urologic Pathology: The Prostate. Lea and Febiger, Philadelphia, 1977; 171-198.
6. Balk SP, Ko Y-J, Bubley GJ. Biology of Prostate-Specific Antigen. Journal of Clinical Oncology, 2003. 28 (2): 383–91.
7. Nelson SJ. Analysis of volume MRI and MR spectroscopic imaging data for the evaluation of patients with brain tumors. Magn Reson Med. 2001 Aug;46(2):228-39.
8. Daldrup H, Shames DM, Wendland M, Okuhata Y, Link TM, Rosenau W, Lu Y, Brasch RC. Correlation of dynamic contrast-enhanced magnetic resonance imaging with histologic tumor grade: comparison of macromolecular and small-molecular contrast media. Pediatr Radiol. 1998 Feb;28(2):67-78.
9. Ross BD. The biochemistry of living tissues: examination by MRS. NMR Biomed. 1992 Sep-Oct;5(5):215-9. Review
10. The Theory of NMR. University of Colorado, Boulder, Chemistry and Biochemistry Department, 2003. <http://orgchem.colorado.edu/hndbksupport/nmrtheory/protonchemshift.html>.
11. Han E, Gold G, Stainsby J, Wright G, Beaulieu C, Brittain J. 1In-Vivo T1 and T2 Measurements of Muskuloskeletal Tissue at 3T and 1.5T. Proceedings 11th Scientific Meeting ISMRM, Toronto, Canada, 2003. #450
12. Lu H, Nagae-Poetscher LM, Golay X, Lin D, Pomper M, van Zijl PC. Routine clinical brain MRI sequences for use at 3.0 Tesla. J Magn Reson Imaging. 2005 Jul;22(1):13-22.
13. Wright PJ, Mougin OE, Totman JJ, Peters AM, Brookes MJ, Coxon R, Morris PE, Clemence M, Francis ST, Bowtell RW, Gowland PA. Water proton T1 measurements in brain tissue at 7, 3, and 1.5 T using IR-EPI, IR-TSE, and MPRAGE: results and optimization. MAGMA. 2008 Mar;21(1-2):121-30. Epub 2008 Feb 8.

14. Stanisz GJ, Odrobina EE, Pun J, Escaravage M, Graham SJ, Bronskill MJ, Henkelman RM. T1, T2 relaxation and magnetization transfer in tissue at 3T. Magn Reson Med. 2005 Sep;54(3):507-12.
15. MRI Pulse Sequences. Ray Ballinger. <http://www.mritutor.org/mritutor/invers.htm>.
16. Tran TK, Vigneron DB, et al. Very selective suppression pulses for clinical MRSI studies of brain and prostate cancer. Magn Reson Med. 2000 Jan;43(1):23-33.
17. Haase A, Frahm J, Hänicke W, Matthaei D. 1H NMR chemical shift selective (CHESS) imaging. Phys Med Biol. 1985 Apr;30(4):341-4.

Chapter 3: Kinetic Modeling and Metabolism in MR

3.1 Basics of MR Contrast in Cancer

NMR techniques have been developed to reveal unique contrasts between cancerous and healthy tissue. MRI with and without the injection of an exogenous contrast agent has become a common procedure for diagnostic studies to define tumor boundaries and guide biopsy locations (1,2,3). MRSI has also been shown to be beneficial in distinguishing aggressive malignant tumors from less dangerous benign tumors (2,4,5).

Magnetic resonance imaging using T_1 and T_2 weighting has been helpful in clinical settings to aid in characterizing brain tumors. Specifically, T_2 weighted images have been used to distinguish healthy gray and white matter from tumor. T_2 values in cancerous tissue tend to be lower than the rest of the neural tissue, except cerebral spinal fluid (CSF), due to less confined tissue structure and more edema. Thus, with the right echo time, images can be acquired to show much brighter cancerous tissue than the normal surroundings. A fluid attenuated inversion recovery (FLAIR) sequence can also be incorporated to suppress the signal from CSF and make the tumor delineation even more apparent. Similar MR tissue contrast can also be seen in other organs.

MRIs acquired after the injection of a gadolinium (Gd) chelate have been useful in designating boundaries of blood vessel leakage and tumor blood volume. Gadolinium acts to increase the T_1 and T_2^* effects due to its seven unpaired electrons in its 3+ oxidation state, and thus will cause a brighter signal in a T_1 weighted acquisition and darker signal in a T_2^* weighted image. This is especially useful in the brain, where

healthy tissue normally has an intact blood brain barrier (BBB), preventing the chelate from leaving the blood vessels. In an aggressive glioma, the BBB can be compromised due to proliferative activity, and the presence of the chelate will cause cancerous tissue to change its contrast after gadolinium injection. Cancerous tissues outside the brain also show an increased gadolinium influence compared to normal tissue, most likely due to increased blood vessel density and disrupted endothelial vessel walls. However, it is important to note that larger sized Gd compounds may be more effective in demonstrating differences in Gd uptake outside the brain (6).

NMR spectroscopy has also been used to show relevant correlations with tumor malignancy in the brain, breast, and prostate (7,8,9). N-acetyl aspartate (NAA) is a chemical associated with neuronal function and should be lower than normal in areas of malignant glioma. Choline containing compounds (Cho), such as phosphorylcholine (PC) and glycerophosphorylcholine (GPC), as well as free choline, are affiliated with cell membrane turnover and are indicative of tumor growth in multiple tissues. Lactate (Lac) is a byproduct of anaerobic respiration, indicative of oxygen deficiency, and may predict tumor necrosis, while the presence of mobile lipids (Lip) in a tumor may already imply necrosis. Citrate is an intermediate of the Kreb's cycle which may be associated with healthy prostate tissue (10). All of these MR-derived parameters may be associated with tumor staging criteria and thus can be useful for tumor classification.

3.2 Kinetic Modeling

Kinetic modeling involves the optimization of parameters of one or more mathematical equations to help describe observed variations in acquired data. Modeling has become a widely accepted technique in many disciplines from economics to biology.

It is now commonly used to investigate the pharmacokinetics of drugs, including characterization of their metabolism and clearance. Many imaging procedures have also benefited from kinetic modeling (7), including MRI. By combining kinetic modeling with medical imaging, quantitative descriptions of the interconnections of several physiological processes are now possible in vivo. Processes such as transport, metabolism, and receptor binding can be routinely probed based on imaging tracer concentration profiles over time. Multiple techniques are available that use MRI to acquire tracer concentration weighted images. When acquired sequentially, these images can be used for fitting particular kinetic models that describe various physiological processes.

Gadolinium (Gd) is a metal element in the Lanthanide series that possesses strong paramagnetic properties. In its 3+ oxidation state, it has seven unpaired electrons that can considerably influence T_1, T_2, and T_2^* effects. When combined with a chelating agent, such as diethylenetriamine penta-acetate (DTPA), it can form a relatively inert compound that can be injected into human subjects undergoing a subsequent MRI. If MR images are acquired sequentially after introducing this exogenous and inert agent, a spatially varying time course of Gd contrast can be viewed. This is known as dynamic contrast enhanced MRI (DCE-MRI), and can be acquired with various contrast weightings.

Because Gd shortens T_1, and T_2^*, a T_1 weighted image will appear brighter where Gd is present, while a T_2^* weighted image will appear darker. The change in the inverse of these time constants, called relaxation rates (R_1 and R_2^*) is nearly linearly related to the concentration of Gd (6,12). Thus by monitoring the image signal intensity over time, an

estimate of the Gd concentration time course can be used in a kinetic modeling technique to describe the physiological processes occurring in the various tissues.

DCE-MRI has been used to model vascular density and permeability, as well as blood flow in many tissues and diseases (3,6,13,14). Most of these techniques have relied on tracer models for capillary permeability developed by Renkin (15), Crone (16), and Johnson et al. (17). Kenney et al. (18) have used kinetic modeling to estimate the permeability surface area product (PS) of the blood-brain barrier (BBB) and fractional volume of blood (f_{BV}) in brain tissue using Gd-DTPA enhanced MRI. Daldrup (6), Roberts (2), and Boxerman (19) have expanded on these methods to show that DCE-MRI can be used to non-invasively quantify vascular density and permeability of multiple tumor tissues in both T_1 weighted and T_2^* weighted techniques using various sized Gd compounds.

The main differences in these techniques are usually image quality and temporal resolution. T_1 weighted images, usually acquired with a 3D fast spoiled gradient acquisition in steady state (FSPGR) sequence, generally take longer to acquire and thus have poorer temporal resolution (~5-30sec) with relatively good image quality. T_2 and T_2^* weighted DCE images are usually acquired using 2D echo-planar imaging (EPI) techniques with finer temporal resolution (~1-2sec) but compromised image quality. Higher temporal resolution techniques necessitate a first-pass modeling method to account for the injected bolus shape, while lower temporal resolution methods tend to assume the tracer to be instantaneously well mixed, and usually acquire data for a longer post-injection duration. This difference affects how the bolus input is modeled. Most modeling techniques (using T_1, T_2 or T_2^* data) assume a compartmental relationship

between intravascular extracellular space and extravascular extracellular space, but may differ in how they model the bolus input. Some modeling techniques have gone as far as to account for tracer convection through vasculature (20). However, some techniques do not use a vascular input function, or any tissue exchange model at all (13,14). Such methods usually rely on heuristic parameters for relevant information. Which particular DCE-MRI technique is most useful for assessing tumor characteristics is still not known.

Equation 3.1 shows a general equation for the time concentration of Gd in tissue used for the modeling of the tissue exchange of Gd-DTPA.

$$C_V(t) = f_{BV} C_B(t) + K^{PS} \int_0^t C_B(\tau)^{-k_{ep}(t-\tau)} d\tau \qquad [3.1]$$

Here C_V represents Gd concentration in a given volume V. C_V has contributions from both tissue, or extravascular space, and blood, or intravascular space (C_B). The rate constant for the leakage of Gd from blood vessels is K^{PS}, while the reverse rate constant is k_{ep}. The fractional volume of blood in any given region is represented by f_{BV}. The parameters K^{PS}, k_{ep}, and f_{BV} are routinely estimated as biomarkers for tumor malignancy. Kinetic modeling of DCE-MRI data can thus improve the diagnostic capabilities of Gd enhanced MRI by probing the underlying kinetic processes involved.

3.3 Cancer Metabolism

Cancer is a complex disease with multiple characteristic traits; perhaps most inherent is its abnormal metabolism. Cancer metabolism can be marked by various abnormalities, which can be probed through multiple techniques. MR spectroscopy offers a promising spectrum of non-invasive techniques to investigate abnormal cancer metabolism by studying the amount of specific metabolites present in tissues. For

example, healthy brain tissue will contain a relatively high amount of N-acetyl aspartate (NAA), signifying normal neuronal function, with a lower amount of choline containing compounds (Cho), markers of cell division and proliferation. Healthy tissue also does not contain a large of amount of lactate (Lac), in general. However, in a malignant glioma, tissue may contain no NAA with large amounts of Cho and/or Lac. NAA decreases and Cho increases in a glioma due to lack of normal cellular function and the high cellular turnover rate associated with cancer. The presence of Lac may be due to various reasons: hypoxia due to insufficient blood supply, which leads to anaerobic lactate production; or the Warburg effect (21), in which cancer cells preferably undergo lactate fermentation, instead of normal aerobic metabolism, even though oxygen is present. The Warburg effect is present in nearly all known cancers (22).

Two strategies can be employed when investigating metabolism with NMR spectroscopy and MRSI. One involves investigating the amount of endogenous metabolites already present within a volume, thus non-invasively probing the steady state metabolic state (non-dynamic). The other involves injecting an exogenous metabolically active material and monitoring its progression through the body and into other metabolites (dynamic). Both techniques are used and are extremely useful in cancer research.

3.4 Improving ^{1}H 3D-MRSI Acquisitions

A common technique for studying non-dynamic endogenous metabolites within tissues is ^{1}H MRSI. This has been particularly significant in brain tumor research (7), but also in prostate and breast cancer research (8,9). Because gliomas are often extremely heterogeneous, single voxel MRS and 2D-MRSI of the brain can be error prone. 3D-

MRSI allows for the most comprehensive information, but, as mentioned in chapter 2, it can suffer from a low signal to noise ratio (SNR) as well as long acquisition times (t_{ACQ}). Thus, multiple techniques have been developed to improve 3D-MRSI by increasing SNR and/or speeding up acquisition times.

Increasing the static B_0 field and simultaneously incorporating multiple receive coils has improved SNR in MRSI studies without compromising relevant metabolite tissue contrast (25,26). This SNR increase can then be used to either improve the spatial resolution of the data with a similar acquisition time or to maintain the spatial resolution and shorten the acquisition time. The traditional method for encoding spectral data in k-space relies on multiple phase encoding steps, and thus RF excitations. The time required to obtain each phase encoded k-space point depends linearly upon the repetition time (TR) for a given echo time (TE). Reducing the time needed to acquire the data requires the implementation of novel k-space sampling strategies, such as: ellipsoidal k-space encoding (27), parallel imaging reconstruction (28), or time varying readout gradient trajectories, like spiral spectroscopic imaging (29) and echo-planar spectroscopic imaging (EPSI) (30). Which time reducing technique is most appropriate for a particular setting is still not fully known.

3.5 Hyperpolarized ^{13}C Spectroscopy

Nuclei other than ^{1}H have also been used to study cancer and its abnormal metabolism. Common alternative nuclei consist mainly of Phosphorus-31 (^{31}P), Nitrogen-15 (^{15}N), and Carbon-13 (^{13}C). These elements are involved in most important metabolic reactions and can therefore reveal important metabolic information. However, these nuclei tend to have lower measurable signal than ^{1}H due to lower concentration in the

body, lower isotopic natural abundance, or lower NMR sensitivity ($\propto \gamma^3$). In vivo spectroscopic studies of ^{13}C and ^{15}N tend to suffer from low SNR mainly due both to low natural abundance (<2% for each) and low NMR sensitivity (<2% of ^{1}H for each). Although ^{31}P has a 100% isotopic natural abundance, its sensitivity is less than 7% that of 1H, thus 31P spectroscopy also tends to suffer from low SNR. Nevertheless, the recent development of dynamic nuclear polarization (DNP) can excite many more ^{13}C nuclei to the aligned spin state, thus increasing the ^{13}C NMR signal intensity by more than 10,000-fold (31). DNP has allowed for dramatic improvements in the ability to study in vivo ^{13}C metabolism (32,33,34), by introducing an exogenous compound that is metabolically active. Thus, with dynamic hyperpolarized ^{13}C spectroscopy, kinetic and metabolic information is available in vivo and in real time, and a kinetic model can be applied to estimate useful physiologic parameters. With further improvements and innovations to this relatively new technology, great scientific progress into cancer research may be just on the horizon.

3.6 References

1. Bydder GM, Steiner RE, Young IR, Hall AS, Thomas DJ, Marshall J, Pallis CA, Legg NJ. Clinical NMR imaging of the brain: 140 cases. AJR Am J Roentgenol. 1982 Aug;139(2):215-36.
2. Roberts, H., et al., Quantitative measurement of microvascular permeability in human brain tumors achieved using dynamic contrast-enhanced MR imaging: correlation with histologic grade. AJNR Am J Neuroradiol, 2000. 21(5): p. 891-899.AJNR Am J Neuroradiol. 1992 Nov-Dec;13(6):1555-64.
3. Noworolski SM, Henry RG, Vigneron DB, Kurhanewicz J. Dynamic contrast-enhanced MRI in normal and abnormal prostate tissues as defined by biopsy, MRI, and 3D MRSI. Magn Reson Med. 2005 Feb;53(2):249-55.
4. Preul, M., et al., Accurate, noninvasive diagnosis of human brain tumors by using proton magnetic resonance spectroscopy. Nat Med, 1996. 2(3): p. 323-325.
5. Kurhanewicz J, Vigneron DB, Hricak H, Narayan P, Carroll P, Nelson SJ. Three-dimensional H-1 MR spectroscopic imaging of the in situ human prostate with high (0.24-0.7-cm3) spatial resolution. Radiology. 1996 Mar;198(3):795-805.

6. Daldrup H, Shames DM, Wendland M, Okuhata Y, Link TM, Rosenau W, Lu Y, Brasch RC. Correlation of dynamic contrast-enhanced magnetic resonance imaging with histologic tumor grade: comparison of macromolecular and small-molecular contrast media. Pediatr Radiol. 1998 Feb;28(2):67-78.
7. Nelson SJ. Analysis of volume MRI and MR spectroscopic imaging data for the evaluation of patients with brain tumors. Magn Reson Med. 2001 Aug;46(2):228-39.
8. Katz-Brull R, Lavin PT, Lenkinski R (2002) Clinical utility of proton magnetic resonance spectroscopy in characterizing breast lesions. J Natl Cancer Inst 94:1197-1203.
9. Kurhanewicz J, Dahiya R, Macdonald JM, Chang LH, James TL, Narayan P. Citrate alterations in primary and metastatic human prostatic adenocarcinomas: 1H magnetic resonance spectroscopy and biochemical study. Magn Reson Med. 1993 Feb;29(2):149-57.
10. Cooper JF, Imfeld H. The role of citric acid in the physiology of the prostate: a preliminary report. Trans West Sect Am Urol Assoc. 1958;25:153-61
11. Price JC. Principles of tracer kinetic analysis. Neuroimaging Clin N Am. 2003 Nov;13(4):689-704.
12. Rosen BR, Belliveau JW, Vevea JM, Brady TJ. Perfusion imaging with NMR contrast agents. Magn Reson Med 1990; 14: 249-265.
13. Lee, M., et al., Dynamic Susceptibility Contrast Perfusion Imaging of Radiation Effects in Normal-Appearing Brain Tissue: Changes in the First-Pass and Recirculation Phases. J Magn Reson Imaging, 2005. 21(6): p. 683-693.
14. Lupo, J., et al., Dynamic susceptibility-weighted perfusion imaging of high-grade gliomas: characterization of spatial heterogeneity. AJNR Am J Neuroradiol, 2005. 26(6): p. 1446-1454.
15. Renkin EM. Transport of potassium-42 from blood to tissue in isolated mammalian skeletal muscles. Am J Physiol. 1959 Dec;197:1205-10.
16. Crone C. The Permeability Of Capillaries In Various Organs As Determined By Use Of The 'Indicator Diffusion' Method. Acta Physiol Scand. 1963 Aug;58:292-305.
17. Johnson JA, Wilson TA. A model for capillary exchange. Am J Physiol. 1966 Jun;210(6):1299-303.
18. Kenney J, Schmiedl U, Maravilla K, Starr F, Graham M, Spence A, Nelson J. Measurement of blood-brain barrier permeability in a tumor model using magnetic resonance imaging with gadolinium-DTPA. Magn Reson Med. 1992 Sep;27(1):68-75.
19. Boxerman JL, Schmainda KM, Weisskoff RM. Relative cerebral blood volume maps corrected for contrast agent extravasation significantly correlate with glioma tumor grade, whereas uncorrected maps do not. AJNR Am J Neuroradiol. 2006 Apr;27(4):859-67.
20. Lee, T., T. Purdie, and E. Stewart, CT Imaging of Angiogenesis. QJ Nucl Med, 2003. 47(3): p. 171-187.
21. Warburg O. On the origin of cancer cells. Science. 1956 Feb 24;123(3191):309-14.
22. Kim JW, Dang CV. Cancer's molecular sweet tooth and the Warburg effect. Cancer Res, 2006. 66 (18): 8927–30.

23. Govindaraju V, Gauger GE, Manley GT, Ebel A, Meeker M, Maudsley AA. Volumetric proton spectroscopic imaging of mild traumatic brain injury. AJNR Am J Neuroradiol. 2004 May;25(5):730-7.
24. Laprie A, Pirzkall A, et al. Longitudinal multivoxel MR spectroscopy study of pediatric diffuse brainstem gliomas treated with radiotherapy. Int J Radiat Oncol Biol Phys. 2005 May 1;62(1):20-31.
25. Li Y, Osorio JA, et al. Considerations in applying 3D PRESS H-1 brain MRSI with an eight-channel phased-array coil at 3 T. Magn Reson Imaging. 2006 Dec;24(10):1295-302. Epub 2006 Oct 18.
26. Osorio JA, Ozturk-Isik E, et al. 3D 1H MRSI of brain tumors at 3.0 Tesla using an eight-channel phased-array head coil. J Magn Reson Imaging. 2007 Jul;26(1):23-30.
27. Maudsley AA, Matson GB, Hugg JW, Weiner MW. Reduced phase encoding in spectroscopic imaging. Magn Reson Med. 1994 Jun;31(6):645-51.
28. Dydak U, Weiger M, Pruessmann KP, Meier D, Boesiger P. Sensitivity-encoded spectroscopic imaging. Magn Reson Med. 2001 Oct;46(4):713-22.
29. Adalsteinsson E, Irarrazabal P, Topp S, Meyer C, Macovski A, Spielman DM. Volumetric spectroscopic imaging with spiral-based k-space trajectories. Magn Reson Med. 1998 Jun;39(6):889-98.
30. Posse S, Tedeschi G, Risinger R, Ogg R, Le Bihan D. High speed 1H spectroscopic imaging in human brain by echo planar spatial-spectral encoding. Magn Reson Med. 1995 Jan;33(1):34-40.
31. Ardenkjaer-Larsen JH, Fridlund B, Gram A, Hansson G, Hansson L, Lerche MH, Servin R, Thaning M, Golman K. Increase in signal-to-noise ratio of > 10,000 times in liquid-state NMR. Proc Natl Acad Sci U S A. 2003 Sep 2;100(18):10158-63. Epub 2003 Aug 20.
32. Golman K, Zandt RI, Lerche M, Pehrson R, Ardenkjaer-Larsen JH. Metabolic imaging by hyperpolarized 13C magnetic resonance imaging for in vivo tumor diagnosis. Cancer Res. 2006 Nov 15;66(22):10855-60.
33. Chen AP, Albers MJ, Cunningham CH, Kohler SJ, Yen YF, Hurd RE, Tropp J, Bok R, Pauly JM, Nelson SJ, Kurhanewicz J, Vigneron DB. Hyperpolarized C-13 spectroscopic imaging of the TRAMP mouse at 3T-initial experience. Magn Reson Med. 2007 Dec;58(6):1099-106.
34. Golman K, in 't Zandt R, Thaning M. Real-time metabolic imaging. Proc Natl Acad Sci U S A. 2006 Jul 25;103(30):11270-5. Epub 2006 Jul 12.

Chapter 4: Comparison of T_1 Weighted and T_2^* Weighted DCE-MRI Modeling Techniques in Human Brain Tumor Patients

4.1 Abstract

Purpose: To compare T_2^* and T_1 weighted DCE-MRI modeling techniques and investigate their usefulness in characterizing brain tumors.

Methods: Kinetic parameters for blood volume (f_{BV} and CBV) and endothelial leakage (K^{PS} and k_{T2*}) were estimated from T_2^* and T_1 weighted DCE-MRI data. Regions of interest (ROIs) representing normal appearing white matter (NAWM) and gray matter (NAGM) and contrast enhancing lesions (CEL) were manually drawn and parameters were compared across them. Blood volume parameters were compared to previously published values. Statistical tests were performed to assess any relationship between parameters and tumor grade and any differences between parameter values normalized to NAWM (MCR: malignancy contrast ratio) in grade 4 patients.

Results: Both methods' blood volume parameters correlated well with literature. K^{PS} and k_{T2*} each showed a significant correlation with tumor grade, while f_{BV} and CBV did not. Median MCR values were significantly higher in T_1 derived parameters compared to T_2^* derived parameters ($MCR_{KPS} = 9.21$, $MCR_{fBV} = 5.44$, $MCR_{kT2*} = 1.95$, $MCR_{CBV} = 2.52$).

Conclusion: T_1 derived parameters may be more beneficial than T_2^* derived parameters in assessing human gliomas. Specifically, K^{PS} showed the largest contrast ratio for tumor compared to NAWM and had the strongest correlation with WHO tumor grade.

4.2 Introduction

Cancer is a complex disease that involves multiple physiologic changes and abnormalities of tissue. One important functional change associated with cancer is the development of vascular networks to feed the rapidly growing tissue. This angiogenesis is often associated with increased blood vessel leakage, due to the disorganized structure of the hastily growing endothelial network. This change may be most noticeable in the brain, where healthy tissue does not receive much of the blood's content due to the blood brain barrier (BBB). This barrier acts to block unwanted pathogens and chemical substances, while still allowing essential nutrients to be delivered to neural tissue.

When brain tissue becomes cancerous, the coupled angiogenesis often compromises the BBB, leading to significant endothelial leakage. The increase of blood vessel density and vascular leakage can be investigated in vivo using MRI with an exogenous contrast agent, such as a gadolinium (Gd) chelate. Gadolinium increases the influence of T_1 and T_2^* effects, and thus, if present, will cause tissue in a T_1 weighted MRI to appear brighter and tissue in a T_2^* weighted image to appear darker. Figure 4.1 shows an example of this in a glioma patient. Current clinical MRI procedures often include a post-contrast T_1 weighted image, acquired a few minutes after the Gd injection. These post-Gd images can be helpful in defining tumor boundaries and helping guide biopsy locations; however, they do not allow for the quantitative estimation of the processes behind the Gd transport.

Tracer kinetic modeling can be used to probe in vivo physiologic processes such as transport, metabolism, and receptor binding based on images of tracer concentration profiles over time. Thus, if sequential MR images are acquired after Gd is administered,

tracer kinetic modeling can be used to estimate transport kinetics and functional changes in the diseased tissue. This dynamic acquisition technique is known as dynamic contrast enhanced MRI (DCE-MRI).

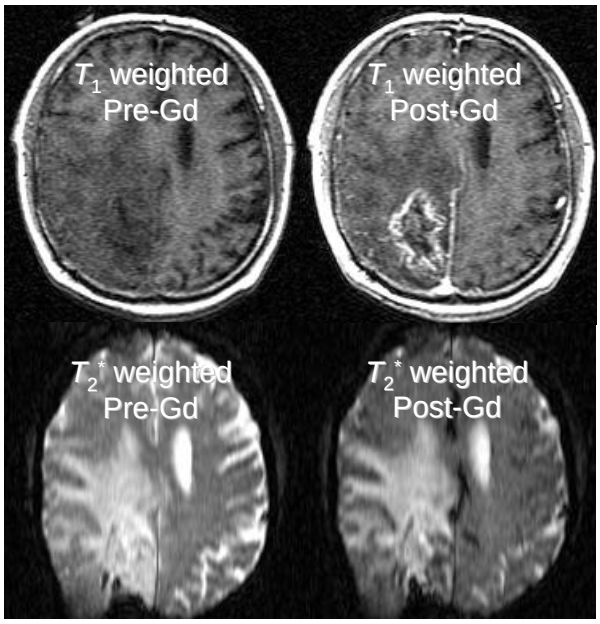

Figure 4.1. Before and after Gd injection. T_1 weighted images (top) show an increased signal intensity in vessels and tumor rim, while T_2^* weighted images (bottom) show signal dropout in blood vessels and near the tumor.

Because Gd shortens T_1 and T_2^*, DCE-MRI can be performed with either T_1 or T_2^* weighting. The change in the inverse of these time constants, called relaxation rates (R_1 and R_2^*), has been shown to be nearly linearly related to the concentration of Gd (1,2). Thus, ΔR_1 or ΔR_2^* images can be constructed with voxels that are proportional to the Gd concentration time course, and both can be used in a kinetic modeling procedure to estimate parameters corresponding to blood vessel density and leakage rate.

The main differences between T_1 weighted and T_2^* weighted modeling techniques are associated with image acquisition parameters. T_1 weighted acquisitions need a short echo time (TE) and repetition time (TR) to lessen T_2^* decay and allow for T_1 contrast. A

3D acquisition technique known as fast spoiled gradient acquisition at steady state (FSPGR) is commonly used for this purpose. At each time point, a 3D k-space matrix is acquired and then Fourier transformed into image space. T_2^* weighted acquisitions require a longer TE to allow for T_2^* contrast and a long TR to inhibit T_1 effects. The long TR necessary for T_2^* weighting would make a 3D acquisition very time consuming, so a multislice 2D acquisition is preferred. An echo-planar image (EPI) acquisition is commonly used for T_2^* weighting, where multiple 2D images can be acquired in one TR by sequentially exciting neighboring slices within the volume while the previously selected slices return to T_1 equilibrium. Each 2D slice is acquired in one RF excitation, allowing for rapid imaging (typically 1-2 seconds), but the quality can be compromised due to lower spatial resolution, chemical shift artifacts, and geometric distortion. The T_1 weighted images also have a tradeoff, and are usually acquired with a lower temporal resolution (~5-30 seconds), but with higher image quality and spatial resolution.

DCE-MRI methods with higher temporal resolution often incorporate a first pass technique to account for the injected bolus shape as it passes through the tissue, while lower temporal resolution methods tend to assume the first pass effect to be negligible and the tracer to be instantaneously well mixed. Higher temporal resolution techniques also tend to have shorter acquisition durations and focus on the initial kinetic changes (within the first two minutes). Lower temporal resolution techniques usually acquire data for a longer post-injection duration, focusing more on the tracer's extravasation. However, both modeling techniques assume a compartmental relationship between intravascular and extravascular space.

This study compares the modeling methods for T_1 weighted and T_2^* weighted DCE-MRI datasets, which are acquired sequentially in one exam. Specifically, estimated parameters from lower temporal resolution, high image quality T_1 weighted DCE-MRI data were compared with estimated parameters from higher temporal resolution, lower image quality T_2^* weighted DCE-MRI data to assess any differences in their ability to characterize human gliomas. Estimated parameters corresponding to blood volume from each technique were also compared to literature values to assess their validity.

4.3 Methods

4.3.1 Patients and Data Acquisition

This study was a retrospective analysis on data acquired from July 8th, 2002 through August 1st, 2006. T_1 weighted and T_2^* weighted DCE-MRIs were performed on a 1.5T Signa Echospeed scanner (GE Medical Systems, Milwaukee, WI) with a birdcage volume head coil. Eleven newly diagnosed glioma patients (three WHO grade 2, two WHO grade 3, and six WHO grade 4), two recurrent grade 4 glioma patients, and nine other brain tumor patients underwent contrast enhanced MR imaging. All patients received a T_1 weighted 3D-FSPGR DCE-MRI scan (N=12, FOV=26x26x8.4cm^3, res=1.02x1.02x3mm^3, TR=6.5ms, TE=1.25ms, flip angle = 30°, t_{ACQ}=6.2min) followed by a single T_1 weighted 3D-FSPGR scan (FOV=26x26x17.4cm^3, res=1.02x1.02x1.5mm^3) and a T_2^* weighted 2D-EPI DCE-MRI scan (N=60, FOV=26x26x4.2cm^3, res=2.03x2.03x6mm^3 (7 slices), TR=2000ms, TE=54ms, flip angle = 35°, t_{ACQ}=2min). Each DCE-MRI scan was preceded by an injection of 20 mL Gd diethylenetriamine penta-acetate (Gd-DTPA) at 1 mL sec^{-1} for T_1 weighted DCE-MRI and 3–4 mL sec^{-1} for

T_2^* weighted DCE-MRI. All patients provided informed consent as required by our institutional review board.

For all patients, representative regions of interest (ROIs) for contrast enhancing lesion (CEL), normal appearing white matter (NAWM), and normal appearing gray matter (NAGM) were manually drawn on the post-Gd T_1 weighted image, after it had been resampled to the resolution of the T_1 weighted DCE-MRI. Maps of T_2^* derived parameters were resampled to this same resolution. One grade 2 and one grade 3 glioma patient did not show any enhancement on the post-Gd images, thus only NAWM and NAGM ROIs were available. Only NAWM and NAGM ROIs were used for the nine other non-glioma patients, although ROIs of CEL were available. Figure 4.2 shows a representative example of how the ROIs were drawn. CEL was used to define the tumor.

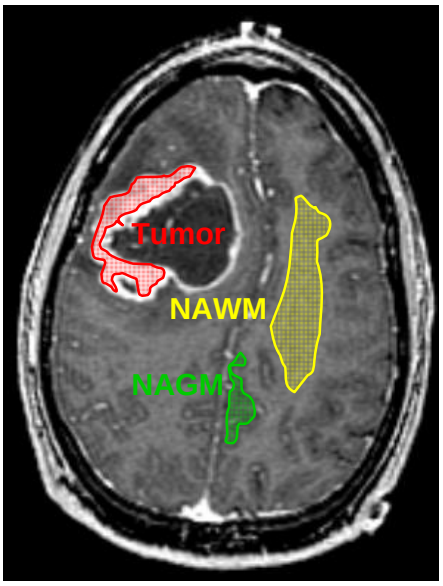

Figure 4.2. Representative ROI image. CEL (red), NAWM (yellow), and NAGM (green) are shown, overlaid on one slice of the post-Gd FSPGR image.

4.3.2 Modeling

T_1 and T_2^* DCE-MRI data do not directly relate to Gd concentration ([Gd]) after they are acquired, and mathematical manipulation is necessary to get dynamic images that correspond to Gd concentration. For T_1 data, it is assumed that the change in signal intensity (ΔS_1) resulting from the Gd injection is proportional to Gd concentration. That is, by subtracting an image acquired before Gd injection (S_{10}) from all post-injection images, a dynamic ΔS_1 data set is produced.

$$[Gd]_{T_1} \propto \Delta S_1(t) = S_1(t) - S_{10} \qquad [4.1]$$

The change in T_1 relaxation rate (ΔR_1) has a more accurate correlation with Gd concentration, but because the TR used here is relatively short, a first order approximation was used to simplify model fitting and avoid additional error propagation from calculating ΔR_1 (3,4). There is a proton density (ρ_0) weighting in ΔS_1 as well, but because ρ_0 weighted images do not have much contrast in the brain, it was assumed to be negligible (4). For T_2^* data, ΔR_2^* curves were calculated for each voxel using signal intensity (S_2^*) and echo time (TE)

$$[Gd]_{T_2^*} \propto \Delta R_2^*(t) = \frac{-\ln\left(S_2^*(t)/S_{20}^*\right)}{TE}, \qquad [4.2]$$

where $S_2^*{}_0$ represents the pre-injection signal.

A model describing Gd concentration changes over time was fit to data in each voxel of the images corresponding to Gd concentration (Equations 4.1 and 4.2) using nonlinear least squares regression. T_1 weighted analyses used an automated technique to select voxels representing intravascular space and estimate intravascular model parameters (5). The intravascular model was then used as a vascular input function for

the rest of the voxels in a tissue exchange model. The T_2^* weighted analyses used the same tissue exchange model; however, an intravascular input function was not estimated. A general model for the two compartment exchange used here is described by the following equation:

$$C_V(t) = C_B(t) + k_{trans}\int_0^t C_B(\tau)^{-k_{ep}(t-\tau)}d\tau\ , \qquad [4.3]$$

where C_V represents Gd concentration in each voxel, C_B represents the Gd concentration from just the blood in each voxel, k_{trans} represents the transfer constant from blood to extravascular space, and k_{ep} represents the rate constant of Gd leaving extravascular space. In both model fitting techniques used here, k_{ep} is assumed to be negligible, and is omitted from the model fitting equation (6).

For the modeling of T_1 weighted data, a vascular input function was used, allowing estimated parameters to be normalized to what is perceived as whole blood kinetics. The model used for the vascular input function is:

$$C_B^{'}(t) = \begin{cases} 0 & t < t_{inj} \\ \dfrac{rate}{k_b}\left(1 - e^{-k_b(t-t_{inj})}\right) & t_{inj} \le t < t_{end} \\ C_B^{'}(t_{end})e^{-k_b(t-t_{end})} & t \ge t_{end} \end{cases}, \qquad [4.4]$$

where $C_B^{'}$ is constant for all voxels. The estimated parameters are t_{inj}, or time of injection (sec), *rate*, or injection rate (a.u. sec^{-1}) and k_b, or blood signal decay constant (sec^{-1}). The injection duration is known, thus t_{end} is simply the sum of t_{inj} and the injection duration.

Using a vascular input function slightly alters Equation 4.3, adding a fractional blood volume (f_{BV}) term.

$$C_{T_1}(t) = f_{BV}C_B^{'}(t) + k_{trans}\int_0^t f_{BV}C_B^{'}(\tau)d\tau \qquad [4.5]$$

f_{BV} (%) is simply the relative contribution from the vascular input function, or whole blood, to the signal in each voxel. Equation 4.3 is then further altered, as the product of k_{trans} and f_{BV} is used to estimate the endothelial leak rate in each voxel, or K^{PS} (mL blood sec^{-1} $100cc^{-1}$ tissue) from the T_1 weighted data.

$$C_{T_1}(t) = f_{BV} C_B{}'(t) + K^{PS} \int_0^t C_B{}'(\tau) d\tau \qquad [4.6]$$

Although an input function was not used for the T_2^* data fitting, the high temporal resolution necessitates the use of a model to describe the first pass Gd kinetics in the blood. A gamma-variate model was used to describe the contribution from the first pass of blood in each voxel (C_{BGV}).

$$C_{BGV}(t) = CBV \frac{(t - t_0)^{\alpha} e^{-(t - t_{inj})/\beta}}{\beta^{\alpha+1} \Gamma(\alpha + 1)} \qquad [4.7]$$

where CBV (a.u.) represents cerebral blood volume. The gamma-variate model has been commonly used to describe the first pass kinetics of a bolus injection (7,8,9). For T_2^* data, Equation 4.3 now becomes:

$$C_{T_2^*}(t) = C_{BGV}(t) + k_{T2*} \int_0^t C_{BGV}(\tau) d\tau \qquad [4.8]$$

where k_{T2*} (sec^{-1}) is just k_{trans} estimated for the T_2^* data. The T_2^* DCE-MRI fitting algorithm was previously described by Lee et al. (10). It is important to note that because there is no vascular input function in Equation 4.8, an estimate for the relative amount of blood in a voxel can only be derived by comparing CBV values between voxels. Therefore, CBV normalized to NAWM ($nCBV$) was used to compare CBV values between patients.

4.3.3 Comparative Analysis

Using statistical tests, the estimated parameters representing tissue vascularity (f_{BV} and $nCBV$) and vascular permeability (K^{PS} and k_{T2*}) were directly compared across glioma patients to assess how well the parametric maps represented the disease state as determined by the histologic tumor grade. A Kruskal-Wallis statistical comparison was performed to assess if a significant difference existed between each parameter grouped by tumor grade. The Spearman rank correlation coefficient was also calculated for each parameter to test for a significant correlation with histologic grade. Additionally, the relative difference between tumor and NAWM was compared to assess the "malignancy contrast ratio" (MCR) for each parameter ($MCR_{PAR} = PAR_{CEL}:PAR_{NAWM}$). For the grade 4 glioma patients, a Friedman statistical test was used to assess any significant differences in the MCR values between the parameters. This was followed by a Student-Newman-Keuls multiple comparison to test which pairs of parameters showed a significant difference ($p<0.05$). Tissue vascularity parameters were tested for validity by comparing ratios of NAGM and NAWM to published cerebral blood volume ratios (11,12,13) in all twenty two patients. f_{BV} values were also compared to literature values for NAWM and NAGM because they were considered absolute values.

4.4 Results

Figure 4.3 shows representative parametric images from patients with grade 2, grade 3, and grade 4 gliomas, with median parameter values in the table below each patient's images. The CEL is labeled on the post-Gd T_1 weighted 3D-FSPGR on the left. A maximum intensity projection (MIP) of f_{BV} is also shown on the far right for each patient. The f_{BV} MIP demonstrates the superior image quality available with the T_1

weighted DCE-MRI techniques, as blood vessels are clearly visible. Additionally, T_2^* weighted images showed a varying amount of geometric distortion artifacts due to the EPI technique, which made coregistration between images difficult. This was not observed in the T_1 weighted images.

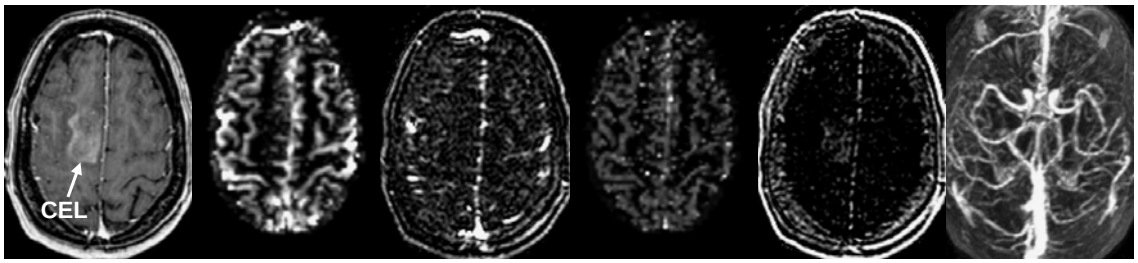

		CBV	f_{BV}	k_{T2*}	K^{PS}
Grade 2	CEL	767.68 ± 821.75	3.70% ± 2.02%	0.019 ± 0.016	0.015 ± 0.009
	NAWM	319.23 ± 339.52	2.25% ± 1.54%	0.008 ± 0.008	0.004 ± 0.004
	NAGM	1744.6 ± 977.86	4.63% ± 2.63%	0.018 ± 0.008	0.005 ± 0.005

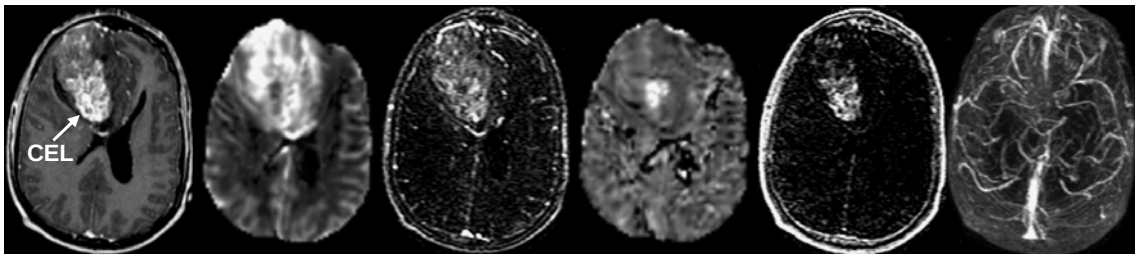

		CBV	f_{BV}	k_{T2*}	K^{PS}
Grade 3	CEL	4416.4 ± 1198.4	13.09% ± 5.31%	0.056 ± 0.023	0.045 ± 0.022
	NAWM	964.6 ± 291.1	2.28% ± 1.53%	0.037 ± 0.011	0.005 ± 0.004
	NAGM	2048.0 ± 533.0	3.33% ± 2.02%	0.034 ± 0.009	0.008 ± 0.006

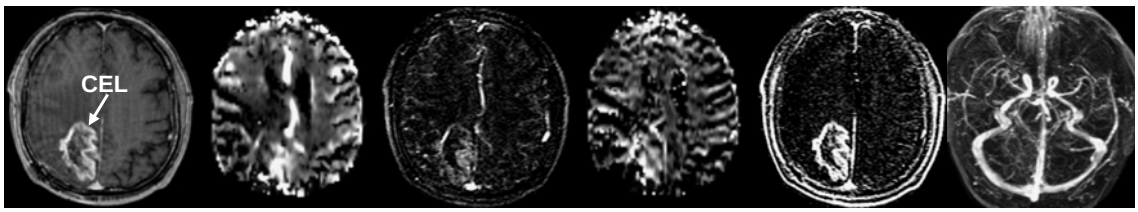

		CBV	f_{BV}	k_{T2*}	K^{PS}
Grade 4	CEL	2405.3 ± 1565.3	8.85% ± 5.76%	0.045 ± 0.033	0.105 ± 0.055
	NAWM	2061.2 ± 918.6	1.99% ± 1.34%	0.030 ± 0.020	0.011 ± 0.007
	NAGM	2181.8 ± 1355.2	3.75% ± 2.74%	0.022 ± 0.019	0.013 ± 0.009

Figure 4.3. Images from three glioma patients representing grade 2, 3, and 4 gliomas. From left to right the images are: T_1 weighted post-Gd 3D-FSPGR, *CBV* map, f_{BV} map (0-25%), k_{T2*} map (0-0.1 sec^{-1}), K^{PS} map (0-0.075 mL blood sec^{-1} $100cc^{-1}$ tissue), and maximum intensity projection (MIP) of f_{BV} (0-75%). Median parameter values (±SD) within each patient are listed for the CEL, NAWM, and NAGM ROIs.

Table 4.1 shows median parameter values (±SD) for each enhancing glioma patient. Error propagation was used to calculate SD values for *nCBV*. The median values within each grade are also shown, including the standard deviation of the medians (SE). Malignancy contrast ratios (MCR_{PAR}) for each parameter are also shown. The MCR is defined as the ratio of parameter values between CEL and NAWM ($MCR_{PAR} = PAR_{CEL}:PAR_{NAWM}$). For the grade 4 glioma patients, there existed a significant difference in the MCR values between parameters ($p=0.0001$) when assessed using the Friedman test. Three pairs of parameters showed a significant difference ($p<0.05$) when compared using the Student-Newman-Keuls multiple comparison test: MCR_{CBV} was significantly different than MCR_{KPS} and MCR_{kT2*} was significantly different than both MCR_{fBV} and MCR_{KPS}.

There was no statistical significance found between tumor grades for any parameters when analyzed with the Kruskal-Wallis statistical test ($p>0.05$); however, there was nearly significance for K^{PS} ($p=0.086$) and k_{T2*} ($p=0.100$). When the parameter values were tested for a correlation with tumor grade using a Spearman rank correlation coefficient, both K^{PS} and k_{T2*} showed a significant relationship ($p<0.05$). Figure 4.4 shows the parameter values grouped by tumor grade in boxplots.

Table 4.1. Median (±SD) DCE-MRI parameter values for each glioma patient in the CEL. Malignancy contrast ratio (MCR_{PAR}) for each parameter is also included. The patients are divided by WHO grade and the median parameter values and SD are shown above the standard deviation of the median (SE) for each grade.

Grade	T2* Weighted Parameters				T1 Weighted Parameters			
	nCBV	MCR_{CBV} †	k_{T2*}	MCR_{kT2*} §♦	f_{BV}	MCR_{fBV} §	K^{PS}	MCR_{KPS} †♦
2	2.40 ± 3.63	2.40	0.019 ± 0.016	2.38	3.70% ± 2.02%	1.65	0.015 ± 0.009	3.56
2	4.93 ± 2.95	4.93	0.026 ± 0.014	1.17	12.06% ± 6.98%	7.20	0.024 ± 0.024	3.65
Median±SD	**3.67 ± 3.29**	**3.67**	**0.022 ± 0.015**	**1.78**	**7.88% ± 4.50%**	**4.42**	**0.020 ± 0.017**	**3.61**
SE	**1.79**	**1.79**	**0.005**	**0.85**	**5.91%**	**3.92**	**0.006**	**0.06**
3	**4.58 ± 1.86**	**4.58**	**0.056 ± 0.023**	**1.50**	**13.09% ± 5.31%**	**5.74**	**0.045 ± 0.022**	**8.88**
4	3.73 ± 2.76	3.73	0.065 ± 0.031	2.20	19.75% ± 11.28%	8.08	0.092 ± 0.045	10.82
4	3.50 ± 2.41	3.50	0.078 ± 0.023	2.17	10.14% ± 5.47%	5.00	0.043 ± 0.025	7.22
4	2.44 ± 1.39	2.44	0.066 ± 0.010	0.78	11.10% ± 6.10%	8.00	0.055 ± 0.021	10.23
4	2.36 ± 2.86	2.36	0.027 ± 0.020	1.73	11.61% ± 5.80%	3.20	0.037 ± 0.022	4.72
4	2.59 ± 1.99	2.59	0.068 ± 0.020	3.80	13.94% ± 5.55%	5.88	0.098 ± 0.032	10.54
4	4.98 ± 4.78	4.98	0.077 ± 0.050	4.11	16.82% ± 6.30%	6.32	0.059 ± 0.037	6.16
4‡	1.17 ± 0.92	1.17	0.045 ± 0.033	1.48	8.85% ± 5.76%	4.44	0.105 ± 0.055	9.75
4‡	1.36 ± 1.23	1.36	0.034 ± 0.025	1.48	5.76% ± 3.68%	3.52	0.049 ± 0.025	8.67
Median±SD	**2.52 ± 2.20**	**2.52**	**0.066 ± 0.024**	**1.95**	**11.36% ± 5.78%**	**5.44**	**0.057 ± 0.029**	**9.21**
SE	**1.26**	**1.26**	**0.020**	**1.16**	**4.47%**	**1.86**	**0.027**	**2.25**

‡ – indicates patients with a recurrent tumor, all others were newly diagnosed.
† – indicates a significant difference was found between MCR_{CBV} and MCR_{KPS}.
§ – indicates a significant difference was found between MCR_{kT2*} and MCR_{fBV}.
♦ – indicates a significant difference was found between MCR_{kT2*} and MCR_{KPS}.

Although not all patients in this study were diagnosed with a glioma, all did receive DCE-MRI scans and had parametric maps calculated. Thus, all patients' parameter values were able to be assessed in NAGM and NAWM. Table 4.2 shows median values for f_{BV} in NAGM and NAWM along with there ratios (NAGM:NAWM). Only the NAGM:NAWM ratio is shown for *CBV* because the values were not absolute. The standard deviation for each patient is also listed (the SD for NAGM:NAWM was estimated using error propagation). The median of all patients' f_{BV} values in NAWM and NAGM and the NAGM:NAWM ratios from both f_{BV} and *CBV* agreed with values from literature (11,12,13).

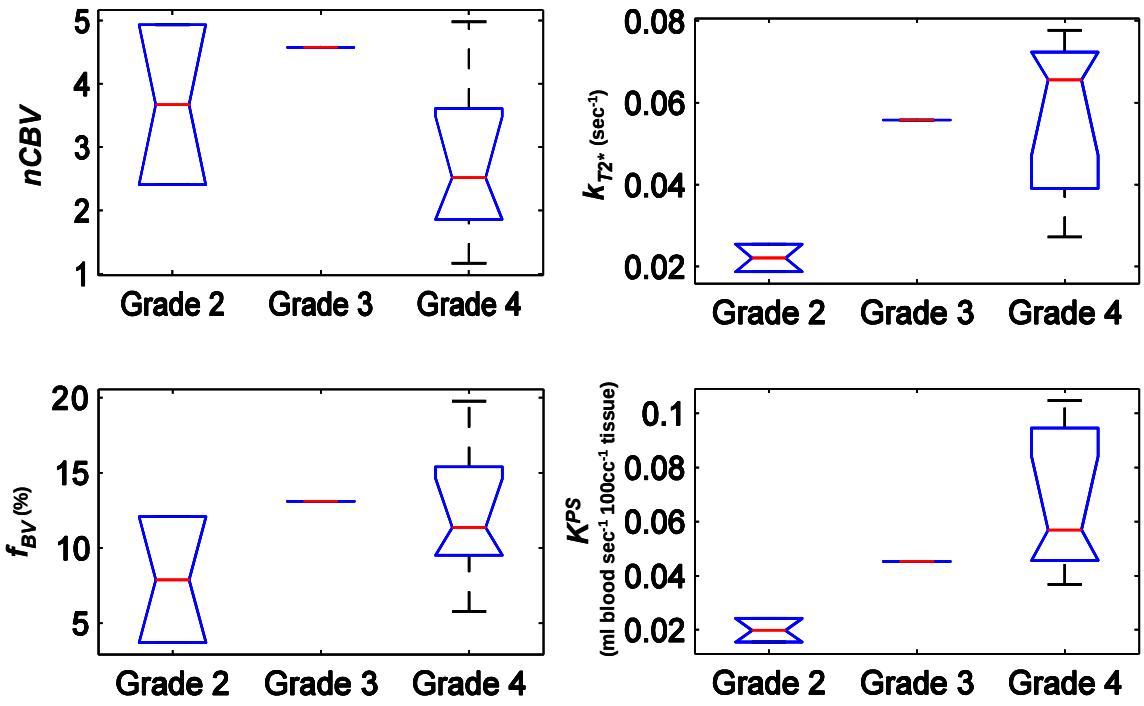

Figure 4.4. Boxplots of parameter values vs grade. There were no significant differences ($p<0.05$) in parameter values between grades using a Kruskal-Wallis test (*nCBV*: p=0.526, k_{T2*}: p=0.100, f_{BV}: p=0.567, K^{PS}: p=0.086). However, with a Spearman rank correlation, both k_{T2*} and K^{PS} showed a significant ($p<0.05$) correlation with grade (k_{T2*}: r_s=.627, p=0.039; K^{PS}: r_s=0.679, p=0.022), while blood volume parameters showed no significant correlation (*nCBV*: r_s=-0.296, p=0.377; f_{BV}: r_s=0.174, p=0.609).

Table 4.2. Median blood volume parameters (±SD) for each patient as estimated from T_1 weighted DCE-MRI (f_{BV}) and T_2^* weighted DCE-MRI (CBV) in NAGM and NAWM, including median ratios of NAGM:NAWM. Only the ratio is shown for CBV because the values are not absolute. Overall median values (±median SD) and standard deviation of the medians (SE) are shown for the total patient group. NAGM:NAWM blood volume ratios are consistent with published values (11-13) for both T_1 weighted and T_2^* weighted parameters. T_1 weighted f_{BV} values show absolute values that are also consistent with literature.

Patient	T_1 (f_{BV})			T_2^* (CBV)
	NAGM	NAWM	NAGM:NAWM	NAGM:NAWM
1	4.63% ± 2.63%	2.25% ± 1.54%	2.06 ± 1.41	5.47 ± 6.57
2	3.28% ± 2.39%	1.68% ± 1.24%	1.96 ± 1.45	1.88 ± 1.21
3	3.33% ± 2.02%	2.28% ± 1.53%	1.46 ± 0.98	2.12 ± 0.85
4	5.16% ± 4.01%	2.45% ± 1.61%	2.11 ± 1.39	2.83 ± 2.13
5	3.60% ± 2.62%	2.03% ± 1.42%	1.78 ± 1.24	2.35 ± 2.05
6	2.26% ± 1.47%	1.39% ± 0.92%	1.63 ± 1.08	1.44 ± 0.72
7	8.70% ± 6.47%	3.63% ± 2.29%	2.39 ± 1.51	2.68 ± 2.86
8	2.82% ± 2.51%	2.37% ± 1.64%	1.19 ± 0.82	1.47 ± 1.52
9	5.30% ± 3.48%	2.66% ± 1.86%	1.99 ± 1.39	1.72 ± 1.84
10	3.75% ± 2.74%	1.99% ± 1.34%	1.88 ± 1.27	1.06 ± 0.81
11	3.01% ± 2.08%	1.64% ± 1.06%	1.84 ± 1.19	2.31 ± 1.23
12	3.56% ± 2.26%	1.85% ± 1.25%	1.93 ± 1.30	2.22 ± 1.92
13	3.97% ± 2.42%	2.58% ± 1.75%	1.54 ± 1.04	1.07 ± 0.61
14	5.61% ± 3.86%	2.30% ± 1.91%	2.44 ± 2.02	1.67 ± 1.05
15	5.56% ± 2.86%	2.54% ± 1.70%	2.19 ± 1.47	2.67 ± 5.73
16	5.61% ± 3.74%	2.26% ± 1.48%	2.48 ± 1.62	1.68 ± 1.28
17	4.44% ± 2.40%	2.58% ± 1.76%	1.72 ± 1.18	2.15 ± 1.42
18	2.92% ± 1.83%	1.40% ± 0.95%	2.09 ± 1.41	2.19 ± 2.05
19	3.56% ± 2.69%	2.39% ± 1.70%	1.49 ± 1.06	2.67 ± 1.89
20	5.10% ± 4.26%	2.74% ± 2.13%	1.86 ± 1.45	1.45 ± 1.68
21	5.29% ± 3.82%	2.49% ± 1.75%	2.13 ± 1.50	2.69 ± 2.80
22	5.17% ± 3.75%	2.95% ± 2.03%	1.75 ± 1.20	3.06 ± 4.87
Median	4.21% ± 2.66%	2.34% ± 1.63%	1.90 ± 1.35	2.17 ± 1.76
SE	1.42%	0.52%	0.33	0.92

Figure 4.5 shows comparative graphs of f_{BV} vs CBV (4.5a) and K^{PS} vs k_{T2*} (4.5b), normalized to parameter values in NAWM, in grade 4 patients only. All data points represent median ROI parameter values: blue squares represent NAGM and red circles represent CEL. The solid black line represents a perfect 1:1 correlation. There is not a strong correlation between parameters estimating blood volume ($R^2 = 0.33$) or between

parameters estimating endothelial leak rate ($R^2 = 0.27$). It is apparent that the parameters from T_1 weighted data show a larger contrast in tumor compared to NAWM than the T_2^* parameters. Additionally, the median NAGM:NAWM ratios show a larger variance in T_2^* parameters.

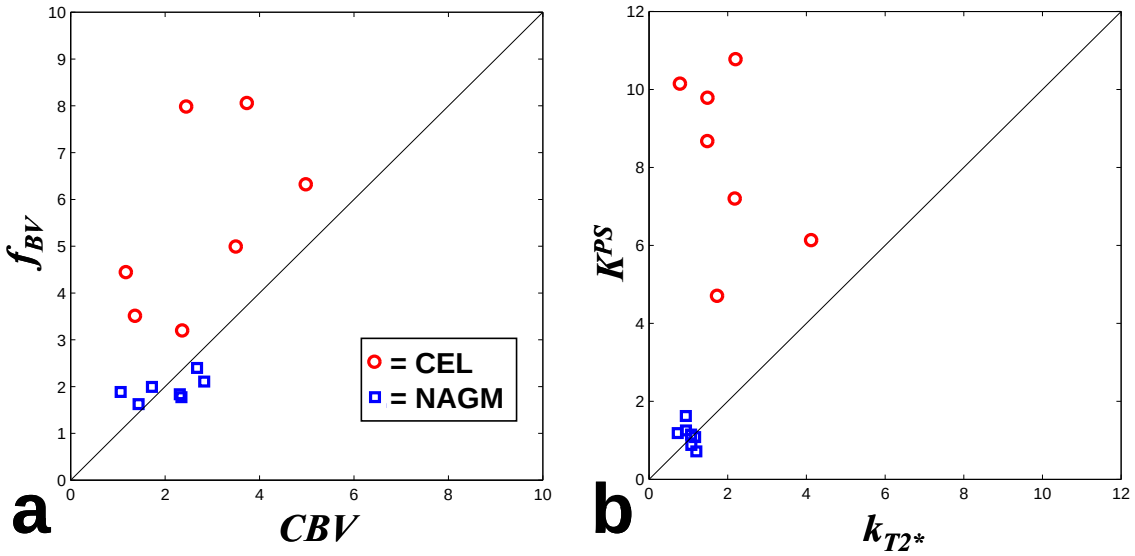

Figure 4.5. Comparison plots of blood volume parameters (a: f_{BV} vs CBV) and endothelial leak parameters (b: K^{PS} vs k_{T2*}). All parameter values are normalized to median values in NAWM. Blue squares represent median parameter values in NAGM and red circles represent median parameter values in CEL. The solid black line represents a perfect 1:1 correlation.

4.5 Discussion

This study demonstrates that both T_1 and T_2^* derived parametric maps can be useful in assessing glioma disease state. However, T_1 derived parameters may be more beneficial in patient diagnosis and prognosis due to significantly higher disease contrast, as assessed by malignancy contrast ratio (MCR). Although parametric maps of tumor blood volume (CBV and f_{BV}) may have shown a noticeable distinction between tumor and normal tissue, there was no significant relationship between these parameters and grade.

Parameters corresponding to tissue permeability (K^{PS} and k_{T2*}) did exhibit a significant correlation with tumor grade, but only showed a tendency for difference between grades. These results are in agreement with previous work done by Roberts, et al. (14). The conclusions based on the statistics performed here may change as the number of glioma patients receiving both acquisitions increases, especially in the lower grade groups. However, with the small number of patients in this study, it does appear that maps of K^{PS} show the largest distinction between normal and cancerous tissue and median CEL parameter values significantly correlate with tumor grade.

Absolute values of f_{BV} were consistent with literature values for NAGM and NAWM and both techniques blood volume ratios for NAGM:NAWM were also consistent. This supports the DCE-MRI modeling techniques used in this study and helps validate the other results. However, there are some issues associated with each modeling technique.

Most issues for modeling T_2^* weighted DCE-MRI data have to do with the acquisition parameters necessary to achieve T_2^* weighting. To reduce the influence of T_1 contrast, the TR must be relatively long (~1-2 seconds), but frequency encoding must be relatively quick with an EPI sequence because T_2^* decay is rapid and chemical shift and geometric distortion artifacts can become more pronounced the longer a frequency encoding gradient is on. This causes the T_2^* weighted data to have lower spatial coverage and resolution, but also allows for finer temporal resolution giving first pass kinetic information. Because the EPI sequence is more prone to geometric distortion artifacts from local susceptibility influences, image coregistration also becomes difficult. Inaccurate registration would create discrepancies in the volumes that the ROIs were

representing. Non-rigid image registration has been used to combat geometric distortion artifacts; however, it was not used in this study, and it may have slightly improved some of the MCR results for T_2^* derived parameters. Additionally, Gd has a strong effect on T_2^* that is felt by regions beyond its actual presence. This, coupled with the already lower spatial resolution, causes more volume averaging in the T_2^* dynamic data, which would reduce the ability to see finer tumor boundaries. However, the strong T_2^* effect of Gd also allows access to tissue with lower Gd concentrations than the T_1 weighted data, making the T_2^* data more sensitive to the presence of Gd. Because Gd also has an effect on T_1, T_2^* weighted images may be influenced by T_1 contrast in the presence of Gd. To account for this, the T_2^* weighted DCE-MRI was always acquired second, treating the first Gd injection as a loading dose. A loading dose has been shown to reduce T_1 influence on T_2^* weighted DCE-MRI data (15).

The T_1 weighted DCE-MRI modeling technique used here has a relatively poor temporal resolution (31 seconds). This is because of the fine spatial resolution and large coverage of the 3D-FSPGR acquisition. Temporal resolution can be improved, however, if spatial resolution and coverage and possibly SNR are compromised. The long duration between sequential images inhibits information about Gd first pass effects, and the data are thus assumed to be instantaneously well mixed. While this is not exactly true, the compartmental modeling technique used here assumes it is, thus data that are less influenced by first pass effects may actually be more appropriate for this modeling technique. More specifically, using a vascular input function can become problematic when there is a noticeable temporal difference between arterial and venous data. With a lower temporal resolution, this difference is masked, and the use of a vascular input

function may become more appropriate. Additionally, the slower Gd injection used in the T_1 weighted DCE-MRI acquisition is appropriate for the slower sampling time. Low sensitivity of T_1 weighted images to low Gd concentrations also inhibits parameter estimation in certain tissue. This is noticeable in Figure 4.3 as parametric images appear quite noisy in certain regions of the brain. However, as demonstrated by a lower relative standard error in NAGM:NAWM for f_{BV} compared to CBV (17% compared to 42%, respectively – see Table 4.2 and Figure 4.5), T_1 derived parameters may be more reproducible and vary less between patients than T_2^* derived parameters.

4.6 Conclusion

Both T_1 and T_2^* derived parametric maps are useful tools to help assess and monitor disease state. Values for blood volume parameters that are consistent with previously published values support the validity of both the modeling techniques used in this study. However, this study shows that T_1 derived parameters may be more beneficial than T_2^* derived parameters in assessing human gliomas. Specifically, tissue permeability as estimated via T_1 weighted DCE-MRI (K^{PS}) showed the largest contrast ratio for tumor compared to NAWM and had the strongest correlation with WHO tumor grade.

4.7 References

1. Rosen BR, Belliveau JW, Vevea JM, Brady TJ. Perfusion imaging with NMR contrast agents. Magn Reson Med 1990; 14: 249-265.
2. Daldrup H, Shames DM, Wendland M, Okuhata Y, Link TM, Rosenau W, Lu Y, Brasch RC. Correlation of dynamic contrast-enhanced magnetic resonance imaging with histologic tumor grade: comparison of macromolecular and small-molecular contrast media. Pediatr Radiol. 1998 Feb;28(2):67-78.
3. Shames DM, Kuwatsuru R, Vexler V, Mühler A, Brasch RC. Measurement of capillary permeability to macromolecules by dynamic magnetic resonance

imaging: a quantitative noninvasive technique. Magn Reson Med. 1993 May;29(5):616-22.
4. Walker-Samuel S, Leach MO, Collins DJ. Reference tissue quantification of DCE-MRI data without a contrast agent calibration. Phys Med Biol. 2007 Feb 7;52(3):589-601. Epub 2007 Jan 10.
5. Zierhut ML, Gardner JC, Spilker ME, Sharp JT, Vicini P. Kinetic modeling of contrast-enhanced MRI: an automated technique for assessing inflammation in the rheumatoid arthritis wrist. Ann Biomed Eng. 2007 May;35(5):781-95. Epub 2007 Mar 6.
6. Patlak CS, Blasberg RG, Fenstermacher JD. Graphical evaluation of blood-to-brain transfer constants from multiple-time uptake data. J Cereb Blood Flow Metab. 1983 Mar;3(1):1-7.
7. Davenport R. The derivation of the gamma-variate relationship for tracer dilution curves. J Nucl Med. 1983 Oct;24(10):945-8.
8. ThompsonHK Jr, Starmer CF, Whalen RE, McIntosh HD. Indicator Transit Time Considered as a Gamma Variate. Circ Res. 1964 Jun;14:502-15.
9. Benner T, Heiland S, Erb G, Forsting M, Sartor K. Accuracy of gamma-variate fits to concentration-time curves from dynamic susceptibility-contrast enhanced MRI: influence of time resolution, maximal signal drop and signal-to-noise. Magn Reson Imaging. 1997;15(3):307-17.
10. Lee MC, Cha S, Chang SM, Nelson SJ. Dynamic susceptibility contrast perfusion imaging of radiation effects in normal-appearing brain tissue: changes in the first-pass and recirculation phases. J Magn Reson Imaging. 2005 Jun;21(6):683-93.
11. Leenders KL, Perani D, Lammertsma AA, et al. Cerebral blood flow, blood volume and oxygen utilization. Normal values and effect of age. Brain 1990;113(Pt 1):27–47.
12. Hamberg LM, Hunter GJ, Kierstead D, Lo EH, Gilberto Gonzalez R, Wolf GL. Measurement of cerebral blood volume with subtraction three-dimensional functional CT. AJNR Am J Neuroradiol 1996;17:1861–1869.
13. Newman GC, Delucia-Deranja E, Tudorica A, Hospod FE, Patlak CS. Cerebral blood volume measurements by T*2-weighted MRI and contrast infusion. Magn Reson Med 2003;50:844–855.
14. Roberts HC, Roberts TP, Brasch RC, Dillon WP. Quantitative measurement of microvascular permeability in human brain tumors achieved using dynamic contrast-enhanced MR imaging: correlation with histologic grade.AJNR Am J Neuroradiol. 2000 May;21(5):891-9.
15. Boxerman JL, Schmainda KM, Weisskoff RM. Relative cerebral blood volume maps corrected for contrast agent extravasation significantly correlate with glioma tumor grade, whereas uncorrected maps do not. AJNR Am J Neuroradiol. 2006 Apr;27(4):859-67.

Chapter 5: ^{1}H Spectroscopic Imaging of Human Brain at 3T: Comparison of Fast 3D-MRSI Techniques

5.1 Abstract

Purpose: To investigate SNR and data quality of time-reduced ^{1}H 3D-MRSI techniques in the human brain.

Materials and Methods: Techniques investigated included ellipsoidal k-space sampling, parallel imaging, and EPSI. The SNR values for NAA, Cho, Cre, and lactate or lipid peaks were compared across techniques after correcting for effective spatial resolution and acquisition time in a phantom and in the brains of human volunteers. Other factors considered were linewidths, metabolite ratios, partial volume effects, and subcutaneous lipid contamination.

Results: In volunteers, the median normalized SNR for the SENSE data decreased by 37-41%, but could be significantly improved using regularization. The normalized signal to noise loss in flyback EPSI data was 19-23%. The effective spatial resolutions of the traditional, ellipsoidal, SENSE, and EPSI data were 1.02, 2.43, 1.03, and 1.01cm^{3}, respectively. As expected, lipid contamination was variable between subjects but was highest for the SENSE data. Patient data obtained using the flyback EPSI method were of excellent quality.

Conclusions: The data from all ^{1}H 3D-MRSI techniques were clinically acceptable, based upon SNR, linewidths, and metabolite ratios. The larger FOV obtained with the EPSI methods showed negligible lipid aliasing with acceptable SNR values in less than 9.5 minutes without compromising the PSF.

5.2 Introduction

Proton magnetic resonance spectroscopic imaging (^{1}H MRSI) has become a routine clinical imaging tool for non-invasively assessing the spatial distribution of different metabolites (1-3). This is of particular importance in the evaluation of neurological diseases. Many of the current studies that have applied point resolved (PRESS) 3D-MRSI are being performed at 1.5 Tesla (T) with a standard quadrature head coil and nominal spatial resolution of 1cm^3 with acquisition times of 20 minutes or greater (4,5). The time required to obtain these data may limit the options for acquiring other valuable imaging sequences during a single patient visit.

By using a 3T scanner with an eight-channel phased array reception coil, it is possible to improve the signal to noise ratio (SNR) of the data by two-fold (6) without compromising the contrast between metabolite levels in normal appearing white matter (NAWM) and tumor (7). This increase can either be used to maintain the spatial resolution and shorten the acquisition time or to improve the spatial resolution of the data with a similar acquisition time. The traditional method for localizing the signal relies on multiple phase encoding steps to gather the necessary spatial information. The time required to obtain these data for a given echo time (TE) depends linearly upon the repetition time (TR). Reducing the time needed to acquire the data requires the implementation of novel k-space sampling strategies (8-13).

Three well-known approaches that have been proposed to reduce the acquisition time for ^{1}H 3D-MRSI data are ellipsoidal k-space encoding (9), parallel imaging reconstruction (10), and time varying readout gradient trajectories such as spiral spectroscopic imaging (11) and echo-planar spectroscopic imaging (EPSI) (12).

Ellipsoidal k-space techniques are implemented by limiting the number of acquired phase encoding steps to a central ellipsoid of k-space, thus decreasing the number of samples obtained and reducing acquisition time. Parallel imaging techniques reduce the number of acquired k-space points by increasing the spacing between k-space samples. Additional spatial information from multiple receiver coils is then used to increase the spatial field-of-view (FOV) to the original size. EPSI and spiral SI techniques apply a time varying gradient waveform during data acquisition to simultaneously encode spectral and spatial information. This reduces the acquisition time by a factor determined by the number of phase encodes that would have been acquired in the EPSI or spiral dimensions. A variety of gradient trajectories may be considered based upon how they address waveform efficiency, robustness to gradient imperfections, and the tradeoff between spatial resolution and spectral bandwidth (13).

The purpose of this study was to investigate the relative benefits of time-reducing ^{1}H 3D-MRSI techniques, and to determine which technique reduced acquisition time with the lowest cost in SNR and data quality. These issues were first investigated using ^{1}H 3D-MRSI data from phantoms and healthy volunteers. Following this analysis, the most promising technique was applied to seventeen patients diagnosed with primary brain tumors in order to evaluate its robustness in a clinical setting.

5.3 Materials and Methods

Images and ^{1}H MRSI data were acquired using a 3T MR Scanner (GE Healthcare, Waukesha, WI) with an eight-channel phased array head coil. Data were acquired on four separate occasions from an MR phantom that contained water, choline (Cho), creatine (Cre), N-acetyl aspartate (NAA), and lactate (Lac). Comparison data were then acquired

from the brains of five healthy human volunteers. Seventeen clinical EPSI datasets were also acquired in patients with primary brain tumors. All human subjects provided informed consent as required by our institutional review board.

5.3.1 MR Data Acquisition Protocol

Data obtained from phantoms and healthy volunteers consisted of a scout sequence followed by an anatomic imaging sequence (axial T1-weighted 3D-IRSPGR: FOV=24x24x18cm^3, 256x256x120 voxels, 15° flip angle, TE=1.6ms, TI=400ms, TR=7.3ms); a set of 2D fast GRE proton density weighted coil sensitivity images (FOV=30x30x18cm^3, 64x64x36 voxels, 20° flip angle, TE=2.1ms, TR=150ms); and 4 different ^{1}H 3D-MRSI acquisitions. The ^{1}H MRSI sequences applied PRESS volume localization with an 8cm x 8cm x 4cm selection from the center of the phantom or brain, with chemical shift selective (CHESS) (14) pulses for water suppression, and very selective suppression (VSS) (15) pulses to limit the degree of lipid contamination from the scalp.

The acquisition parameters for the ^{1}H 3D-MRSI data are summarized in Table 5.1 and the two EPSI trajectories are shown in Figure 5.1. In all cases the echo-planar encoding was performed in the superior-inferior (SI) dimension. Ellipsoidal k-space sampling and parallel imaging data with a reduction factor of 2 in the RL dimension (R_x=2) were simulated from the fully encoded MRSI data by eliminating the appropriate phase encoded k-space points. In one of the five volunteers, flyback EPSI data were not acquired, and in a different volunteer, symmetric EPSI data were not acquired. The MRSI data from patients were acquired using EPSI with the flyback gradient as described in Table 5.1.

Table 5.1. List of all spectroscopic imaging techniques and their specifications, including: spatial field of view (FOV), spectral bandwidth (BW), number of scan repetitions (NEX), total acquisition time (t_{ACQ}), nominal resolution, and effective spatial resolution (as estimated via 3D-PSF simulation in MATLAB). The full-volume at half maximum PSF signal was used to represent effective spatial resolution. For traditional encoded 12x12x8 k-space sampling, ellipsoidal sampling, and SENSE sampling each point represented 9.04×10^{-6} cm^3 (1 $cm^3 = 48^3$ points). For all other 3D-MRSI techniques, each point represented 30.52×10^{-6} cm^3 (1 $cm^3 = 32^3$ points).

Encoding Technique	FOV (cm^3)	BW (Hz)	NEX	t_{ACQ} (min)	Nominal Resolution	Effective Spatial Resolution
Traditional MRSI	12x12x8	2000	1	21.12	1cm^3x1.95Hz	1.017 cm^3
Ellipsoidal MRSI *	12x12x8	2000	1	9.39	1cm^3x1.95Hz	2.473 cm^3
SENSE MRSI (R_x=2) *	12x12x8	2000	1	10.56	1cm^3x1.95Hz	1.026 cm^3
SENSE w/REG *	12x12x8	2000	1	10.56	1cm^3x1.95Hz	1.026 cm^3
Flyback EPSI	16x16x16	988	2	9.46	1cm^3x1.39Hz	1.014 cm^3
Symmetric EPSI	16x16x12	977	2	9.39	1cm^3x1.91Hz	1.015 cm^3
Symmetric w/ramps ‡	16x16x12	977	2	9.39	0.857cm^3x1.91Hz	0.868 cm^3

* These data sets were simulated from the traditionally encoded MRSI data.
‡ From same dataset as symmetric EPSI data.

5.3.2 Data Reconstruction

The traditionally encoded ^{1}H 3D-MRSI data were reconstructed by processing each of the 8 coil channels separately, apodizing with a 4Hz Lorentzian, applying phase and frequency corrections, and then removing residual water and baseline (6,16). The corrected spectroscopic images from each coil were then combined using coil sensitivity weighting from the low resolution proton density weighted images (17).

Ellipsoidal k-space sampling was simulated from the traditionally encoded MRSI data by reducing the number of phase encoding steps from 1152 (12x12x8) to 512 through zero filling the appropriate k-space points outside a normalized ellipsoidal radius of 1.2. This reduction would have resulted in an acquisition time of 9.39 minutes instead of the full 21.12 minutes. Data were then reconstructed in the same manner as the

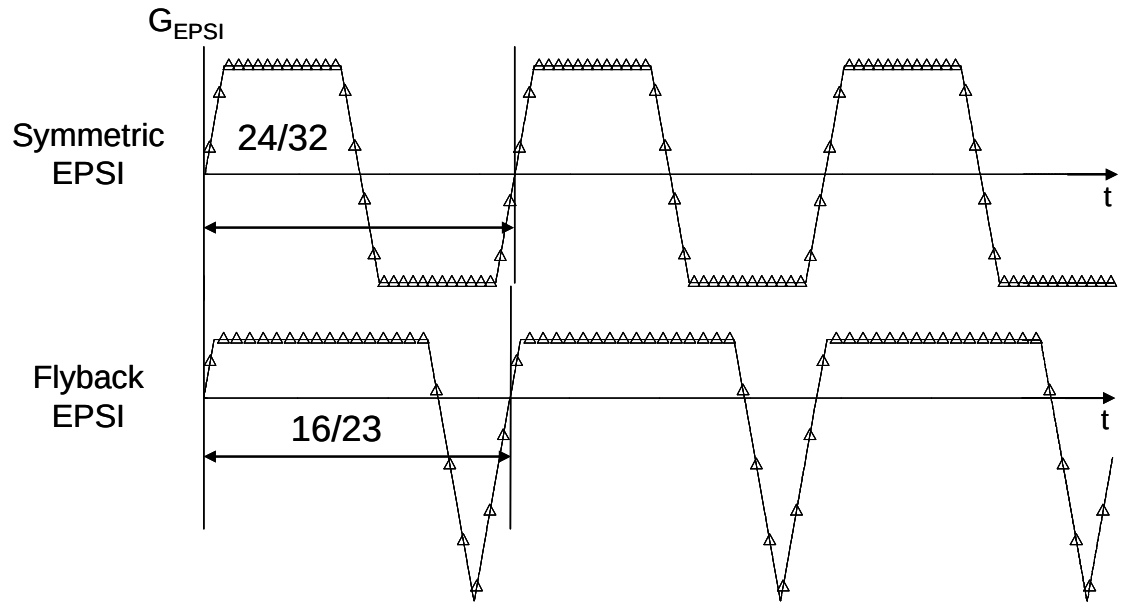

Figure 5.1. Gradient waveforms used for two different echo-planar spectroscopic imaging (EPSI) encoding techniques. Fractions represent the number of samples on the plateau compared to the total number of samples per echo for each technique. Double-sided arrows represent the relative duration of each gradient echo.

traditionally encoded data.

Parallel imaging data were simulated from the traditional fully encoded MRSI data using a SENSE data sampling scheme with a reduction factor of 2 along k_x (R_x=2), which would have corresponded to an acquisition time of 10.56 minutes. This resulted in a 6x12x8 simulated spectral data acquisition matrix. The parallel imaging data were reconstructed using the SENSE algorithm according to the following formula (10,18,19):

$$v = (S^H \psi^{-1} S + \lambda \mathrm{I})^{-1} S^H \psi^{-1} A, \qquad [5.1]$$

where S is the coil sensitivity matrix, ^{H} is the complex conjugate transpose, ψ is the receiver noise matrix (19), λ is the regularization parameter, I is the identity matrix, A is the aliased spectrum, and v are the unaliased spectra. Tikhonov's regularization parameter, λ, was set to 1 for regularized and to 0 for unregularized SENSE reconstruction for this simulation.

The EPSI data were reconstructed one channel at a time and combined in the same way as the traditionally encoded data, but with the application of an additional linear phase correction in the EPSI dimension of spectral k-space to prevent spatial chemical shift artifacts (20). For the initial analysis, only samples from the flat part (plateau) of the EPSI gradient waveforms were used. To reconstruct the data acquired with the symmetric EPSI waveform, the positive and negative gradient lobe data were completely processed separately and then combined in the spectral image domain. In an additional technique, samples from the symmetric EPSI waveform transitions (ramps) were incorporated to reconstruct the data at a nominal resolution of 0.86cm^3 after applying a Gaussian-weighted average regridding algorithm (21).

5.3.3 Data Analysis

The spectroscopic imaging data were analyzed to quantify the SNR of the real peak heights of Cho, Cre, NAA, Lac (in phantom only), and lipid (Lip) (in volunteers only). For the lipid peak, which was not always in phase, peak heights were assessed as the maximum positive or minimum negative peak height. The noise was calculated, using all voxels in the PRESS box, as the minimum standard deviation of all continuous 20Hz segments within a 250Hz region without metabolite signal. Metabolite SNR values were then normalized to acquisition time (t_{ACQ}) and effective spatial resolution (*res*) as follows:

$$nSNR = \frac{SNR_{measured}}{res\sqrt{t_{ACQ}}} \qquad [5.2]$$

The effective spatial resolution was estimated using a simulation of the 3D point-spread function (PSF) in MATLAB (The Mathworks, Inc.) similarly to Maudsley et al. (9). By integrating the total number of voxels greater than 50% of the maximum signal in the 3D-

PSF, the full-volume at half maximum (FVHM) could be estimated to represent effective spatial resolution. In this simulation, for traditionally encoded 12x12x8 k-space sampling, ellipsoidal k-space sampling, and SENSE k-space sampling, 110592 (48^3) voxels represented 1 cm^3 (1 voxel = $9.04x10^{-6}$ cm^3); however, the larger FOV EPSI techniques used 32768 (32^3) voxels per 1 cm^3 (1 voxel = $30.52x10^{-6}$ cm^3) due to computer memory limitations for the simulation. The estimated effective spatial resolution for each technique as calculated from the FVHM of the 3D-PSF simulation is shown in the far right column of Table 5.1.

For phantom data, all voxels within the prescribed PRESS box were analyzed to compare nSNR of Cho, Cre, NAA, and Lac. Median nSNR values for each metabolite were compared along with the standard deviation of these medians for each acquisition. The median percent coefficient of variation (%CV) within the PRESS box was also compared across all techniques to assess the spatial variance in metabolites. The linewidth of NAA was analyzed similarly by looking at the median values, the standard deviation of the medians, and the median %CV within each acquisition.

For the volunteer data, the T1-weighted 3D-IRSPGR images were automatically segmented into partial volumes of NAWM, normal appearing gray matter (NAGM), and cerebral spinal fluid (CSF) (22,23). Normalized SNR values for Cho, Cre, and NAA, and NAA linewidths were compared across all techniques in the five volunteers (as described in phantoms) only in voxels within the press box that contained at least 90% NAWM. Cho:NAA ratios were assessed in all voxels containing at least 90% NAWM and a Wilcoxon signed rank test and Spearman rank correlation were used to compare with the traditionally encoded MRSI ratios. The number of voxels that were at least 90% outside

the CSF and contained detectable metabolite peaks were also counted to determine the spectral quality across all ^{1}H 3D-MRSI methods. Cho, Cre, and NAA Peaks were considered detectable if they had a raw SNR value greater than 5. Lipid peaks were considered detectable if they had a peak height greater than 25% of the median NAWM NAA peak. Voxels in the volunteers that contained a detectable lipid peak were considered to have lipid contamination because the PRESS box was prescribed completely within the brain parenchyma. Partial volume effects were also qualitatively examined by looking at the voxels near the edge of the ventricles in the normal volunteers.

5.4 Results

Median nSNR values for NAA and Lac (±SD) in all phantom MRSI acquisitions are shown in Table 5.2, including median raw SNR values. The medians of the variation within each scan are also shown as a coefficient of variation (%CV). The nSNR values for the ellipsoidal data were corrected by a spatial resolution factor of 2.43 to account for the increased effective voxel size due to the PSF associated with the ellipsoidal sampling (9,23). It is well known that SENSE data reconstruction results in a noise amplification, which is assessed using the g-factor, and can be calculated on a voxel by voxel basis. The SNR values were not corrected for the g-factor, but it was estimated that the median phantom nSNR dropped by approximately 31-39% for NAA, Cho, Cre, and Lac, which translates to a median g-factor between 1.45 and 1.63, for the unregularized SENSE data. The Tikhonov regularized SENSE data showed an nSNR reduction of 4-18%, and a lower median g-factor of 1.04-1.21 for all metabolites. In regridded symmetric EPSI data, the median raw SNR decreased by 3.5% compared to plateau-only symmetric EPSI data,

Table 5.2. Median raw SNR and normalized SNR (nSNR: cm^{-3} $min^{-1/2}$) values for all spectroscopic imaging techniques for NAA and Lac in a phantom (N=4 scans). Standard deviation between the 4 scans is shown (for nSNR only) as median ± SD and the median variation within each scan is also presented as %CV. The Lac:NAA median ratio is displayed in the far right column.

Encoding Technique	NAA raw SNR	NAA nSNR	Lac raw SNR	Lac nSNR	Lac:NAA
Traditional MRSI	190.75	40.83 ± 1.53 (9.10%)	43.43	9.30 ± 0.12 (15.20%)	0.23
Ellipsoidal MRSI	289.92	38.26 ± 1.23 (9.09%)	65.53	8.65 ± 0.21 (14.86%)	0.23
SENSE MRSI (R_x=2)	83.86	25.15 ± 0.77 (16.64%)	19.17	5.75 ± 0.23 (21.22%)	0.23
SENSE w/REG	115.18	34.54 ± 2.41 (14.45%)	22.81	6.84 ± 0.38 (24.06%)	0.20
Flyback EPSI	116.03	37.20 ± 0.29 (9.10%)	25.22	8.08 ± 0.17 (12.32%)	0.22
Symmetric EPSI	109.87	35.32 ± 1.48 (9.52%)	22.18	7.13 ± 0.53 (14.07%)	0.21
Symmetric w/ramps	105.36	39.64 ± 1.39 (7.46%)	20.95	7.88 ± 0.32 (14.12%)	0.20

but the expected decrease due to finer effective spatial resolution was approximately 14%. After correcting the raw SNR values for effective spatial resolution, the regridding algorithm showed a median improvement in nSNR of approximately 13% compared to plateau-only data.

Table 5.3 shows median raw SNR and median nSNR (±SD) of NAA from NAWM in five volunteers. One of the five volunteers did not receive a flyback EPSI scan and another did not receive a symmetric EPSI scan. Median Cho:NAA and Cre:NAA ratios are also shown, along with percentage of voxels containing aliased lipid. The plateau-only symmetric EPSI data showed a larger median nSNR loss (21-30%) than the flyback data (19-23%) for Cho, Cre, and NAA. Regridding the symmetric ramp data improved the median nSNR for NAA by approximately 8.6%, and for Cho and Cre by 4.9% each. The EPSI data had higher median nSNR values for all metabolites than unregularized parallel imaging data, which showed a median nSNR drop of approximately 37-41%. With regularization, the parallel imaging data showed a median improvement of 37-42% in nSNR for Cho, Cre, and NAA, making the nSNR similar to

Table 5.3. Median raw SNR and normalized SNR (nSNR: cm^{-3} $min^{-1/2}$) values for all spectroscopic imaging techniques for NAA in 5 volunteers. Standard deviation between the 5 scans is shown (for nSNR only) as median ± SD. Median metabolite ratios are also shown for each technique (Cho:NAA and Cre:NAA). Voxels were considered to have aliased lipid if Lip SNR was greater than 25% of median NAA SNR in NAWM. Flyback data were not acquired on one volunteer and symmetric data were not acquired on another.

Encoding Technique	NAA raw SNR	NAA nSNR	Cho:NAA	Cre:NAA	% of voxels with aliased lipid
Traditional MRSI	**49.28**	**10.55** ± 0.63	**0.53**	**0.40**	**0.00** ± 6.80
Ellipsoidal MRSI	**75.74**	**10.00** ± 0.48	**0.53**	**0.40**	**0.00** ± 10.05
SENSE MRSI (R_x=2)	**21.69**	**6.51** ± 0.92	**0.53**	**0.43**	**26.05** ± 31.00
SENSE w/REG	**27.44**	**8.23** ± 1.64	**0.53**	**0.43**	**14.29** ± 24.11
Flyback EPSI	**27.57**	**8.84** ± 0.79	**0.50**	**0.38**	**0.38** ± 1.10
Symmetric EPSI	**25.71**	**8.27** ± 0.88	**0.52**	**0.38**	**0.00** ± 0.00
Symmetric w/ramps	**23.94**	**9.01** ± 1.12	**0.51**	**0.38**	**1.70** ± 1.30

that of the EPSI data.

The linewidths for NAA appeared similar across techniques, with median values of 5.5-6.5 Hz in phantom data and 9.4-10.9 Hz in volunteer data. Fully encoded MRSI data showed a median NAA linewidth of 6.2 Hz in phantom and 10.1 Hz in volunteers. Table 5.4 shows median linewidths for NAA in all techniques in phantoms and volunteers.

The relative metabolite ratios of Cho:NAA were similar across all MRSI techniques for volunteers when using a Spearman rank correlation to compare with traditional encoded MRSI ($p<0.05$). In the parallel imaging data set, and in both the symmetric and flyback datasets, the Wilcoxon signed-rank test showed only one volunteer with a significant difference in Cho:NAA values when compared to fully encoded MRSI.

Table 5.4. NAA linewidths for all techniques in phantom and volunteers. Median values of the median linewidths are shown with standard deviation of the median linewidths as ±S.D. All voxels within the PRESS box were included for the phantom data, while only voxels containing at least 90% NAWM were used in the volunteer analysis.

Encoding Technique	Phantom (N=4) NAA Linewidth (Hz)	Volunteer (N=5) NAA Linewidth (Hz)
Traditional MRSI	6.2 ± 0.16	10.1 ± 0.16
Ellipsoidal MRSI	6.3 ± 0.23	10.8 ± 0.26
SENSE MRSI (R_x=2)	5.5 ± 0.21	9.4 ± 0.38
Flyback EPSI	5.9 ± 0.04	10.7 ± 0.41
Symmetric EPSI	6.5 ± 0.06	10.9 ± 0.27
Symmetric w/ramps	6.5 ± 0.08	10.9 ± 0.35

Analysis of spectral quality showed between 96% and 100% of all voxels outside the ventricles had detectable NAA peaks (SNR > 5). For Cho and Cre the range was 92-100% and 87-100%, respectively. Figure 5.2 shows a bar graph of the median percentages of all detectable metabolites with error bars of one standard deviation for all techniques. Lipid aliasing was more noticeable in the parallel imaging techniques, as the median±SD percentage of voxels with lipid peaks greater than 25% of the median NAWM NAA signal was 26.1±31% in the SENSE reconstructed data. With regularization, this number decreased to 14.3±24%. The EPSI acquisition techniques showed a much lower percentage of voxels with lipid aliasing (all volunteers less than 3% of voxels). One volunteer showed strong lipid contamination in the traditional (16% of voxels) and ellipsoidal encoding (22% of voxels) techniques. Figure 5.3 shows two examples of volunteer spectral quality for traditional encoding, SENSE encoding, and flyback EPSI encoding.

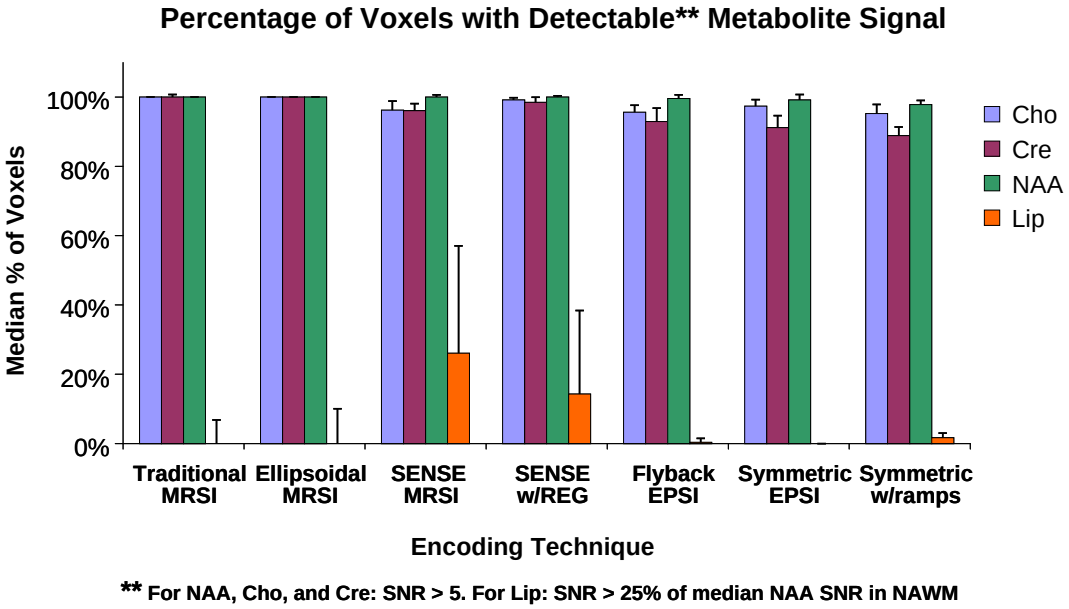

Figure 5.2. Median percentages of detectable voxels in each metabolite peak region are shown in the bar graph for each spectroscopic imaging technique. Error bars represent one standard deviation. Voxels were considered to have detectable NAA, Cho, and Cre signals if the metabolite raw SNR values were greater than 5. Voxels were considered to have aliased lipid if the lipid SNR was greater than 25% of the median SNR of NAA in NAWM.

Figure 5.4 provides a representative dataset from a volunteer to show how partial voluming varies between techniques. The ellipsoidal encoded MRSI data are clearly inferior to the other data, as the definition of the ventricle is visibly reduced. As expected, the other techniques appear to have similar edge definition to the traditionally encoded MRSI.

An example of data acquired on a glioma patient using a flyback EPSI sequence is shown in Figure 5.5. Differences in the pattern of metabolite levels were clearly visible in areas of T2 hyperintensity and contrast enhancement. Lipid, which is an important sign of necrosis, can be seen in multiple voxels in Figure 5.5. Based upon the analysis that we performed, these voxels should not have experienced aliasing from the scalp, and thus the

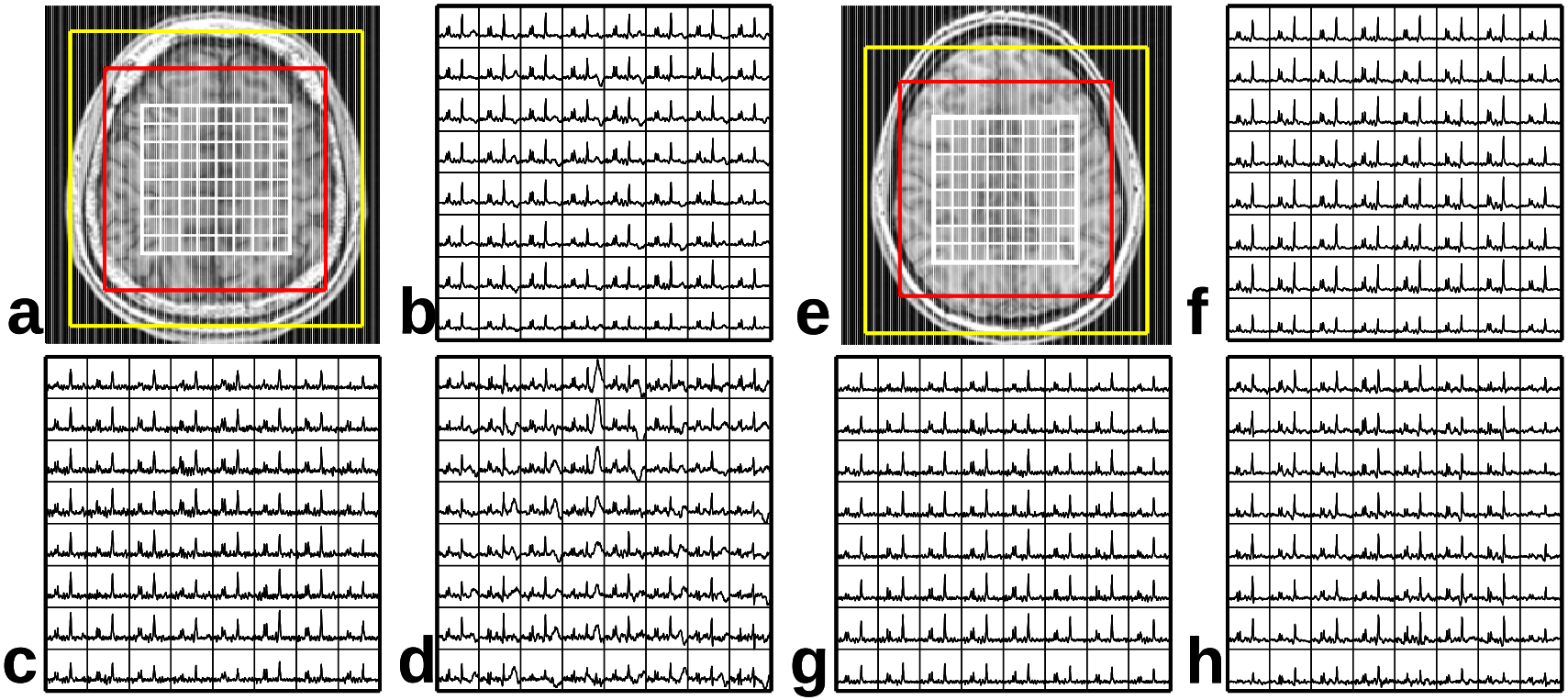

Figure 5.3. Representative datasets of two volunteers' spectra. T1 weighted images are shown (a and e) with the spectral grid overlaid in white. The red box represents the FOV of the traditional, ellipsoidal, and SENSE encoded data, while the yellow box represents the FOV of the EPSI encoded data. Spectra acquired with a traditional phase encoding technique (b and f), a flyback EPSI technique (c and g), and with the SENSE technique (d and h) are shown for one slice with a 1cm3 nominal resolution. Lipid contamination is noticeable in d and slightly apparent in b.

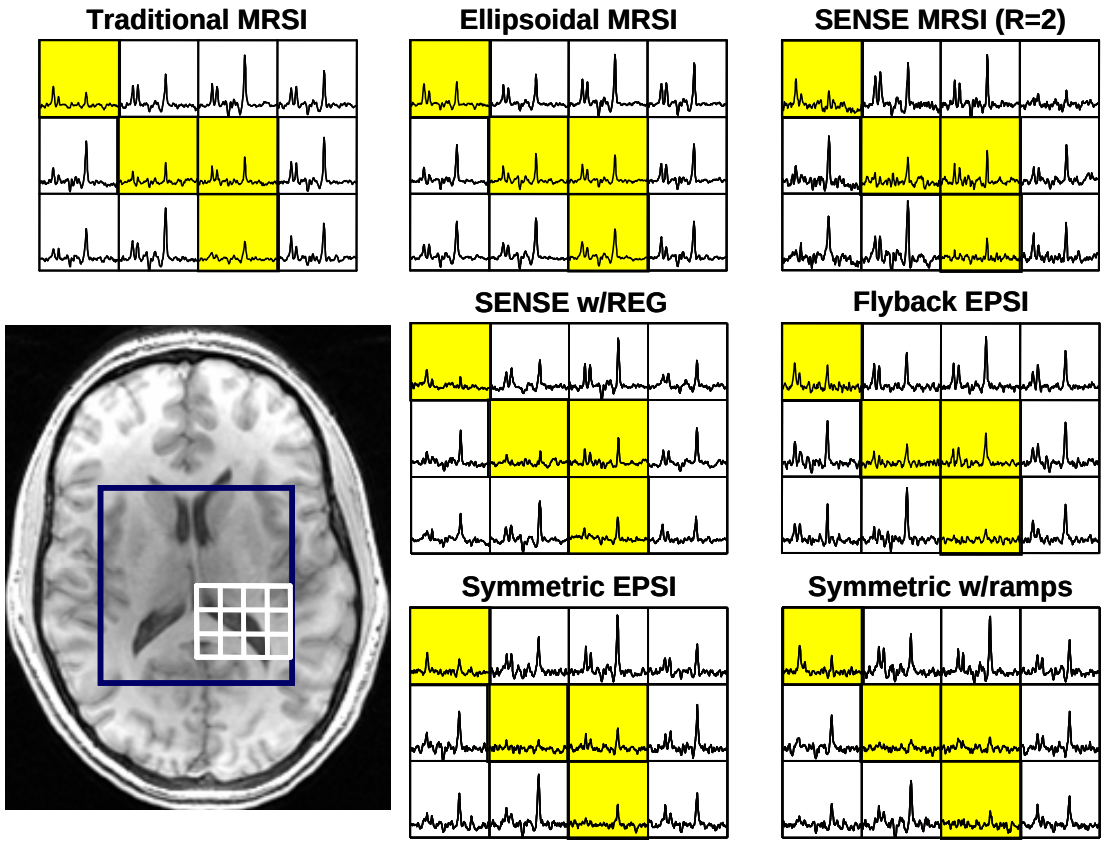

Figure 5.4. Qualitative examples of the partial volume effect in each spectroscopic imaging technique. Yellow boxes represent voxels containing ventricle.

lipid peaks may be attributed to there being necrosis in that region. The median raw SNR values in NAWM for the seventeen patients were 21.15±4.52, 11.76±3.59 and 8.86±2.33 for NAA, Cho, and Cre, respectively. The median Cho:NAA metabolite ratios in NAWM were similar to the values in NAWM from normal volunteers (not significantly different in a Mann-Whitney rank sum test ($p > 0.10$)). The median Cho:NAA ratio in the five healthy volunteers' NAWM was 0.53±0.04 for the traditionally encoded MRSI data, while the flyback data acquired in the seventeen patients had a median Cho:NAA ratio of 0.57±0.08 in NAWM. Lipid was detected within the tumors for 7 out of the 17 patient

scans using the flyback EPSI technique. No lipid was detected outside the T2 hyperintense lesions or contrast enhanced lesions in any of the 17 scans.

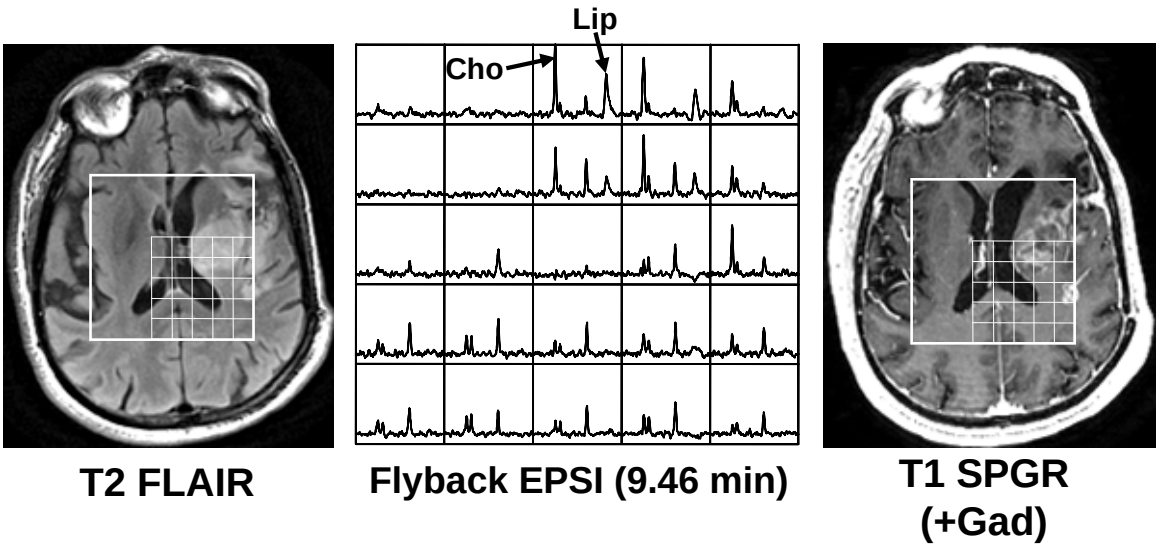

Figure 5.5. Typical data acquired on a glioma patient using a flyback EPSI sequence. High choline (Cho) and lipid (Lip) are markers of tumor pathology. Anatomical images (T2 FLAIR and T1 SPGR (+Gad)) are shown for reference.

5.5 Discussion

All of the fast spectroscopic imaging techniques examined in this study produced data that would have been relevant for clinical applications. Each had its own advantages and limitations, and the choice of which is most appropriate for any specific application needs to take these factors into account. The ellipsoidal encoded MRSI data provided the highest absolute SNR, but had a broader PSF causing a 2.43-fold increase in effective spatial resolution. This led to significant partial volume effects, which may not be important when looking at data with uniform concentrations of metabolites, but would make it extremely difficult to detect small lesions or heterogeneity in the case of tumors or other pathology. Showing a clear delineation between tumor and healthy tissue may be

a crucial factor for surgeons and oncologists who wish to define the spatial extent of the lesion.

Spectroscopic imaging with parallel reconstruction methods can dramatically reduce acquisition time, but SNR may be lost in the reconstruction algorithm due to the geometry of the coil array. Our results showed an nSNR loss in NAWM of volunteers of up to 41.3% in the unregularized data, which translated to a geometry factor (17) of approximately 1.7. After Tikhonov regularization was applied, the g-factor was reduced. For volunteers, a regularization factor of 1.0 showed a median improvement in SENSE encoded nSNR of approximately 37-42%, reducing the g-factor to approximately 1.2. Tikhonov regularization has been shown here as an important technique for increasing the SNR for parallel imaging by aiding in the matrix inversion. Despite the improved SNR from regularization, SENSE techniques are more prone to spectral contamination from spatial aliasing than the other fast MRSI techniques because of the reduced FOV used for data acquisition. Data quality will therefore be more dependent on the accuracy of coil calibration maps and the efficiency of VSS pulses in reducing the signal from subcutaneous lipid.

In this study, the traditionally and ellipsoidal encoded data may have suffered from a smaller FOV (as did SENSE data), but only one of the five volunteers showed large lipid contamination (16% in traditionally encoded data and 22% in ellipsoidal encoded data). No volunteers showed more than 3% contaminated voxels in any of the EPSI techniques. Four of the five volunteers showed lipid contamination in greater than 15% of the voxels in the SENSE encoded data. Additionally, the signal variation within each phantom scan was slightly higher for the SENSE reconstruction with and without

regularization, as seen in the larger %CV values in Table 5.2, compared to the other techniques. As the smaller FOV increases aliasing, the SENSE unfolding technique tries to correct for it; however, this correction is not always perfect. Perhaps this is why the relatively uniform metabolite signal in the phantom appears to vary slightly more in the SENSE reconstructed data. Another adverse effect may be seen in Figure 5.3, for the same reason. The spectra in Figures 5.3(b-d) show how a small lipid contamination in the traditionally encoded data (5.3b) can get magnified using the SENSE technique (5.3d). Note that data acquired from the same subject with the larger FOV used for EPSI acquisition show no noticeable lipid contamination.

Echo-planar spectroscopic imaging techniques can have the most significant effect on reducing acquisition time, but these techniques must trade off between spectral bandwidth and spatial resolution due to the limited gradient strength and slew rates available on a clinical system. To expand the spectral bandwidth, spectral data must be acquired faster, and unless the gradient strength can increase, faster spectral sampling will increase the spatial resolution in the EPSI dimension (improved spatial resolution will inhibit spectral bandwidth for the same reason). Gradient imperfections, asymmetries, inefficient sampling on the gradient waveform, and imperfect combination of data (symmetric EPSI data only) are also expected to provide a loss in nSNR for the EPSI techniques. These results show median nSNR losses in volunteers ranging from 16-21% for NAA for the EPSI techniques analyzed here compared to traditional phase encoded data.

Because of the more efficient spatial sampling, the FOV could be increased for the EPSI dimension at no cost until the maximum sampling frequency is reached. This is

important when trying to determine if tissue contains lipid or lactate, which are markers of necrosis and/or hypoxia (24-26). The high level of lipid in the human scalp makes lipid contamination a problem in brain spectroscopy, especially if the FOV is small. This contamination can thus hinder one's ability to assess real lipid or lactate, as lactate and lipid both resonate near 1-1.5 ppm in a ^{1}H spectrum. Additionally, k-space is fully sampled with these EPSI techniques, which results in less partial voluming than the ellipsoidal techniques, and thus maintains the ability to delineate important tissues from spectroscopic data (see Figure 5.4). Although the flyback EPSI waveform is slightly less efficient, the data quality appeared superior to the symmetric EPSI waveform data. This is most likely due to the imperfectly matched phases of the positive and negative gradient lobe data when they are combined. After applying a Gaussian-weighted average regridding algorithm to the more efficient symmetric EPSI data, the nSNR did improve; but because the effective spatial resolution was reduced to $0.87cm^3$, the raw SNR was still lower than the flyback EPSI data.

The quality of the MRSI data from the seventeen patient scans was comparable with that from the healthy volunteers. Cho:NAA ratios were not significantly different in NAWM, but the raw SNR was slightly lower. The lower SNR in patients may be attributed to the variable location of the press selected volume. In volunteers the selected volume was placed at the same location, which was relatively close to the eight coil elements. The prescription of the selected volume for the patients was based on tumor location, which is frequently lower in the head. This explains the slightly lower median SNR and the larger variation in values observed in patients. The flyback EPSI technique was also successful in identifying areas within the tumor containing lipid in 7 of the 17

scans in which it was used. This is important, as one can be confident that the lipid signal from the large FOV EPSI data is not coming from aliased subcutaneous fat signal. Using this technique may therefore provide data with more diagnostic value than methods utilizing acquisitions with lower FOV.

5.6 Conclusions

This study compares the performance of a number of fast three dimensional spectroscopic imaging techniques. Ellipsoidal k-space encoding, parallel imaging with and without Tikhonov regularization, and echo-planar techniques all produce spectroscopic images that are clinically acceptable. Each technique has strengths and weaknesses, and it is possible to incorporate multiple strategies into a single fast spectroscopic imaging sequence and reconstruction package (27). The EPSI techniques seem to pose a slight advantage over the other techniques due to the increased FOV (and less lipid aliasing) and preserved PSF. The flyback EPSI technique was shown to provide clinically reliable 3D-MRSI data in human glioma patients in less than 9.5 minutes.

5.7 Appendix: Gaussian-Weighted Average Regridding Algorithm

The 3D EPSI data contained data points that were acquired during gradient transitions. These data points were not used in normal reconstruction for any of the EPSI techniques. Incorporating these data points into the reconstruction could improve the results; but only if they could be reliably remapped, or regrid, to their appropriate k-space locations.

A Gaussian-weighted average regridding technique was applied only to the EPSI method with a symmetric gradient waveform. Points acquired during gradient transition

(or on the gradient ramps) were not correctly mapped when placed in their default k-space location. K-space locations from the trapezoidal gradient were compared to k-space locations from an ideal gradient (with no ramps). The differences between the locations were calculated and input into a Gaussian function with a full width at half maximum (FWHM) of $\sqrt{0.5}$ voxels^{-1}. Each value returned from this Gaussian function was then used as a weighting factor for the actual data when calculating the average value for each k-space location. If only one k-space value from the trapezoidal gradient was within one-half of a k-space voxel width to the ideal k-space location, the actual data was used for that location without any weighted average. Using the 8 data points acquired on the gradient ramps (for each echo) improved the waveform efficiency from 24 out of 32 data points used to 32 out of 32 data points used (75% efficiency to 100% efficiency), and also improved the spatial resolution by spanning an additional two k-space locations, going from 12 k-space voxels to 14 k-space voxels (17% improvement). The expected decrease in raw SNR due to this regridding technique is approximately 1.03%, or $1-\frac{\sqrt{32/24}}{14/12}$.

5.8 References

1. Bertolino A, Callicott JH, et al. Reproducibility of proton magnetic resonance spectroscopic imaging in patients with schizophrenia. Neuropsychopharmacology 18 (1998b), pp. 1-9.
2. Tedeschi G, Bonavita S, et al. Proton magnetic resonance spectroscopic imaging in the clinical evaluation of patients with Niemann-Pick type C disease. J Neurol Neurosurg Psychiatry. 1998 Jul;65(1):72-9.
3. Kurhanewicz J, Vigneron DB, Nelson SJ. Three-dimensional magnetic resonance spectroscopic imaging of brain and prostate cancer. Neoplasia. 2000 Jan-Apr;2(1-2):166-89. Review.

4. Govindaraju V, Gauger GE, Manley GT, Ebel A, Meeker M, Maudsley AA. Volumetric proton spectroscopic imaging of mild traumatic brain injury. AJNR Am J Neuroradiol. 2004 May;25(5):730-7.
5. Laprie A, Pirzkall A, et al. Longitudinal multivoxel MR spectroscopy study of pediatric diffuse brainstem gliomas treated with radiotherapy. Int J Radiat Oncol Biol Phys. 2005 May 1;62(1):20-31.
6. Li Y, Osorio JA, et al. Considerations in applying 3D PRESS H-1 brain MRSI with an eight-channel phased-array coil at 3 T. Magn Reson Imaging. 2006 Dec;24(10):1295-302. Epub 2006 Oct 18.
7. Osorio JA, Ozturk-Isik E, et al. 3D 1H MRSI of brain tumors at 3.0 Tesla using an eight-channel phased-array head coil. J Magn Reson Imaging. 2007 Jul;26(1):23-30.
8. Pohmann R, von Kienlin M, Haase A. Theoretical evaluation and comparison of fast chemical shift imaging methods. J Magn Reson. 1997 Dec;129(2):145-60.
9. Maudsley AA, Matson GB, Hugg JW, Weiner MW. Reduced phase encoding in spectroscopic imaging. Magn Reson Med. 1994 Jun;31(6):645-51.
10. Dydak U, Weiger M, Pruessmann KP, Meier D, Boesiger P. Sensitivity-encoded spectroscopic imaging. Magn Reson Med. 2001 Oct;46(4):713-22.
11. Adalsteinsson E, Irarrazabal P, Topp S, Meyer C, Macovski A, Spielman DM. Volumetric spectroscopic imaging with spiral-based k-space trajectories. Magn Reson Med. 1998 Jun;39(6):889-98.
12. Posse S, Tedeschi G, Risinger R, Ogg R, Le Bihan D. High speed 1H spectroscopic imaging in human brain by echo planar spatial-spectral encoding. Magn Reson Med. 1995 Jan;33(1):34-40.
13. Chen AP, Cunningham CH, et al. High-speed 3T MR spectroscopic imaging of prostate with flyback echo-planar encoding. J Magn Reson Imaging. 2007 Jun;25(6):1288-92.
14. Haase A, Frahm J, Hänicke W, Matthaei D. 1H NMR chemical shift selective (CHESS) imaging. Phys Med Biol. 1985 Apr;30(4):341-4.
15. Tran TK, Vigneron DB, et al. Very selective suppression pulses for clinical MRSI studies of brain and prostate cancer. Magn Reson Med. 2000 Jan;43(1):23-33.
16. Nelson SJ. Analysis of volume MRI and MR spectroscopic imaging data for the evaluation of patients with brain tumors. Magn Reson Med. 2001 Aug;46(2):228-39.
17. Pruessmann KP, Weiger M, Scheidegger MB, Boesiger P. SENSE: sensitivity encoding for fast MRI. Magn Reson Med. 1999 Nov;42(5):952-62.
18. Lin FH, Kwong KK, Belliveau JW, Wald LL. Parallel imaging reconstruction using automatic regularization. Magn Reson Med. 2004 Mar;51(3):559-67.
19. Ozturk-Isik E, Crane JC, Cha S, Chang SM, Berger MS, Nelson SJ. Unaliasing lipid contamination for MR spectroscopic imaging of gliomas at 3T using sensitivity encoding (SENSE). Magn Reson Med. 2006 May;55(5):1164-9.
20. Cunningham CH, Vigneron DB, Chen AP, Xu D, Nelson SJ, Hurd RE, Kelley DA, Pauly JM. Design of flyback echo-planar readout gradients for magnetic resonance spectroscopic imaging. Magn Reson Med. 2005 Nov;54(5):1286-9.
21. Thompson AR, Bracewell RN. Interpolation and Fourier transformation of fringe visibilities. Astron J 1974; 79(1):11–24.

22. Zhang Y, Brady M, Smith S. Segmentation of brain MR images through a hidden Markov random field model and the expectation-maximization algorithm. IEEE Trans Med Imaging 2001; 20(1):45–57.
23. Li X, Vigneron DB, et al. Relationship of MR-derived lactate, mobile lipids, and relative blood volume for gliomas in vivo. AJNR Am J Neuroradiol. 2005 Apr;26(4):760-9.
24. Alger JR, Frank JA, Bizzi A, et al. Metabolism of human gliomas: assessment with H-1 MR spectroscopy and F-18 fluorodeoxyglucose PET. Radiology 1990;177:633–641.
25. Herholz K, Heindel W, Luyten PR, et al. In vivo imaging of glucose consumption and lactate concentration in human gliomas. Ann Neurol 1992;31:319–327.
26. Remy C, Fouilhe N, Barba I, et al. Evidence that mobile lipids detected in rat brain glioma by 1H nuclear magnetic resonance correspond to lipid droplets. Cancer Res 1997;57:407–414.
27. Lin FH, Tsai SY, et al. Sensitivity-encoded (SENSE) proton echo-planar spectroscopic imaging (PEPSI) in the human brain. Magn Reson Med. 2007 Feb;57(2):249-57.

Chapter 6: Kinetic Modeling of Hyperpolarized $^{13}C_1$-Pyruvate Metabolism in Normal Rat Kidneys and TRAMP Mice

6.1 Abstract

Purpose: To investigate metabolic exchange between $^{13}C_1$-pyruvate, $^{13}C_1$-lactate, and $^{13}C_1$-alanine in pre-clinical model systems using kinetic modeling of dynamic hyperpolarized ^{13}C spectroscopic data and to examine the relationship between fitted parameters and dose response.

Materials and Methods: Dynamic ^{13}C spectroscopy data were acquired in normal rats, wild type mice, and TRAMP mice either within a single slice or using a one-dimensional EPSI encoding technique. Rate constants were estimated by fitting a set of exponential equations to the dynamic data. Variations in fitted parameters were used to determine model robustness in 15mm slices containing normal rat kidneys. Parameter values were used to investigate differences in metabolism between and within TRAMP and wild type mice.

Results: The kinetic model was shown here to be robust when fitting data from a rat given similar doses. In normal rats, Michaelis-Menten kinetics were able to describe the dose response of the fitted conversion rate constants with a 13.65% and 16.75% scaled fitting error (SFE) for $k_{pyr\rightarrow lac}$ and $k_{pyr\rightarrow ala}$, respectively. In TRAMP mice, $k_{pyr\rightarrow lac}$ increased an average of 94% after up to 23 days of disease progression, whether the mice were treated or untreated with bicalutamide. Parameters estimated from dynamic ^{13}C 1D-EPSI data were able to differentiate anatomical structures within both wild type and TRAMP mice.

Conclusions: The metabolic parameters estimated using this approach may be useful for *in vivo* monitoring of tumor progression and treatment efficacy, as well as to distinguish between various tissues based on metabolic activity.

6.2 Introduction

The biochemical processes observed in cancerous tissue may be markedly different than those in anatomically similar normal tissue (1,2). A number of such processes have been investigated using *in vivo* ^{13}C magnetic resonance spectroscopy (MRS) and mathematical modeling, but have suffered from relatively low signal to noise ratios (3,4). With the recent development of dynamic nuclear polarization (DNP) it has been possible to increase the ^{13}C MR signal intensity by more than 10,000-fold (5) and to provide dramatic improvements in the ability to study *in vivo* ^{13}C metabolism (6,7,8).

Pyruvate is an important end product of glycolysis that is preferentially converted in the mitochondria of healthy cells to acetyl-CoA and carbon dioxide via pyruvate dehydrogenase (PDH). Acetyl-CoA enters the tricarboxylic acid (TCA) cycle and eventually provides cellular energy as ATP. Without oxygen, or if the TCA cycle is running at full capacity, healthy tissue is forced to maintain energy needs through an alternate pathway that converts pyruvate to lactate via lactate dehydrogenase (LDH) and oxidizes NADH to NAD^+. The NAD^+ is then available to aid in further glycolytic conversion of glucose to pyruvate, providing cellular energy as ATP. Another common pathway for pyruvate is conversion to alanine via alanine transaminase (ALT), which is known to occur in healthy liver and sometimes muscle. Figure 6.1 shows a simplified diagram of these biochemical pathways that follows the C_1 carbon of pyruvate.

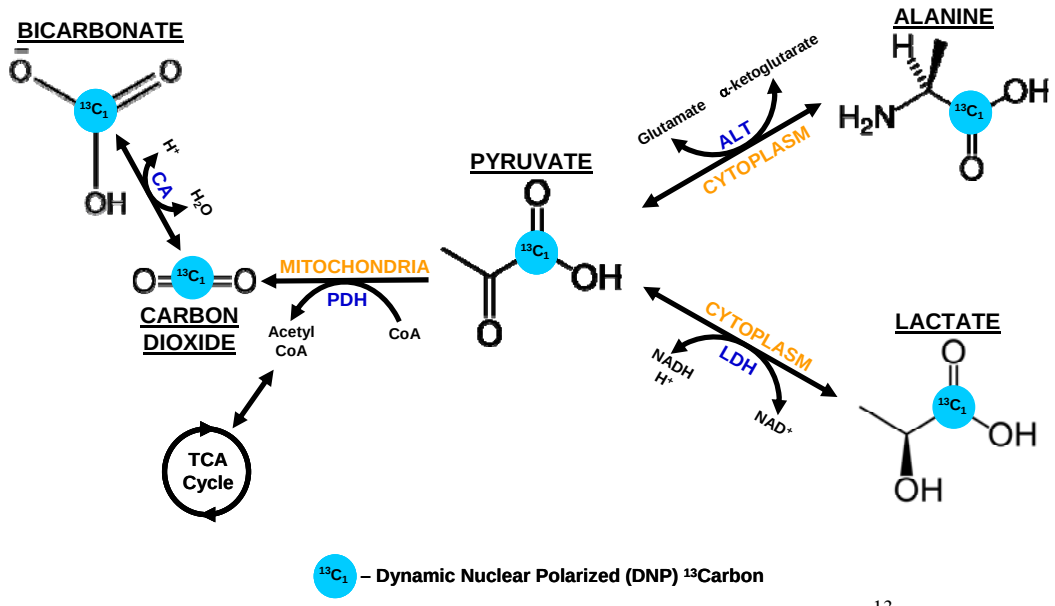

Figure 6.1. Simplified diagram of the biochemical pathways taken by $^{13}C_1$-pyruvate that are visible with the hyperpolarized MR spectroscopy techniques discussed here. The position of the hyperpolarized ^{13}C nucleus is shown in all metabolites with the $^{13}C_1$ symbol. LDH = lactate dehydrogenase. PDH = pyruvate dehydrogenase complex. ALT = alanine transaminase. CA = carbonic anhydrase.

There are a number of changes in the metabolic products of pyruvate that may be of interest for the evaluation of tumors. One key finding is that all tumors preferentially undergo conversion of pyruvate to lactic acid, even in the presence of oxygen. This observation is known as aerobic glycolysis, or the Warburg effect (9,10). Some cancer cells also show changes in transaminase activity, suggesting pyruvate-to-alanine exchange may be enhanced or suppressed, depending on tumor type (11,12,13,14). Therefore, it may be possible to discern healthy tissue from cancerous tissue or to monitor cancer progression by injecting ^{13}C-pyruvate and monitoring the changes in ^{13}C-lactate, ^{13}C-alanine, and/or other metabolic products.

Prostate cancer is the most prevalent form of cancer in men, making up approximately 25% of all new male cancer diagnoses each year in the US (15). A transgenic model of prostate cancer in mice (TRAMP) has been developed for its

similarities to human prostate cancer, in that the tumor will occur spontaneously and follow a similar pattern of progression (16). By studying the TRAMP model using hyperpolarized ^{13}C techniques, important details about prostate cancer may be learned at first, with future studies aimed at investigating other tumor types and cancer in general.

This study uses dynamic MRS data to investigate $^{13}C_1$-pyruvate metabolism in healthy rats and mice, and in TRAMP mice. This agent was chosen because of the relatively long T_1 value of the ^{13}C nucleus in the C_1 position. Simple exponential equations were used to model the dynamic changes in $^{13}C_1$-pyruvate, $^{13}C_1$-lactate, and $^{13}C_1$-alanine levels following a bolus of the hyperpolarized agent. By using a range of different doses of hyperpolarized $^{13}C_1$-pyruvate, it was also possible to investigate the metabolic response to dose through Michaelis-Menten kinetics.

6.3 Methods

6.3.1 Animal and Sample Handling

Twelve healthy male Sprague-Dawley rats (median mass of 330g) were injected with hyperpolarized $^{13}C_1$-pyruvate through a tail vein catheter. Two wild type male and ten TRAMP mice (median mass of 35.5g) were injected with hyperpolarized $^{13}C_1$-pyruvate through a jugular vein catheter. The TRAMP mice were serially studied to monitor tumor progression and treatment response, whereas healthy rats and mice were sacrificed immediately after imaging. The TRAMP mice received up to twelve $^{13}C_1$-pyruvate injections over multiple studies and the healthy mice and rats received a maximum of three $^{13}C_1$-pyruvate injections. Imaging and spectroscopy were performed on a GE 3T MR scanner (GE Healthcare, Waukesha, WI) with a dual-tuned ($^1H/^{13}C$)

quadrature coil, either customized for rats (8cm inner diameter, 9cm length) or customized for mice (4cm inner diameter, 8cm length). The specifics of the animal handling procedure have been reported previously (7,17). All experiments were conducted under a protocol approved by our institutional animal care and use committee.

Hyperpolarized $^{13}C_1$-pyruvate was generated with either a prototype DNP polarizer (17) or a Hypersense® system (Oxford Instruments, Abingdon, UK). Polarization levels ranged from 16–23%. Rats received $^{13}C_1$-pyruvate at concentrations of 9.6–80 mM with volumes of 1.0–3.4 mL, yielding a $^{13}C_1$-pyruvate dose between 28.1 and 724.2 μmol/kg. In TRAMP and wild type mice, doses ranged from 92.4 to 857.9 μmol/kg (10–80 mM, 300–400 μL). The injections lasted between 4 and 13 seconds in rats, but were consistently 12 seconds in the mice.

6.3.2 Data Acquisition

In twelve of the rats (21 scans), dynamic spectroscopy data were acquired from a single 15mm slice centered on the kidneys (Flip angle = 5°, spectral bandwidth (BW) = 5kHz, 2048 spectral points) using a spin-echo RF pulse sequence. Data acquisition began simultaneously with the $^{13}C_1$-pyruvate injection and was repeated every 3 seconds (TR = 3 seconds) over a duration of 189 seconds (64 time points). The same acquisition was used for six TRAMP mice (11 scans) with a 10mm slice centered on the primary tumor in the prostate.

A one-dimensional flyback echo-planar spectroscopic imaging (1D-EPSI) technique was used to acquire dynamic data in two healthy wild type mice (3 scans) and five TRAMP mice (15 scans) (18). The readout gradient was applied in the superior-inferior (SI) dimension during acquisition to allow spatial encoding with a 10mm slice

resolution and a 160mm field of view (FOV). The readout trajectory was designed for a spectral bandwidth of 581.4Hz with 288 spectral points (19). The other acquisition parameters remained the same.

Data were processed using an algorithm that was implemented in the Interactive Data Language (IDL, ITT Visual Information Solutions, Boulder, CO). For the single slice data, a 10Hz Lorentzian apodization was applied to each free-induction decay (FID) prior to Fourier transforming the data. Zero-order phasing was applied to maximize the value of the first point in the FID. The average baseline signal was then subtracted and the real peak heights for $^{13}C_1$-pyruvate, $^{13}C_1$-lactate, and $^{13}C_1$-alanine were used as source data for the models described below. The 1D-EPSI data were processed in the same way but with additional phase corrections to account for the time delays in the FID that result from the spatial encoding (20). These data were zero filled spatially in the SI dimension to 1.25mm resolution in order to more accurately reference the metabolite levels to specific tissues.

6.3.3 Data Analysis

The change in $^{13}C_1$-pyruvate signal over time was first fit to the pyruvate peak height data according to the following piecewise equation:

$$M_{pyr}(t) = \begin{cases} \dfrac{rate_{inj}}{k_{pyr}}\left(1 - e^{-k_{pyr}(t - t_{arrival})}\right) & , \quad t_{arrival} \le t < t_{end} \\ M_{pyr}(t_{end})e^{-k_{pyr}(t - t_{end})} & , \quad t \ge t_{end} \end{cases}, \qquad [6.1]$$

where $M_{pyr}(t)$ represents $^{13}C_1$-pyruvate peak height as a function of time. The parameters fit by this model are: $\boldsymbol{k_{pyr}}$, the rate constant for pyruvate signal decay (in sec^{-1}); $\boldsymbol{rate_{inj}}$, the rate of pyruvate arrival (in a.u. sec^{-1}); and $\boldsymbol{t_{arrival}}$, the time of pyruvate arrival (in sec). The

signal was assumed to be zero for all metabolites prior to $t_{arrival}$. The variable, t_{end}, can be calculated as the sum of the fitted arrival time, $t_{arrival}$, and the known injection duration. The three estimated pyruvate parameters (k_{pyr}, $rate_{inj}$, $t_{arrival}$) were then used to fit $^{13}C_1$-lactate and $^{13}C_1$-alanine dynamic data with the following equation:

$$M_x(t) = \begin{cases} \dfrac{k_{pyr\to x} rate_{inj}}{k_{pyr} - k_x}\left(\dfrac{1-e^{-k_x(t-t_{arrival})}}{k_x} - \dfrac{1-e^{-k_{pyr}(t-t_{arrival})}}{k_{pyr}}\right) & , \quad t_{arrival} \le t < t_{end} \\ \dfrac{M_{pyr}(t_{end})k_{pyr\to x}}{k_{pyr} - k_x}\left(e^{-k_x(t-t_{end})} - e^{-k_{pyr}(t-t_{end})}\right) + M_x(t_{end})e^{-k_x(t-t_{end})} & , \quad t \ge t_{end} \end{cases} \qquad [6.2]$$

Here, x represents either lactate (*lac*) or alanine (*ala*), and $M_x(t)$ represents either $^{13}C_1$-lactate or $^{13}C_1$-alanine peak heights over time. Two parameters were estimated: $\boldsymbol{k_{pyr\to lac}}$ (or $\boldsymbol{k_{pyr\to ala}}$), the rate constant for pyruvate to lactate (or alanine) conversion (sec^{-1}), and $\boldsymbol{k_{lac}}$ (or $\boldsymbol{k_{ala}}$), the rate constant for lactate (or alanine) signal decay (sec^{-1}). Metabolite signal decay rate constants (k_{pyr}, k_{lac}, and k_{ala}) were assumed to consist of both metabolite T_1 decay and signal loss from the 5° RF flip angles. This meant that T_1 values could be estimated for lactate and alanine after accounting for RF excitations and for pyruvate after also accounting for metabolic conversion rate constants. The robustness of parameter estimation was assessed based upon multiple scans on a healthy rat that was given three similar $^{13}C_1$-pyruvate doses (321.4–321.9 μmol/kg).

In addition to metabolism, T_1 effects, and RF excitations, all rate constants may be influenced by other sources of signal change or variation, and they should be thought of as apparent, rather than absolute, rate constants. Also note that reverse exchange of metabolites back to pyruvate was assumed to be negligible in this model to allow fitting of irreversible Michaelis-Menten kinetics. This was further shown to be a reasonable assumption in studies using hyperpolarized $^{13}C_1$-lactate as the injected substrate (22).

The dose effects were represented with a Michaelis-Menten model with maximum reaction velocity (V_{max}) and Michaelis constant (K_m) according to the following equation:

$$k_{pyr\rightarrow x} = \frac{V_{max}}{K_m + Dose_{pyr}}. \qquad [6.3]$$

The kinetics are described here using $k_{pyr\rightarrow lac}$ and $k_{pyr\rightarrow ala}$ instead of initial reaction rates (V_0). This modified Michaelis-Menten equation is simply the inverse of the Hanes-Woolf equation (21). To adhere to the traditional Michaelis-Menten equation, the initial reaction rates (V_0) were also estimated as the product of dose ($Dose_{pyr}$) and conversion rate constants ($k_{pyr\rightarrow lac}$ and $k_{pyr\rightarrow ala}$). Parameter estimates from nineteen scans (11 rats) were used to fit equation 6.3 and to estimate V_{max} and K_m for conversion to lactate and conversion to alanine. The robustness of the model fit was assessed via the scaled fitting error (23).

Metabolic parameters from ten TRAMP mouse tumors (26 scans) and two wild type mice (3 scans) were considered. In wild type mice, comparison data came from the region containing normal prostate. Three TRAMP mice underwent serial studies at a constant pyruvate dose (two with hormone deprivation treatment, one without treatment) to investigate how metabolic parameters change with disease progression. Tumor stage was assessed by size and appearance. Four TRAMP mice (two mid-stage tumors, two late-stage tumors) received a range of three $^{13}C_1$-pyruvate doses on studies performed within a short time period (7 days for one, 4 hours for the other three); these data were used to separately fit equation 6.3 and to describe the individual dose responses. Four TRAMP mice underwent only one dynamic spectroscopy scan.

6.4 Results

A normal rat that was given three similar doses of $^{13}C_1$-pyruvate showed highly reproducible parameter estimates (see Table 6.1). In nineteen scans, with doses ranging from 36 to 724 μmol/kg, the median *in vivo* T_1 estimates (±S.D.) in slices containing normal rat kidney were 12.7±4.4, 12.7±1.7, and 12.1±2.4 seconds for $^{13}C_1$-pyruvate, $^{13}C_1$-lactate, and $^{13}C_1$-alanine, respectively. Figure 6.2a shows an example of dynamic curves of metabolite levels in a 15mm slice containing healthy rat kidney for a dose of 725 μmol/kg, including parameter estimates.

Table 6.1. Reproducibility of metabolic conversion parameters for a 15mm slice containing healthy rat kidney. Parameters are shown with standard error (± se) estimated from the covariance matrix of the model fitting.

$Dose_{pyr}$ (μmol/kg)	$k_{pyr\text{-}lac}$ ± se (s^{-1})	$k_{pyr\text{-}ala}$ ± se (s^{-1})
321.4	0.0235 ± 0.00041	0.0229 ± 0.00068
321.9	0.0217 ± 0.00072	0.0214 ± 0.00081
321.9	0.0255 ± 0.00052	0.0192 ± 0.00064
Mean	**0.0236 ± 0.00055**	**0.0211 ± 0.00071**

Figure 6.3 shows the Michaelis-Menten model fit and parameter estimates for $k_{pyr\rightarrow lac}$ and $k_{pyr\rightarrow ala}$ dose response in the rat kidney. For $k_{pyr\rightarrow lac}$, the estimated maximum reaction rate (V_{max}) was 11.12±1.28 μmol/kg/s and the Michaelis constant (K_m) was 161.45±30.03 μmol/kg. For $k_{pyr\rightarrow ala}$, V_{max} was 10.61±1.77 μmol/kg/s and K_m was 279.55±67.42 μmol/kg. SFE values were less than 20% for lactate (13.65%) and for alanine (16.75%). Traditional Michaelis-Menten curves are shown in Figure 6.4 using the value of V_0 that was calculated from the product of $Dose_{pyr}$ and $k_{pyr\rightarrow lac}$ (or $k_{pyr\rightarrow ala}$).

Figure 6.2b shows an example of dynamic curves in a 10mm slice containing TRAMP tumor for a dose of 725 μmol/kg. The lactate curve is noticeably elevated compared to the results from the rat kidney, thus elevating the estimated value of $k_{pyr \to lac}$. The estimated values of T_1 were also higher in the TRAMP tumor than in the rat kidney. Metabolic parameters were estimated for a 10mm slice centered on tumor in ten TRAMP

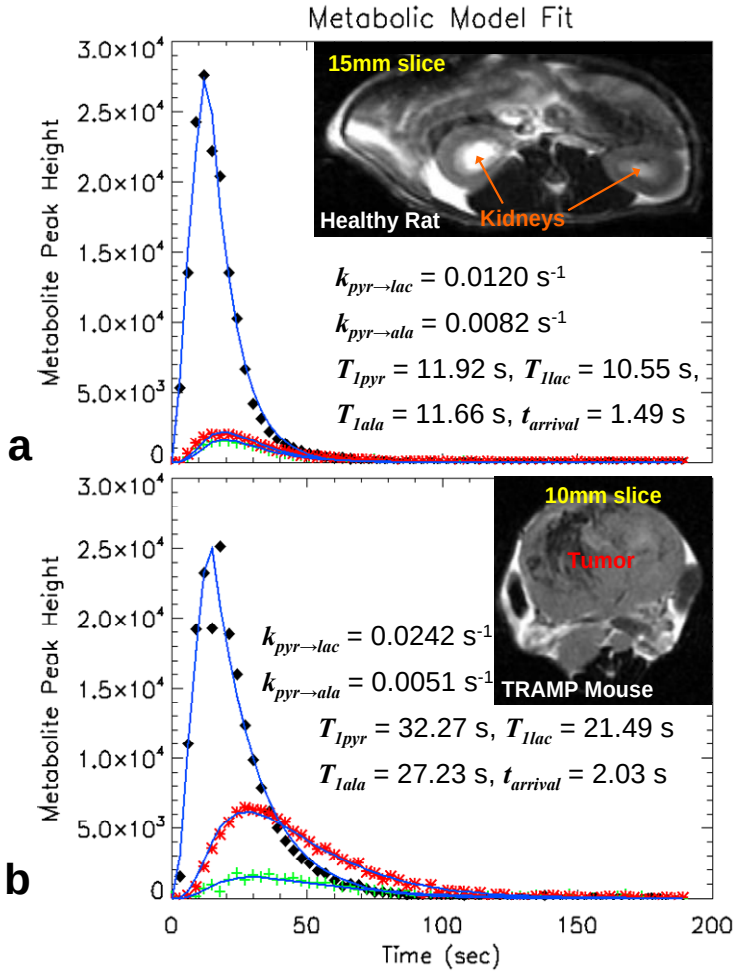

Figure 6.2. Examples of dynamic curves of metabolite levels in a 15mm slice containing healthy rat kidney (**a**) and a 10mm slice containing TRAMP tumor (**b**). Pyruvate data are represented by black diamonds (♦), lactate data are represented by red asterisks (*), alanine data are represented by green plus signs (+), and the estimated best fit lines are represented by the blue lines. Metabolic parameters, estimated from the model in equations 6.1 and 6.2 are also listed inside their respective plots, along with a T_2 fast spin echo (FSE) ^{1}H image of the slice used to acquire ^{13}C data. Both animals received a dose of approximately 725 μmol/kg of hyperpolarized $^{13}C_1$-pyruvate injected over 12 seconds.

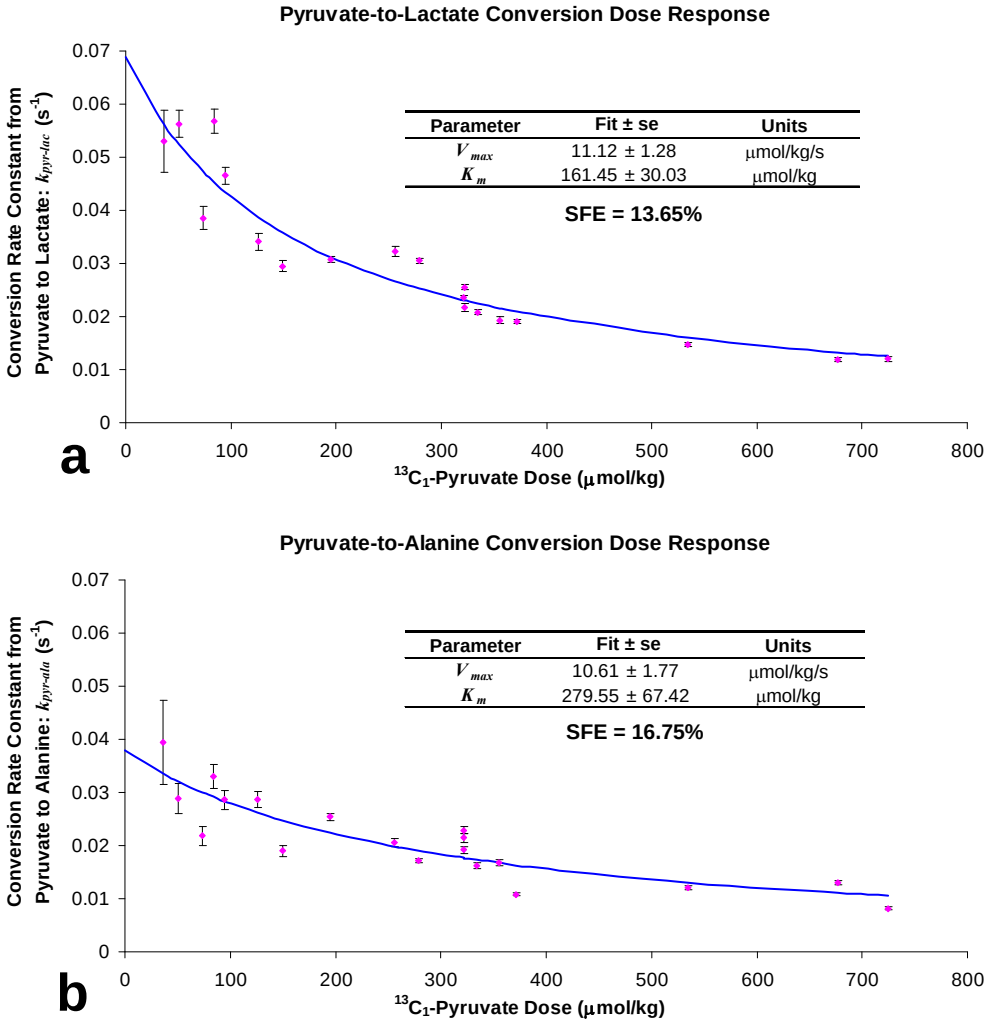

Figure 6.3. Response of metabolic conversion parameters, $k_{pyr\rightarrow lac}$ (**a**) and $k_{pyr\rightarrow ala}$ (**b**), to varying doses of $^{13}C_1$-pyruvate. Data are represented by the pink circles (with ± standard error bars). Michaelis-Menten kinetic parameters (V_{max} and K_m) are listed in the inset tables with standard error (± se) estimated from the covariance matrix of the Michaelis-Menten model fitting. The blue line represents the Michaelis-Menten best fit. Scaled fitting error (SFE) is also shown to represent how well the Michaelis-Menten model fits the dose response data.

mice (26 scans) to give median T_1 values (±S.D.) of 17.4±2.8 s for $^{13}C_1$-lactate and 21.3±6.5 s for $^{13}C_1$-alanine. In the five TRAMP mice and two wild type mice (18 total scans) for whom a dynamic 1D-EPSI acquisition was acquired, it was possible to estimate T_1 values in multiple axial slices. In the region containing mouse kidneys the

median T_1 value for $^{13}C_1$-lactate was 10.4±0.8 s and the median value for $^{13}C_1$-alanine was 6.5±0.9 s. In mice, the T_1 values for $^{13}C_1$-pyruvate were highly variable.

Figure 6.5 shows the dose response in four TRAMP mice that were given three different $^{13}C_1$-pyruvate doses, ranging from 92 to 833 μmol/kg. MS61 (late-stage tumor) was given a range of doses over one week, while MS106 (mid-stage tumor), MS125

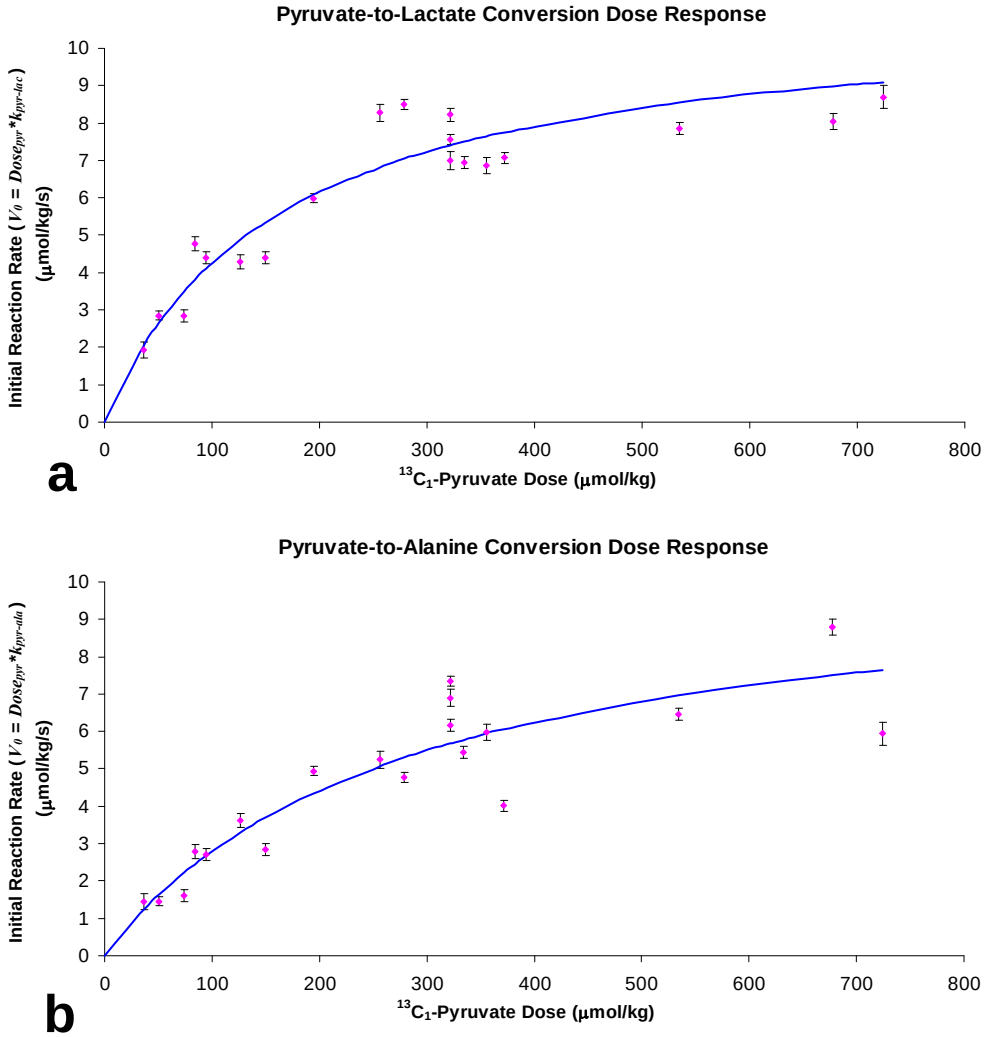

Figure 6.4. Response of initial reaction rates (V_0) to varying doses of $^{13}C_1$-pyruvate. Values for V_0 were calculated as the product of $Dose_{pyr}$ and $k_{pyr \rightarrow lac}$ (**a**) and $Dose_{pyr}$ and $k_{pyr \rightarrow ala}$ (**b**). Error bars were calculated using error propagation (product of standard error of the estimated parameter and $Dose_{pyr}$). Michaelis-Menten kinetic parameters (V_{max} and K_m) from Figure 6.2 were used to calculate the blue best-fit line.

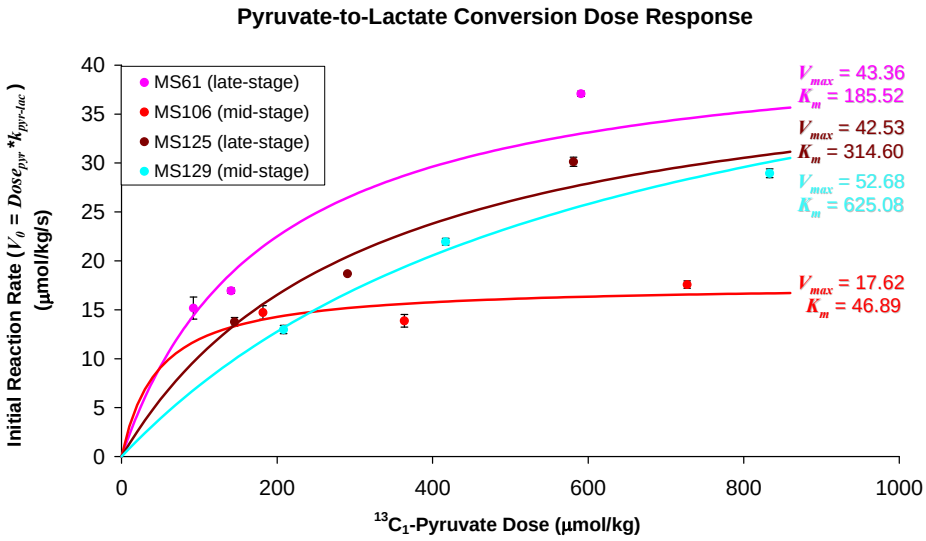

Figure 6.5. Response of initial pyruvate-to-lactate reaction rates in four 10mm slices containing TRAMP tumor to varying doses of $^{13}C_1$-pyruvate. All mice had developed a transgenic prostate tumor prior to these data acquisitions. Best fit estimates of Michaelis-Menten kinetic parameters are shown next to the best fit curves (V_{max} in µmol/kg/s, K_m in µmol/kg). MS61 (pink) received three injections spanning seven days. MS106 (red), MS125 (brown), and MS129 (cyan) all received three injections within a four hour period. MS106 and MS129 were categorized as mid-stage tumors and MS61 and MS125 were categorized as late-stage tumors.

(late-stage tumor), and MS129 (mid-stage tumor) received all of the doses within the same exam (~4 hours). All four mice exhibited a $k_{pyr \rightarrow lac}$ dose response that could be represented by Michaelis-Menten kinetics. The late stage tumors appeared to have similar dose responses and V_{max} values (~43 µmol/kg/s). One of the mid-stage tumors (MS106) showed a noticeably lower dose response curve (V_{max} = 17.6 µmol/kg/s), while the other mid-stage tumor (MS129) had a similar dose response to the late-stage tumors (V_{max} = 52.7 µmol/kg/s).

Three TRAMP mice were studied serially for up to 23 days (11 total scans) and were given a dose of approximately 800 µmol/kg (727–858 µmol/kg). The untreated

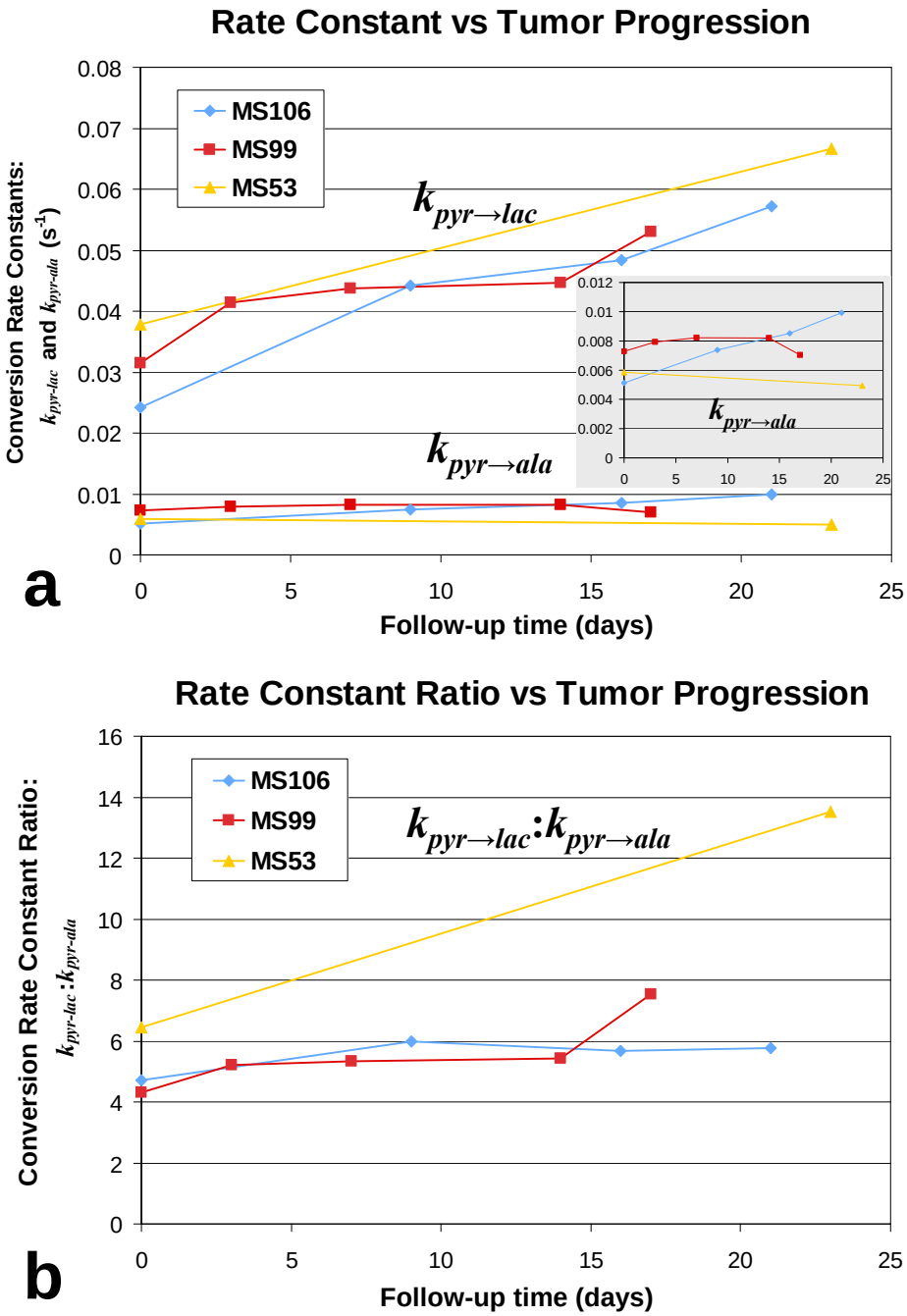

Figure 6.6. Serial plots of estimated metabolic conversion parameters ($k_{pyr\rightarrow lac}$ and $k_{pyr\rightarrow ala}$) over time (**a**) and their ratios ($k_{pyr\rightarrow lac}$:$k_{pyr\rightarrow ala}$) over time (**b**) for three mice with a transgenic prostate tumor. A rescaled plot of $k_{pyr\rightarrow ala}$ is also shown (**a**). One mouse (MS53) was untreated, while two mice (MS99 and MS106) were treated with hormone deprivation (bicalutamide). $k_{pyr\rightarrow lac}$ values appear to increase over time in all animals; however, $k_{pyr\rightarrow lac}$:$k_{pyr\rightarrow ala}$ values appear stable over time for treated animals, while $k_{pyr\rightarrow lac}$:$k_{pyr\rightarrow ala}$ more than doubles in the untreated animal over a 23 day period.

mouse (MS53) showed a large increase in $k_{pyr\rightarrow lac}$ in a 10mm slice containing tumor over a 23 day period, with values for $k_{pyr\rightarrow lac}$ increasing by more than 76% (from 0.0378 to 0.0667 sec^{-1}). Additionally, $k_{pyr\rightarrow ala}$ was fairly stable in the untreated mouse (decreased from 0.0058 to 0.0049 sec^{-1}) and the ratio of $k_{pyr\rightarrow lac}$:$k_{pyr\rightarrow ala}$ increased by more than 109% (from 6.46 to 13.52). The two other TRAMP mice that were studied serially (MS99 and MS106) were treated daily with hormone deprivation (100 mg/kg bicalutamide). The ratio of $k_{pyr\rightarrow lac}$:$k_{pyr\rightarrow ala}$ remained lower for the treated mice relative to the untreated mouse, but there did not appear to be a significant difference between the treated mice and the untreated mouse in any of the metabolic parameters. Figure 6.6 shows how the metabolic conversion parameters changed over time in these mice.

Figure 6.7 shows 1D-EPSI data collected from a wild type mouse (Figure 6.7a-d) compared to a TRAMP mouse (Figure 6.7e-h). In ten TRAMP mice (18 scans) that were given 300–400μL of 80mM $^{13}C_1$-pyruvate (median±S.D. = 790±96.7 μmol/kg) and two wild type mice (2 scans) given 350μL of 80mM $^{13}C_1$-pyruvate (815±11.8 μmol/kg), there were significant differences in estimated $k_{pyr\rightarrow ala}$ values ($p<0.02$) and $k_{pyr\rightarrow lac}$:$k_{pyr\rightarrow ala}$ ratios ($p<0.003$) in the region containing the prostate or tumor, but no statistically significant difference in $k_{pyr\rightarrow lac}$ values ($p>0.05$). In TRAMP mice that had varying levels of disease development, all $k_{pyr\rightarrow ala}$ values were lower and all $k_{pyr\rightarrow lac}$:$k_{pyr\rightarrow ala}$ ratios higher compared to the two wild type mice in the same region. Median $k_{pyr\rightarrow lac}$ and $k_{pyr\rightarrow ala}$ values (±S.D.) for TRAMP mice were 0.0444±0.0122 sec^{-1} and 0.0075±0.0022 sec^{-1}, ranging from 0.0242 to 0.0722 sec^{-1} and 0.0028 to 0.0106 sec^{-1}, respectively. Median $k_{pyr\rightarrow lac}$:$k_{pyr\rightarrow ala}$ ratios (±S.D.) were 5.72±3.77, ranging from 4.07 to 16.98. The two wild type mice showed values for $k_{pyr\rightarrow lac}$, $k_{pyr\rightarrow ala}$, and $k_{pyr\rightarrow lac}$:$k_{pyr\rightarrow ala}$ ranging from 0.0294 to

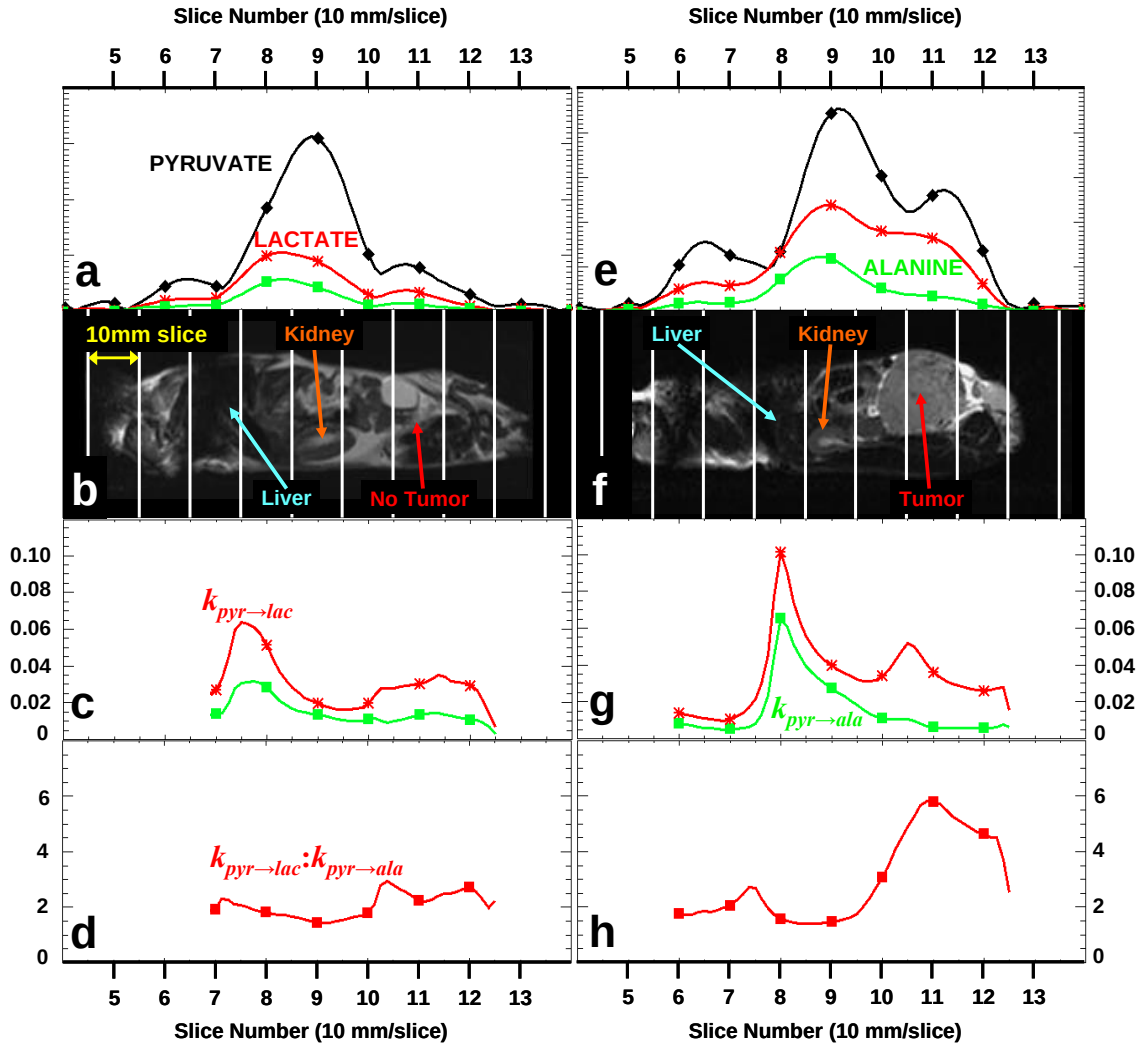

Figure 6.7. One dimensional flyback echo planar spectroscopic imaging (1D-EPSI) data from a wild type mouse (**a-d**) and a TRAMP mouse (**e-h**), each receiving 300–350 µL of 80mM hyperpolarized $^{13}C_1$-pyruvate. Spectroscopic data was zero-filled in the SI dimension to eight times the acquired resolution. Figures 6.7a and 6.7e show the metabolite signal along the superior-inferior (SI) dimension between 27 and 30 seconds post injection acquired for pyruvate (black), lactate (red), and alanine (green), with arbitrary units. Figures 6.7b and 6.7f are sagittal T2 FSE images that show the anatomical structures located within each 10mm slice. Kidneys, liver, and tumor (or "no tumor") are labeled with colored arrows. Figures 6.7c and 6.7g show $k_{pyr\rightarrow lac}$ (red) and $k_{pyr\rightarrow ala}$ (green), in sec^{-1}, along the SI dimension in the healthy mouse (c) and TRAMP mouse (g). Figures 6.7d and 6.7h show the ratios of metabolic conversion parameters along the SI dimension. There are noticeable differences between the TRAMP mouse and healthy mouse, as well as between each animals' anatomical structures.

0.0468 sec^{-1}, 0.0115 to 0.0129 sec^{-1}, and 2.55 to 3.64, in the region containing the prostate. Additionally, differences in metabolic parameters between anatomical structures were present, and examples of this can be easily seen in the Figure 6.7.

6.5 Discussion

This study demonstrates the ability to apply kinetic modeling of *in vivo* changes in $^{13}C_1$-pyruvate and two of its direct metabolites to Sprague-Dawley rats, wild type mice, and TRAMP mice. The parameters estimated by this analysis appear to be robust but are highly dependent on $^{13}C_1$-pyruvate dose, as well as tissue type and disease state. In using hyperpolarized $^{13}C_1$-pyruvate to investigate differences in metabolic activity for various tissues, it is therefore critical to consider the dose that is being used.

The variation in estimated parameters observed when conducting three identical studies on a rat was minimal. The T_1 estimates in slices containing rat kidneys were in agreement with previously published T_1 estimates from the whole rat (8). A robust fit to the dose response was achieved with a Michaelis-Menten model (SFE < 20%) in nineteen scans from rats. The model fitting results in normal rats suggest that the technique used here is a robust option that may be valuable to investigate ^{13}C metabolism in other model systems.

Reverse exchange of lactate and alanine back to pyruvate was assumed to be negligible in this model for various reasons: 1) the expected large preference of forward exchange and the relatively large amount of labeled pyruvate injected will cause the forward reaction rate to be much larger than the reverse (22); 2) the mathematical model fitting complexity was greatly reduced by allowing separate fits of each metabolite; 3) the short time frame in which data are acquired allows for the estimation of the initial

reaction rate as a rate constant; and 4) Michaelis-Menten kinetics assume the reaction is irreversible, thus no reverse exchange should take place.

The TRAMP mouse model was included in this study because of its similarity to human prostate cancer, in that the tumors occur spontaneously and follow a similar pattern of progression. Single slice dynamic ^{13}C spectroscopy was applied to demonstrate the potential for assessing dose response and for monitoring tumor progression and treatment effects. The 1D-EPSI technique was equally effective at monitoring dose response and disease state with the added advantage of being able to show differences in anatomy within multiple slices from the animal.

The TRAMP mice used in this study had the potential to undergo significant disease development over the duration in which they were studied. This meant that dose response studies had to be performed within a relatively short period of time in order to avoid complications associated with tumor progression. One TRAMP dose response study spanned 7 days and three studies were performed during one anesthetic period (within 4 hours), and Michealis-Menten kinetics were able to describe their dose response. However, the dose response kinetics did not appear to show a clear distinction between tumor stage in the relatively small number of mice considered.

Serial studies on three of the TRAMP mice showed how kinetic modeling of dynamic ^{13}C spectroscopy might be valuable in monitoring disease state. One of the TRAMP mice was untreated, and the estimated metabolic parameters showed a noticeable change, larger than the reproducibility error observed in rats. The 76% increase in $k_{pyr\rightarrow lac}$ and the 109% increase in $k_{pyr\rightarrow lac}$:$k_{pyr\rightarrow ala}$ may therefore be attributed to tumor progression. The two TRAMP mice treated with hormone deprivation

(bicalutamide) showed similar progression in $k_{pyr \rightarrow lac}$ with values that continually increased with each exam. However, the $k_{pyr \rightarrow lac}$:$k_{pyr \rightarrow ala}$ values appeared to be relatively stable over the period that they were studied (CV = 10% and 21%). When using volume and appearance as a measure of tumor progression, the prostate tumors in the two treated animals did not seem to progress as aggressively as the untreated mouse. However, this is a heterogeneous model of prostate cancer, and some tumors will naturally progress faster than others. It is not clear if hormone deprivation or phenotype was responsible for the slower tumor growth. A larger number of serial TRAMP studies are required in order to make more significant claims.

In the region containing prostate, the estimated pyruvate-to-alanine conversion rate constants ($k_{pyr \rightarrow ala}$) were lower in TRAMP mice and the conversion rate constant ratios ($k_{pyr \rightarrow lac}$:$k_{pyr \rightarrow ala}$) were higher compared to wild type mice who received a similar dose of approximately 800 μmol/kg. In an earlier 2D ^{13}C spectroscopic imaging study, Golman, et al. showed similarly high lactate with low alanine levels in engrafted rat tumors, but the opposite in normal skeletal muscle (6). These results suggest that the conversion of pyruvate to lactate may not only increase in tumors, but that it may increase more significantly relative to pyruvate-to-alanine conversion.

T_1 values for $^{13}C_1$-lactate and $^{13}C_1$-alanine that were estimated in slices containing TRAMP prostate tumor were on the average higher compared to slices containing TRAMP mouse kidney and normal rat and normal mouse kidney; yet, T_1 values were not always reliably estimated for $^{13}C_1$-pyruvate in these regions. This issue may be due to a reflux of lactate and alanine back to pyruvate, flow related issues, or other unknown variables. The range of metabolite T_1 values exhibited when assessed via 1D-EPSI

suggests that there are distinct T_1 values for lactate, alanine, and pyruvate in various tissues. The estimated arrival time ($t_{arrival}$) varied throughout the mouse anatomy as well, with the earliest arrival times being near the upper abdomen and heart, which is expected due to the jugular vein injections.

Differences in estimated metabolic parameters were also observed in anatomical regions (as seen in the example in Figure 6.7). Slices containing kidneys in wild type mice and TRAMP mice produced the largest signal of all metabolites, while slices containing liver appeared to produce relatively low signal but exhibited the highest metabolic conversion rate constants. This suggests that anatomy is a determinant of metabolic behavior and the metabolic differences can be measured with hyperpolarized ^{13}C techniques. Studies are underway to further investigate variations in metabolism across anatomical regions using a 2D and 3D dynamic spectroscopic imaging protocol, aiming to more accurately describe distinct metabolic activity in specific tissue types (24).

6.6 Conclusion

This study demonstrated the ability to monitor *in vivo* changes in ^{13}C metabolism using kinetic modeling of dynamic ^{13}C spectroscopy. As expected from Michaelis-Menten kinetic theory, the substrate dose had a critical influence on metabolic parameters. The metabolic parameters estimated using this approach may be useful in monitoring tumor progression and treatment efficacy, as well as in distinguishing metabolic activity among different tissues.

6.7 References

1. Ross BD. The biochemistry of living tissues: examination by MRS. NMR Biomed. 1992 Sep-Oct;5(5):215-9. Review.
2. Koukourakis MI, Giatromanolaki A, Sivridis E, Gatter KC, Harris AL; Tumor and Angiogenesis Research Group. Pyruvate dehydrogenase and pyruvate dehydrogenase kinase expression in non small cell lung cancer and tumor-associated stroma. Neoplasia. 2005 Jan;7(1):1-6.
3. Katz-Brull R, Margalit R, Bendel P, Degani H. Choline metabolism in breast cancer; 2H-, 13C- and 31P-NMR studies of cells and tumors. MAGMA. 1998 Aug;6(1):44-52.
4. Artemov D, Bhujwalla ZM, Pilatus U, Glickson JD. Two-compartment model for determination of glycolytic rates of solid tumors by in vivo 13C NMR spectroscopy. NMR Biomed. 1998 Nov;11(8):395-404.
5. Ardenkjaer-Larsen JH, Fridlund B, Gram A, Hansson G, Hansson L, Lerche MH, Servin R, Thaning M, Golman K. Increase in signal-to-noise ratio of > 10,000 times in liquid-state NMR. Proc Natl Acad Sci U S A. 2003 Sep 2;100(18):10158-63. Epub 2003 Aug 20.
6. Golman K, Zandt RI, Lerche M, Pehrson R, Ardenkjaer-Larsen JH. Metabolic imaging by hyperpolarized 13C magnetic resonance imaging for in vivo tumor diagnosis. Cancer Res. 2006 Nov 15;66(22):10855-60.
7. Chen AP, Albers MJ, Cunningham CH, Kohler SJ, Yen YF, Hurd RE, Tropp J, Bok R, Pauly JM, Nelson SJ, Kurhanewicz J, Vigneron DB. Hyperpolarized C-13 spectroscopic imaging of the TRAMP mouse at 3T-initial experience. Magn Reson Med. 2007 Dec;58(6):1099-106.
8. Golman K, in 't Zandt R, Thaning M. Real-time metabolic imaging. Proc Natl Acad Sci U S A. 2006 Jul 25;103(30):11270-5. Epub 2006 Jul 12.
9. Warburg O. On the origin of cancer cells. Science. 1956 Feb 24;123(3191):309-14.
10. Lu H, Forbes RA, Verma A. Hypoxia-inducible factor 1 activation by aerobic glycolysis implicates the Warburg effect in carcinogenesis. J Biol Chem. 2002 Jun 28;277(26):23111-5. Epub 2002 Apr 9.
11. Dröge W, Eck HP, Kriegbaum H, Mihm S. Release of L-alanine by tumor cells. J Immunol. 1986 Aug 15;137(4):1383-6.
12. Brennan L, Hewage C, Malthouse JP, McBean GJ. Gliotoxins disrupt alanine metabolism and glutathione production in C6 glioma cells: a 13C NMR spectroscopic study. Neurochem Int. 2004 Dec;45(8):1155-65.
13. Ronen SM, Volk A, Mispelter J. Comparative NMR study of a differentiated rat hepatoma and its dedifferentiated subclone cultured as spheroids and as implanted tumors. NMR Biomed. 1994 Sep;7(6):278-86.
14. Harding HR, Rosen F, Nichol CA. Depression of Alanine Transaminase Activity in the Liver of Rats Bearing Walker Carcinoma 256. Cancer Res. 1964 Sep;24:1318-23
15. Cancer Statistics 2008. American Cancer Society. <http://www.cancer.org/docroot/PRO/content/PRO_1_1_Cancer_Statistics_2008_Presentation.asp>.

16. Gingrich JR, Barrios RJ, Morton RA, Boyce BF, DeMayo FJ, Finegold MJ, Angelopoulou R, Rosen JM, Greenberg NM. Metastatic prostate cancer in a transgenic mouse. Cancer Res. 1996 Sep 15;56(18):4096-102.
17. Kohler SJ, Yen Y, Wolber J, Chen AP, Albers MJ, Bok R, Zhang V, Tropp J, Nelson S, Vigneron DB, Kurhanewicz J, Hurd RE. In vivo 13 carbon metabolic imaging at 3T with hyperpolarized 13C-1-pyruvate. Magn Reson Med. 2007 Jul;58(1):65-9.
18. Chen AP, Hurd RE, Cunningham CH, Li Y, Zierhut ML, Bok R, Kurhanewicz J, Nelson SJ, Vigneron DB. Spatially Resolved 13C Hyperpolarized Dynamic MRS using Flyback Echo-Planar Readout Trajectory. Proceedings 49th Scientific Meeting ENC, Asilomar, CA, 2008. #60
19. Cunningham CH, Chen AP, Albers MJ, Kurhanewicz J, Hurd RE, Yen YF, Pauly JM, Nelson SJ, Vigneron DB. Double spin-echo sequence for rapid spectroscopic imaging of hyperpolarized 13C. J Magn Reson. 2007 Aug;187(2):357-62. Epub 2007 Jun 2.
20. Cunningham CH, Vigneron DB, Chen AP, Xu D, Nelson SJ, Hurd RE, Kelley DA, Pauly JM. Design of flyback echo-planar readout gradients for magnetic resonance spectroscopic imaging. Magn Reson Med. 2005 Nov;54(5):1286-9.
21. Hanes CS. Studies on plant amylases: The effect of starch concentration upon the velocity of hydrolysis by the amylase of germinated barley. Biochem J. 1932;26(5):1406-21.
22. Chen AP, Kurhanewicz J, Bok R, Xu D, Joun D, Zhang V, Nelson SJ, Hurd RE, and Vigneron DB. In vivo Hyperpolarized 13C MRS/MRSI Using 13C-lactate as the Pre-polarized Substrate. Proceedings 16th Scientific Meeting ISMRM, Toronto, Canada, 2008. #3192
23. Li KL, Zhu XP, Jackson A. Parametric mapping of scaled fitting error in dynamic susceptibility contrast enhanced MR perfusion imaging. Br J Radiol. 2000 May;73(869):470-81.
24. Larson PEZ, Kerr AB, Chen AP, Lustig MS, Zierhut ML, Hu S, Cunningham CH, Pauly JM, Kurhanewicz J, Vigneron DB. Multiband Excitation Pulses for Hyperpolarized 13C Dynamic Chemical Shift Imaging. J Magn Reson. Submitted 29 April, 2008.

Chapter 7: How Does the Dose of Hyperpolarized $^{13}C_1$-Pyruvate Influence the Observed Metabolic Parameters in Canine Prostate?

7.1 Abstract

Purpose: To investigate the effects of pyruvate dose on metabolite SNR and metabolic rate constants using ^{13}C dynamic spectroscopy and spectroscopic imaging of the canine prostate.

Methods: Twelve healthy adult male beagles were injected up to four times with hyperpolarized $^{13}C_1$-pyruvate and either dynamic spectroscopy or spectroscopic imaging data were acquired. Peak heights for $^{13}C_1$-pyruvate, $^{13}C_1$-lactate, and ^{13}C-bicarbonate were obtained from magnitude spectra. Metabolite SNR values were calculated, rate constants were estimated, and the results were compared across dose levels (45–397 μmol/kg). Michaelis-Menten parameters were determined from the metabolic rate constants.

Results: Pyruvate SNR showed a positive correlation with dose levels for both the dynamic spectroscopy and spectroscopic imaging datasets. Lactate and bicarbonate SNR showed a variable dose effect. Estimated rate constants for pyruvate-to-lactate and pyruvate-to-bicarbonate ^{13}C exchange decreased as dose increased, as predicted by Michaelis-Menten kinetics. Mean Lac:Pyr ratios (±SD) in prostate were 1.16±0.15, 1.11±0.16, and 0.25±0.10 for 45–46, 89–90, and 350–397 μmol/kg dose levels, respectively.

Conclusion: This study demonstrates that $^{13}C_1$-pyruvate dose is a critical factor to consider when evaluating variations in metabolic parameters compared to disease state or treatment effects. The detection of $^{13}C_1$-lactate was similar at all doses used in this study.

7.2 Introduction

Methods that have been used to retain dynamic nuclear polarization (DNP) in solution have demonstrated ^{13}C MR signal enhancements of greater than 10,000-fold as compared to thermal equilibrium (1). This breakthrough technology has spurred cutting-edge research investigating in vitro and in vivo ^{13}C metabolism. Due to its intermediate involvement in glycolysis and the tricarboxylic acid (TCA) cycle, and because it possesses a carboxyl group (C_1) with a relatively slow spin-lattice relaxation rate ($1/T_1$), $^{13}C_1$-pyruvate is a common choice for hyperpolarized ^{13}C research. Specifically, DNP polarized $^{13}C_1$-pyruvate has been used as an exogenous agent in pigs, rats, and mice to observe in vivo metabolic changes associated with fermentation (lactate), transamination (alanine), and oxidative decarboxylation (bicarbonate) (2,3,4,5,6). Thus, the presence of lactate, alanine, and bicarbonate can be used to evaluate pathways for anaerobic respiration, transamination, and the TCA cycle, respectively.

Prostate cancer is the most common form of cancer in men, occurring in one out of every six American men at some point in his life (7). This high prevalence has provoked much scientific research on prostate cancer's cause, as well as on early detection and treatment. In particular, a transgenic model of mouse prostate cancer (TRAMP) has been developed, in which mice spontaneously develop prostate tumors that follow a similar pattern of progression to human prostate cancer (8).

Several recent studies have used hyperpolarized $^{13}C_1$-pyruvate to investigate metabolic activity in TRAMP mice (9,10,11,12). As described in Chapter 6, we have investigated the effects of $^{13}C_1$-pyruvate dose on the kinetic modeling of dynamic spectroscopic data in Sprague-Dawley rat kidneys and TRAMP tumors. Specifically, two

metabolic pathways were investigated: fermentation of pyruvate to lactate via the enzyme lactate dehydrogenase (LDH), and transamination of pyruvate to alanine via the enzyme alanine transaminase (ALT). The results showed that a simple compartmental model allowed for robust model fitting, and that dose was highly influential on the estimated parameters, as predicted by Michaelis-Menten kinetics. Additionally, the results suggested that as TRAMP tumors progress, the metabolic rate for pyruvate-to-lactate ^{13}C exchange also increases. Another study carried out in TRAMP mice investigated differences between stages of prostate cancer assessed through non-dynamic hyperpolarized $^{13}C_1$-pyruvate spectroscopic imaging after a predetermined pyruvate dose (12). The results showed that the lactate signal and the lactate to pyruvate signal ratio (Lac:Pyr) increased with tumor grade. Taken together, these two studies provide evidence that LDH activity increases with tumor malignancy, and that this can be seen in both dynamic spectroscopy and spectroscopic imaging.

MR data acquisitions are highly dependent on radiofrequency (RF) coil hardware, and most hardware used for animal research is not suitable for human use. Before hyperpolarized ^{13}C research can be performed on humans, it is important to test the MR system in an alternate model in a similar environment to the clinic. Previous studies have shown that canine prostates are similar to human prostates in size and anatomy, and that a prototype endorectal receive coil and clamshell transmit coil (13) worked well in dogs (14). However, before moving to humans it is necessary to determine the range of doses that will have adequate sensitivity.

This study was conducted to investigate in canine prostate how $^{13}C_1$-pyruvate dose affects spectroscopic results using the same RF coil and data acquisition parameters

that are relevant for human studies. Specifically, dynamic spectroscopic data and spectroscopic images were acquired on canine prostates at three different pyruvate doses. Dynamic data were analyzed to assess the influence of dose on signal to noise ratios (SNR) and metabolic rate constants, while the spectroscopic imaging data were evaluated to investigate dose-dependent changes in the SNR of lactate and pyruvate.

7.3 Methods

7.3.1 Animal Handling

Twelve healthy adult male beagles, median mass 11.5 kg (6.9–14.3 kg), were given up to four injections of hyperpolarized $^{13}C_1$-pyruvate through an 18 or 20 gauge catheter inserted into the cephalic vein (one of the twelve received a jugular vein catheter). Acepromazine was first administered for sedation, followed by propofol and atropine for induction of full anesthesia. Anesthesia was maintained with 2% isoflurane, and spontaneous respiration was allowed. A customized dual tuned ($^{1}H/^{13}C$) endorectal RF receive coil (13) was inserted and positioned next to the prostate after the dog was placed in a GE 3T MR scanner (GE Healthcare, Waukesha, WI). All RF excitation pulses originated from a customized clamshell transmit coil (13) surrounding the animal.

7.3.2 Sample Preparation

The process used to generate hyperpolarized $^{13}C_1$-pyruvate has been described previously (4). Samples were polarized for 45–90 minutes prior to being dissolved in a TRIS/NaOH/EDTA dissolution medium, creating a 250mM pyruvate solution. An aliquot of the pyruvate solution was then used to measure the polarization as the rest of the solution was transferred into the shielded room for injection into the dog. Median

polarization levels were 18.3±1.4%. Volumes ranging from 2 mL to 20 mL were injected into the dog, followed by a saline flush, at a constant rate for each ^{13}C MR data acquisition. The doses ranged from 44.6 to 396.8 μmol/kg and were administered for durations of 1.7 to 12.7 seconds. The median pH of the injected solution was 7.63±0.10.

7.3.3 Dynamic ^{13}C Spectroscopy

Dynamic ^{13}C spectroscopic data were acquired on nine animals (11 scans). The acquisition employed a 5° flip angle (α) with either a 6 cm slice selective or a non-selective excitation pulse. ^{13}C data were acquired every 3 seconds (TR=3) for 189 seconds, beginning simultaneously with hyperpolarized pyruvate injection with a 5 kHz spectral bandwidth and 2.4 Hz resolution.

The time domain data were apodized with a 10 Hz Lorentzian filter and Fourier transformed to provide a time course of spectra. Peak heights in the magnitude spectra were calculated for lactate (185 ppm), pyruvate (173 ppm), and bicarbonate (162 ppm) at each time point (four of the scans did not have any observable bicarbonate). SNR values were calculated as the maximum signal divided by the standard deviation of signal intensities between 240 and 250 ppm, starting 2 minutes after injection. SNR values were normalized to be equivalent to 20% polarization.

A kinetic model was fit separately to each metabolite's dynamic data. The model fit to pyruvate data was used as an input function for the products (lactate and bicarbonate). Thus, reverse rate constants for lactate or bicarbonate to pyruvate were assumed negligible, allowing the use of a Michaelis-Menten model. Equation 7.1 describes the changes in signal intensity for pyruvate.

$$M_{pyr}(t) = \begin{cases} \dfrac{rate_{inj}}{k_{pyr}}\left(1 - e^{-k_{pyr}(t - t_{arrival})}\right) & , \quad t_{arrival} \le t < t_{end} \\ M_{pyr}(t_{end})e^{-k_{pyr}(t - t_{end})} & , \quad t \ge t_{end} \end{cases} \qquad [7.1]$$

Here M_{pyr} represents $^{13}C_1$-pyruvate peak height over time. The fitted parameters are: $rate_{inj}$, the rate of pyruvate signal change due to the injection (in a.u. sec^{-1}); k_{pyr}, the decay constant for pyruvate (in sec^{-1}); and $t_{arrival}$, the injection arrival time (in sec). The injection duration is known, thus t_{end} is the sum of $t_{arrival}$ and the injection duration. Once fit, these parameters are held fixed for fitting the lactate and bicarbonate models.

Although the model used to describe $^{13}C_1$-lactate changes was the same for ^{13}C-bicarbonate, it should be noted that LDH is responsible for mediating pyruvate-to-lactate conversion, while the enzymes pyruvate dehydrogenase (PDH) and carbonic anhydrase (CA) are responsible for the appearance of ^{13}C-bicarbonate. Equation 7.2 describes the model used to fit the lactate and bicarbonate data as represented by M_x.

$$M_x(t) = \begin{cases} \dfrac{k_{pyr \to x} rate_{inj}}{k_{pyr} - k_x}\left(\dfrac{1 - e^{-k_x(t - t_{arrival})}}{k_x} - \dfrac{1 - e^{-k_{pyr}(t - t_{arrival})}}{k_{pyr}}\right) & , \quad t_{arrival} \le t < t_{end} \\ \dfrac{M_{pyr}(t_{end})k_{pyr \to x}}{k_{pyr} - k_x}\left(e^{-k_x(t - t_{end})} - e^{-k_{pyr}(t - t_{end})}\right) + M_x(t_{end})e^{-k_x(t - t_{end})} & , \quad t \ge t_{end} \end{cases} \qquad [7.2]$$

The fitted parameters here are $k_{pyr \to x}$ (sec^{-1}) and k_x (sec^{-1}), where x represents either lactate (*lac*) or bicarbonate (*bic*). Thus, $k_{pyr \to lac}$ is the rate constant for pyruvate to lactate and $k_{pyr \to bic}$ is the same for bicarbonate. All decay constants (k_{pyr}, k_{lac}, and k_{bic}) were assumed to consist of decay from T_1 effects and RF excitation. Because pyruvate is the substrate in these reactions, it will also experience signal decay. T_1 values were calculated for each metabolite as follows:

$$T_{1pyr} = \frac{1}{k_{pyr} - \left(k_{pyr \to lac} + k_{pyr \to bic} + \frac{1 - \cos\alpha}{TR} \right)}$$

$$T_{1lac} = \frac{1}{k_{lac} - \frac{1 - \cos\alpha}{TR}} \qquad [7.3]$$

$$T_{1bic} = \frac{1}{k_{bic} - \frac{1 - \cos\alpha}{TR}}$$

A Michaelis-Menten model was used to investigate the effects of substrate dose on fitted rate constants ($k_{pyr \to lac}$ and $k_{pyr \to bic}$).

$$k_{pyr \to x} = \frac{V_{max}}{K_m + Dose_{pyr}} \qquad [7.4]$$

Estimated parameters for this model were maximum reaction velocity (V_{max}, in μmol kg^{-1} sec^{-1}) and the Michaelis constant (K_m, in μmol kg^{-1}). The Michaelis-Menten kinetics were described here using $k_{pyr \to lac}$ and $k_{pyr \to bic}$ instead of initial reaction rates (V_0). This modified Michaelis-Menten equation is simply the inverse of the Hanes-Woolf equation (15).

7.3.4 Spectroscopic Imaging

Seven dogs underwent two-dimensional ^{13}C MR spectroscopic imaging scan (2D-MRSI). For doses below 100 μmol/kg, image acquisition did not start until 25 seconds after injection, with a 45 second imaging delay being used for larger doses. The 2D image was acquired in a 10 mm axial slice containing the prostate. A 16 x 16 elliptical phase encoding matrix was created by acquiring only the central 80% of k-space, starting in the center and moving radially outwards, with a TR of 80 ms. The flip angle was set to increase with each phase encode to compensate for signal decay from the RF excitations,

which would otherwise act as an unwanted spatial filter. The 2D acquisition resulted in an 8 x 8 cm^2 FOV, 5 x 5 mm^2 pixel size, and 5 kHz spectral bandwidth. The data were reconstructed using a 20 Hz Gaussian spectral apodization for each free induction decay (FID) after zero-filling from 256 to 1024 points. Phase corrections were applied to produce upright absorption mode spectra in the real domain.

Four dogs underwent multislice fast spin echo-planar spectroscopic imaging (MS-FSEPSI) acquisitions (7 scans total) (16). Six axial slices (7 mm slice with 3 mm gap) were acquired sequentially in 6 seconds. The 90° RF excitation pulse was followed by 16 refocusing pulses, and an echo-planar strategy was used to simultaneous acquire a 16 point FID and to encode one dimension of k-space between each refocusing pulse. The in-plane FOV was 9 x 8 cm^2 with 5 x 5 mm^2 pixel size and 493 Hz spectral bandwidth. All data, including those acquired on gradient ramps, were regridded during the reconstruction to rectilinear coordinates using a Gaussian weighted average algorithm (17). FIDs were apodized with a 10 Hz Gaussian filter after being zero filled to 64 time points. Data from the positive and negative echo-planar gradient lobes were processed separately and their magnitude data subsequently combined. Conventional T_2 weighted fast spin-echo (FSE) ^1H images were acquired to identify the anatomy.

The maximum pyruvate and lactate peak heights were determined within the prostate, and the SNRs were calculated using the standard deviation of the signal in a spectral region devoid of peaks for both the 2D-MRSI and the MS-FSEPSI data. Maximum pyruvate SNR was also calculated in the urethra and intravascular space. The SNR was normalized to 20% polarization and for differences in voxel size. Metabolite SNR values and Lac:Pyr ratios were then compared across all dose levels.

7.4 Results

Figure 7.1 shows typical dynamic curves of metabolite peak heights for three $^{13}C_1$-pyruvate dose levels in different dogs. In general, the rate constants decreased as the pyruvate dose increased. Pyruvate SNR showed a positive correlation with dose, but lactate and bicarbonate SNR values remained fairly constant. Table 7.1 shows the mean (±SD) values for metabolite SNR and metabolic rate constants in three dose groups. Only one of the five dogs in the high dose group showed a noticeable bicarbonate peak.

Table 7.2 shows median (±SD) estimated values for spin-lattice decay constants (T_1) and arrival times ($t_{arrival}$). These parameters did not vary greatly between dose groups and were thus combined for all dogs used in this study.

Michaelis-Menten parameters were estimated for pyruvate-to-lactate and pyruvate-to-bicarbonate using the fitted values for $k_{pyr \rightarrow lac}$ and $k_{pyr \rightarrow bic}$. Table 7.3 shows the estimated Michaelis-Menten parameters, including the standard error of the fit.

Figure 7.2 shows a representative example of spectroscopic imaging data for a dog given a dose of 44.6 μmol kg^{-1}. T_2 weighted ^{1}H images are shown with color overlays of lactate and pyruvate peak heights, acquired using MS-FSEPSI. Pyruvate was most noticeable in vascular regions, while lactate was mostly present within the prostate tissue. Similar to the dynamic data, SNR values for lactate remained fairly stable between doses, while pyruvate SNR showed a positive correlation with dose.

Table 7.4 shows maximum lactate SNR values within the prostate and maximum pyruvate SNR values within prostate, urethra, and blood vessels for each image. Lac:Pyr ratios and pyruvate dose levels are also included for each scan. Mean Lac:Pyr values (±SD) separated by dose group were 1.16±0.15, 1.11±0.16, and 0.25±0.10 for increasing

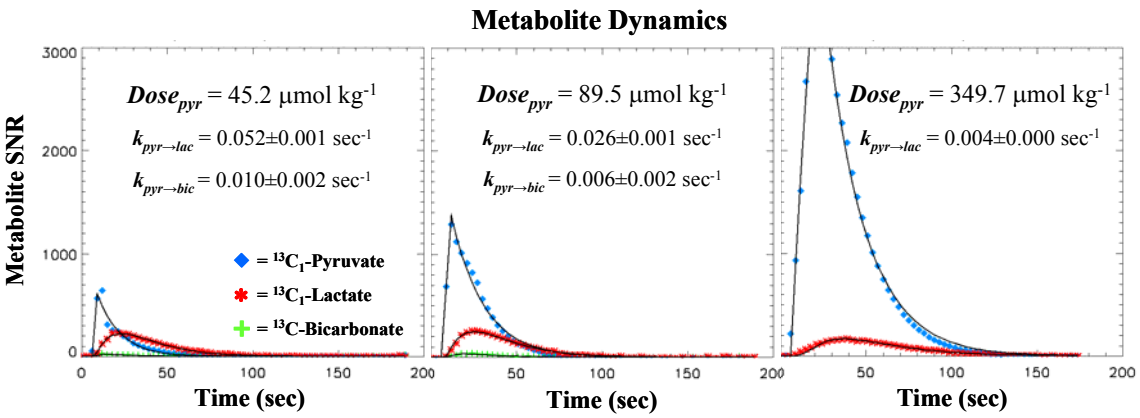

Figure 7.1. Representative dynamic curves of metabolite SNR for 3 different $^{13}C_1$-pyruvate doses in different dogs. The estimated model fit is represented by the black line through the colored metabolite data points. Fitted metabolic rate constants are labeled for each dose. Injection duration was 1.7, 3.1, and 12.7 seconds respectively for the low, medium, and high doses. Bicarbonate was not seen in the dog given the highest dose. SNR is normalized to 20% polarization.

Table 7.1. Mean values of metabolite SNR and metabolic rate constants grouped by dose levels (±SD). Number of dogs (N) in each group is shown below each column.

	45-46 µmol/kg	89-90 µmol/kg	350-362 µmol/kg
Max Pyr SNR	510.3 ± 150	963.3 ± 232	1306.9 ± 1256
Max Lac SNR	199.7 ± 71	265.4 ± 66	149.6 ± 128
Max Bic SNR‡	25.0 ± 13	38.1 ± 15	32.5
$k_{pyr\text{-}lac}$ (sec^{-1})	0.059 ± 0.038	0.037 ± 0.017	0.011 ± 0.007
$k_{pyr\text{-}bic}$‡ (sec^{-1})	0.009 ± 0.001	0.006 ± 0.002	0.005
N	3	3	5 (1‡)

‡ - indicates that only one high dose group dog showed a noticeable bicarbonate peak.

Table 7.2. Median estimated values (±SD) of metabolite T_1 constants and arrival time ($t_{arrival}$) for all dogs included in this study.

	Median ± S.D.
T_{1pyr} (sec)	41.3 ± 155.9
T_{1lac} (sec)	19.4 ± 2.8
T_{1bic}‡ (sec)	11.0 ± 3.8
$t_{arrival}$ (sec)	8.0 ± 1.1
N	11 (7‡)

‡ - Not all dogs showed a noticeable bicarbonate peak.

Table 7.3. Estimated Michaelis-Menten parameters from fitted metabolic rate constants (± standard error from model fit).

	Lactate	Bicarbonate
V_{max} (µmol kg^{-1} sec^{-1})	4.12 ± 2.77	1.82 ± 1.14
K_m (µmol kg^{-1})	24.18 ± 52.34	171.7 ± 146.84

dose levels. The dose-dependency of Lac:Pyr values was similar to $k_{pyr \rightarrow lac}$ in that the ratios decreased, as pyruvate dose increased.

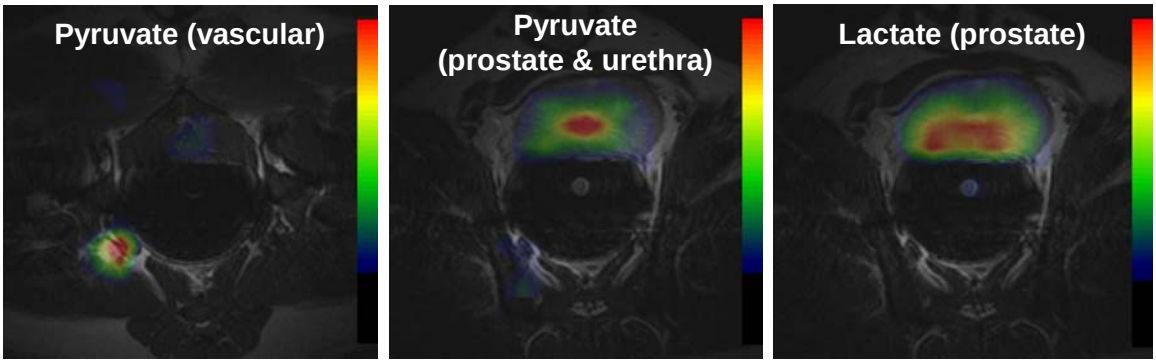

Figure 7.2. Representative pyruvate and lactate peak height images from an MS-FSEPSI data set in a dog given 44.6 μmol kg^{-1} hyperpolarized $^{13}C_1$-pyruvate. Color scale is in a.u. Pyruvate is seen in the prostate, blood vessels, and urethra. Lactate is seen most prominently in prostate tissue only.

Table 7.4. Pyruvate and lactate maximum SNR values in prostate tissue for 14 spectroscopic image acquisitions. Pyruvate SNR values are also shown in vascular regions and within the urethra. Pyruvate dose is listed along with the dog ID number for each scan (row). The far column shows the ratio of lactate to pyruvate in prostate tissue.

Dog ID #	Acquisition Type	Dose (μmol/kg)	Max Pyruvate SNR (vascular)	Max Pyruvate SNR (urethra)	Max Pyruvate SNR (prostate)	Max Lactate SNR (prostate)	Lac:Pyr (prostate)
5063	MS-FSEPSI	45.9	N/A	27.5	19.3	18.7	0.97
5065	MS-FSEPSI	44.6	40.7	38.4	23.8	29.8	1.25
5065	MS-FSEPSI	44.6	25.1	14.0	9.5	12.5	1.31
5064	2D-MRSI	46.2	18.3	21.3	17.7	19.7	1.12
5062	MS-FSEPSI	90.4	30.2	30.0	24.3	28.3	1.16
5065	MS-FSEPSI	89.3	26.5	33.3	26.4	23.0	0.87
5065	MS-FSEPSI	89.3	32.1	28.5	15.9	18.4	1.15
5066	2D-MRSI	89.9	82.4	11.7	15.1	18.8	1.24
5061	MS-FSEPSI	396.8	178.5	50.4	55.2	20.7	0.38
5032	2D-MRSI	362.3	101.9	111.0	93.3	11.9	0.13
5034	2D-MRSI	357.1	92.7	123.0	82.2	22.5	0.27
5038	2D-MRSI	357.1	116.8	225.5	196.2	36.4	0.19
5040	2D-MRSI	349.7	229.4	61.5	70.6	23.9	0.34
5061	2D-MRSI	357.1	94.8	12.6	58.1	11.5	0.20

7.5 Discussion

In both the dynamic and imaging datasets, pyruvate SNR showed a positive correlation with dose levels, while lactate SNR did not. Bicarbonate SNR also did not appear to show a strong dose dependency in the dynamic data. This suggests that, for the range of doses studied here in normal dog prostate, there does not appear to be a significant benefit in using the higher $^{13}C_1$-pyruvate dose. Thus, if the goal is to detect lactate for monitoring the abnormal metabolism typical of prostate cancer, the low $^{13}C_1$-pyruvate dose may be just as effective as the higher doses.

A complication in using the $^{13}C_1$-pyruvate to differentiate tumor from normal tissue is that the tumor has enhanced anaerobic glycolysis. This means that the conversion of pyruvate to lactate would be more pronounced and so it may be difficult to observe the decay of the pyruvate signal at low doses and to estimate ratios of Lac:Pyr. Initial studies in humans should therefore consider both dynamic and spatially localized data at a range of different doses in order to understand the variations in signal intensity observed in tumor versus normal prostate

Estimated rate constants from dynamic ^{13}C spectroscopic data showed that the signal from $^{13}C_1$-pyruvate is converted to $^{13}C_1$-lactate and ^{13}C-bicarbonate faster for lower pyruvate dose levels in normal canine prostates. Metabolite ratios from imaging data also imply a proportionally larger pyruvate-to-lactate rate for lower doses. These results suggest that the LDH and PDH mediated reactions obey Michaelis-Menten kinetics. The low lactate signal seen in blood may indicate that pyruvate is being converted at a lower rate in blood than in prostate tissue. This suggests that it is

reasonable to neglect lactate blood-tissue exchange in the model used to fit the dynamic data, as is done in this study.

The Michaelis-Menten parameters estimated from the fitted rate constants showed relatively large standard errors. This may have been due to variations between each animal, as most dogs only received one dynamic ^{13}C scan and only two dogs received scans spanning two dose levels. Fitting errors would be improved if rate constants were estimated in the same dog at multiple dose levels. Another possible source of error is the size of the slice used to acquire the dynamic data. The tissue in the 6+ cm excited slice can be heterogeneous and vary greatly between animals, and dynamic spectroscopy from this slice should also be expected to vary between animals. Improved spatial location of the representative area, possibly with a one-dimensional dynamic EPSI acquisition (18), would help to reduce this error source. Despite the heterogeneity that was observed, this study demonstrates that knowledge of $^{13}C_1$-pyruvate dose is critical in using metabolic rates and ratios to study disease state and treatment effects.

7.6 Conclusion

This study demonstrates that changes in hyperpolarized $^{13}C_1$-pyruvate signals can be represented by Michaelis-Menten kinetics, and that dose is critical when comparing metabolic rates and ratios to disease state and treatment effects. The real-time detection of $^{13}C_1$-lactate, which is a metabolic marker of hypoxia and cancer, does not appear to improve at higher doses. Achieving a relatively high SNR for $^{13}C_1$-lactate at low $^{13}C_1$-pyruvate doses may significantly benefit future studies by expediting the translation into the clinic.

7.7 References

1. Ardenkjaer-Larsen JH, Fridlund B, Gram A, Hansson G, Hansson L, Lerche MH, Servin R, Thaning M, Golman K. Increase in signal-to-noise ratio of > 10,000 times in liquid-state NMR. Proc Natl Acad Sci U S A. 2003 Sep 2;100(18):10158-63. Epub 2003 Aug 20.
2. Golman K, in 't Zandt R, Thaning M. Real-time metabolic imaging. Proc Natl Acad Sci U S A. 2006 Jul 25;103(30):11270-5. Epub 2006 Jul 12.
3. Golman K, Zandt RI, Lerche M, Pehrson R, Ardenkjaer-Larsen JH. Metabolic imaging by hyperpolarized 13C magnetic resonance imaging for in vivo tumor diagnosis. Cancer Res. 2006 Nov 15;66(22):10855-60.
4. Kohler SJ, Yen Y, Wolber J, Chen AP, Albers MJ, Bok R, Zhang V, Tropp J, Nelson S, Vigneron DB, Kurhanewicz J, Hurd RE. In vivo 13 carbon metabolic imaging at 3T with hyperpolarized 13C-1-pyruvate. Magn Reson Med. 2007 Jul;58(1):65-9.
5. Day SE, Kettunen MI, Gallagher FA, Hu DE, Lerche M, Wolber J, Golman K, Ardenkjaer-Larsen JH, Brindle KM. Detecting tumor response to treatment using hyperpolarized 13C magnetic resonance imaging and spectroscopy. Nat Med. 2007 Nov;13(11):1382-7. Epub 2007 Oct 28. Erratum in: Nat Med. 2007 Dec;13(12):1521.
6. Golman K, Petersson JS, Magnusson P, Johansson E, Akeson P, Chai CM, Hansson G, Månsson S. Cardiac metabolism measured noninvasively by hyperpolarized 13C MRI. Magn Reson Med. 2008 May;59(5):1005-13.
7. Cancer Statistics 2008. American Cancer Society. <http://www.cancer.org/docroot/PRO/content/PRO_1_1_Cancer_Statistics_2008_Presentation.asp>.
8. Gingrich JR, Barrios RJ, Morton RA, Boyce BF, DeMayo FJ, Finegold MJ, Angelopoulou R, Rosen JM, Greenberg NM. Metastatic prostate cancer in a transgenic mouse. Cancer Res. 1996 Sep 15;56(18):4096-102.
9. Chen AP, Albers MJ, Cunningham CH, Kohler SJ, Yen YF, Hurd RE, Tropp J, Bok R, Pauly JM, Nelson SJ, Kurhanewicz J, Vigneron DB. Hyperpolarized C-13 spectroscopic imaging of the TRAMP mouse at 3T-initial experience. Magn Reson Med. 2007 Dec;58(6):1099-106.
10. Larson PE, Kerr AB, Chen AP, Lustig MS, Zierhut ML, Hu S, Cunningham CH, Pauly JM, Kurhanewicz J, Vigneron DB. Multiband excitation pulses for hyperpolarized (13)C dynamic chemical-shift imaging. J Magn Reson. 2008 Jun 24.
11. Zierhut ML, Chen AP, Bok R, Albers MJ, Zhang V, Pels P, Tropp J, Park I, Vigneron DB, Kurhanewicz J, Hurd RE, Nelson SJ, Yen Y-F. Kinetic modeling of hyperpolarized 13C1-pyruvate metabolism using dynamic magnetic resonance spectroscopy. Proceedings of the 15th Annual Meeting of ISMRM, Berlin, 2007, #366.
12. Albers MJ, Bok R, Chen AP, Cunningham CH, Zierhut ML, Zhang VY, Kohler SJ, Tropp J, Hurd RE, Yen Y-F, Nelson SJ, Vigneron DB, Kurhanewicz J. Hyperpolarized 13C Lactate, Pyruvate, and Alanine – Non-Invasive Biomarkers for Prostate Cancer Detection and Grading. Cancer Res. 2008 Sep. [In Press]

13. Tropp J, Calderon P, Carvajal L, Karpodinis K, Chen AP, Vigneron DB, Hurd RE, Ardenkjaer-Larsen J-H. Proceedings of the 14th Annual Meeting of ISMRM, Seattle, WA, 2006. #2594.
14. Nelson SJ, Chen AP, Bok R, Albers MJ, Zierhut ML, Kurhanewicz J, Vigneron DB, Kohler S, Yen Y-F, Tropp J, Gram A, Wolber J, Dirven H, Hurd RE. Hyperpolarized C-13 MRSI data of dog prostate at 3T. Proceedings of the 15th Annual Meeting of ISMRM, Berlin, 2007. #536.
15. Hanes CS. Studies on plant amylases: The effect of starch concentration upon the velocity of hydrolysis by the amylase of germinated barley. Biochem J. 1932;26(5):1406-21.
16. Yen Y-F, Le Roux P, Bok R, Tropp J, Chen AP, Zierhut ML, Park I, Albers MJ, Dirven H, Skloss T, Wolber J, Zhang V, Hu S, Vigneron DB, Kurhanewicz J, Nelson SJ, Hurd RE. Signal Enhancement in Low-Dose Hyperpolarized 13C Imaging Using Multi-Slice FSEPSI Sequence. Proceedings of the 16th Annual Meeting of ISMRM, Toronto, 2008. #890
17. Zierhut ML, Ozturk-Isik E, Chen AP, Pels P, Cunningham CH, Vigneron DB, Nelson SJ. Spectroscopic Imaging of 1H at 3T: Comparing SNR between Traditional Phase Encoding and Echo-Planar Techniques in the Human Brain. Proceedings of the 14th Annual Meeting of ISMRM, Seattle, 2006, #65.
18. Chen AP, Hurd RE, Cunningham CH, Li Y, Zierhut ML, Bok R, Kurhanewicz J, Nelson SJ, Vigneron DB. Spatially Resolved 13C Hyperpolarized Dynamic MRS using Flyback Echo-Planar Readout Trajectory. Proceedings 49th Scientific Meeting ENC, Asilomar, CA, 2008. #60

Chapter 8: Summary

This thesis project was conducted to improve cancer biomarkers using NMR technologies. Three specific areas were investigated: kinetic modeling of ^{1}H DCE-MRI with an inert exogenous contrast agent; three-dimensional ^{1}H MRSI of endogenous metabolites with improved acquisition speed; and real-time monitoring of changes in exogenous hyperpolarized $^{13}C_1$-pyruvate into endogenous products.

Comparing estimated kinetic parameters from T_1 weighted and T_2^* weighted DCE-MRI in glioma patients suggested that the T_1 weighted acquisition, with better image quality and larger spatial coverage, but poorer temporal resolution, may be more helpful in predicting tumor grade than the T_2^* weighted method.

Evaluating the effects of various acquisition time reducing 3D-MRSI techniques in phantoms and volunteers showed that EPSI techniques provide adequate SNR with fewer partial voluming and lipid aliasing artifacts. The flyback EPSI technique was used to acquire data from seventeen patients with glioma using an acquisition time of less than 9.5 minutes.

The application of a kinetic model to the analysis of dynamic ^{13}C spectroscopic data was robust and produced important metabolic parameters in healthy rat kidneys and canine prostates, as well as in transgenic mice with prostate tumors. Michaelis-Menten kinetics successfully described the relationship of the estimated parameters to the amount of injected pyruvate.

This project has contributed to the clinical and scientific communities by helping to evaluate changes in a number of different cancer biomarkers. Kinetic modeling of T_1

weighted DCE-MRI data and ^{1}H 3D-EPSI acquisition techniques have been shown to be particularly valuable. It has also demonstrated the ability to monitor cancer metabolism in an in vivo setting by applying kinetic modeling and EPSI techniques to hyperpolarized ^{13}C data. This suggests that hyperpolarized $^{13}C_1$-pyruvate techniques will be valuable in humans and that significant improvements in non-invasive methods for assessing the prognosis of cancer patients are just on the horizon.

Publishing Agreement

It is the policy of the University to encourage the distribution of all theses and dissertations. Copies of all UCSF theses and dissertations will be routed to the library via the Graduate Division. The library will make all theses and dissertations accessible to the public and will preserve these to the best of their abilities, in perpetuity.

Please sign the following statement:

I hereby grant permission to the Graduate Division of the University of California, San Francisco to release copies of my thesis or dissertation to the Campus Library to provide access and preservation, in whole or in part, in perpetuity.

Matt Zirkle _____ 11/12/08 _____

Author Signature Date